MARMARA UNIVERSITY
INSTITUTE FOR GRADUATE STUDIES
IN PURE AND APPLIED SCIENCES

DEVELOPMENT OF POLYMERIC MATERIALS FOR FLEXIBLE LITHIUM-ION BATTERIES

SANDUGASH KALYBEKKYZY

Ph.D. THESIS

Department of Chemistry

Thesis Supervisor

Prof. Dr. Memet Vezir KAHRAMAN

Thesis Co-Supervisor

Prof. Dr. Zhumabay BAKENOV

ISTANBUL, 2020

MARMARA UNIVERSITY
INSTITUTE FOR GRADUATE STUDIES
IN PURE AND APPLIED SCIENCES

DEVELOPMENT OF POLYMERIC MATERIALS FOR FLEXIBLE LITHIUM-ION BATTERIES

SANDUGASH KALYBEKKYZY

(720815921)

Ph.D. THESIS

Department of Chemistry

Thesis Supervisor

Prof. Dr. Memet Vezir KAHRAMAN

Thesis Co-Supervisor

Prof. Dr. Zhumabay BAKENOV

ISTANBUL, 2020

MARMARA UNIVERSITY
INSTITUTE FOR GRADUATE STUDIES IN PURE AND APPLIED SCIENCES

Sandugash KALYBEKKYZY, a Doctor of Philosophy student of Marmara University, Institute for Graduate Studies in Pure and Applied Sciences, defended her thesis entitled "**Development of polymeric materials for flexible lithium-ion batteries**", on January 21, 2020 and has been found to be satisfactory by the jury members.

Jury Members

Prof. Dr. Memet Vezir KAHRAMAN (Advisor)
Marmara Üniversitesi ....

Prof. Dr. Nilhan KAYAMAN APOHAN (Jury Member)
Marmara Üniversitesi ....

Prof. Dr. Tarık EREN (Jury Member)
Yıldız Teknik Üniversitesi ....

Assoc. Prof. Dr. Emrah ÇAKMAKÇI (Jury Member)
Marmara Üniversitesi ....

Assist. Prof. Dr. Ferhat ŞEN (Jury Member)
Zonguldak Bülent Ecevit Üniversitesi ....

APPROVAL

Marmara University Institute for Graduate Studies in Pure and Applied Sciences Executive Committee approves that Sandugash KALYBEKKYZY be granted the degree of Doctor of Philosophy in Department of Chemistry, Organic Chemistry Program on .05.02....., 2020. (Resolution no: 2020/05-02

Director of the Institute
Prof. Dr. Bülent Ekici

ACKNOWLEDGMENTS

This PhD dissertation was completed at Marmara University, Institute of Pure and Applied Sciences, Department of Chemistry, Organic Chemistry Programme, in collaboration with Nazarbayev University, School of Engineering and Digital Sciences, National Laboratory Astana. This research work was supported by the State Targeted Program #BR05236524 from the Ministry of Education and Science of the Republic of Kazakhstan.

First and foremost, I wish to express the deepest gratitude to my supervisor Prof. Dr. Memet Vezir KAHRAMAN, for his patience, kindness, sharing experience, and endless support. He believed in me and always motivated to keep going on my work. Teşekkürler!

Equally, I would like to express my sincere thanks to my co-advisor, Prof. Zhumabay BAKENOV, for his advice, suggestions, support, and understanding. Thanks for giving me the opportunity to join your group!

A special thanks goes to my advisor Dr. Almagul MENTBAYEVA, who continuously provided encouragement and gave me many ideas, insights, and comments during my research. This dissertation would not have been possible without her persistent help. I appreciate your support!

Also, I want to acknowledge Al-Farabi and Yerkezhan's extra effort and help in conducting experiments. It was very nice to work with you!

Of course, I can't fail without mentioning special thanks to my priceless friends from Marmara University and Nazarbayev University for their friendship and continued support!

My deepest appreciation belongs to my parents Kalybek and Gulnar, parents-in-law Turysbek and Marziya, lovely family members Beibit, Maksat, and Aliya, for their motivation, understanding, and patience.

Finally, I am very thankful to my dearest husband, Ardak, love of my life. Without his support, I would have stopped these studies a long time ago. You always inspired and motivated me doing my work. I am incredibly happy to have you in my life!

December 2019 **Sandugash KALYBEKKYZY**

TABLE OF CONTENTS

ÖZET

ESNEK LİTYUM–İYON PİLLER İÇİN POLİMERİK MALZEMELERİN GELİŞTİRİLMESİ

Esnek elektronik pazarı, klasik elektronik pazarının da ötesine geçmiştir. Yakın gelecekte giyilebilir elektroniklerin ve medikal cihazların kullanımı artacağı için günümüzde esnek katı hal pillerin geliştirilmesi oldukça önemli bir konudur. Yüksek teorik spesifik kapasite, güvenli çalışma gerilimi ve düşük maliyetli üretim gibi avantajları nedeniyle, lityum-sülfür (Li/S) piller, yeni nesil esnek güç kaynağı olarak karşımıza çıkmaktadır. Esnek sülfür bazlı katodun üretilmesi ve esnek katı hal elektrolitler ile birleştirilmesi, Li/S piline önemli avantaj sağlayacaktır.

Bu tez çalışmasında, esnek lityum-iyon pillerde (LİP'ler) kullanılabilecek birtakım alternatif malzemeler geliştirildi. Araştırmanın ilk bölümünde LİP'lerin temel bir bileşeni olarak esnek, bağlayıcı polimer içermeyen sülfür bazlı kompozit katot elektrospin tekniği ile hazırlandı. Nanofiber sülfür katodun, klasik karbonat bazlı elektrolitler ile uyumlu olduğu görüldü. Yüksek kulombik verimliliği, uzun yaşam döngüsü ve yüksek akım yoğunluğu pil uygulamaları için umut vaat etmektedir.

İkinci bölümde, poliakrilonitrilden üç boyutlu karbon nanolif üretilerek, sulfur bazlı katotlar için akım toplayıcı olarak kullanıldı. Ağır metal akım toplayıcısının, daha hafif olan karbon akım toplayıcısı ile değiştirilmesi sülfür katodunun kapasitesini dikkate değer bir şekilde arttırdı.

Üçüncü bölümde, UV polimerizasyon metodı ile siloksan bazlı çapraz bağlı esnek katı polimer eletrolitler geliştirildi. Poli(dimetilsiloksan) bazlı katı polimer eletrolitler, ortam sıcaklığında mükemmel esneklik ve iyonik iletkenliğin artışını gösterdi. Filmlerin termal ve yapısal özelliklerinin yanı sıra elektrokimyasal ve mekanik özellikleri araştırıldı.

Hazırlanan tüm malzemelerin elektrokimyasal performans testleri düğme tipi bataryalar hazırlayarak yapıldı.

ABSTRACT

DEVELOPMENT OF POLYMERIC MATERIALS FOR FLEXIBLE LITHIUM-ION BATTERIES

The market for flexible electronics is rapidly growing out of the boundaries of conventional electronics, and in the nearest future these technologies will be implemented to new areas like wearable electronics and medical devices. Thus, the development of flexible all-solid-state batteries is an important task. Owing to its advantages like high theoretical specific capacity, safe operating voltage, and low-cost production, lithium-sulfur (Li/S) battery is an alternative system for the next generation flexible powering devices. The fabrication of flexible sulfur-based cathode and combination with flexible solid-state electrolytes will significantly advance Li/S battery.

In this dissertation, a number of alternative materials have been developed with the main focus on applicability in flexible lithium-ion batteries (LIBs). The first part of research covers the preparation of an essential component of LIBs, sulfur-based composite cathode. The flexible binder-free sulfur cathode fabricated by electrospinning technique and exhibited good compatibility with the conventional carbonate-based electrolytes. It showed a high coulombic efficiency, long cycle life, and good rate capability, demonstrating a great prospect for battery applications.

In the second part, three dimensional structured nanofibrous carbon was fabricated from polyacrylonitrile and applied as a current collector for sulfur-based cathode. The capacity of the sulfur cathode was remarkably enhanced by replacing heavyweight metal with a lightweight carbon current collector.

Third part covers the development of siloxane-based solid polymer electrolyte by UV-photocrosslinking method. Poly(dimethylsiloxane)-based cross-linked solid polymer electrolyte has excellent flexibility and improved ionic conductivity at ambient temperature. The electrochemical and mechanical properties of films were investigated as well as thermal and structural characteristics.

CLAIM FOR ORIGINALITY

DEVELOPMENT OF POLYMERIC MATERIALS FOR FLEXIBLE LITHIUM-ION BATTERIES

For the last several years, flexible LIBs have become a field of intensive research as a promising power source for forthcoming flexible and wearable electronics. Despite the fact that there are many works on solid-state batteries in literature, the practical application of them is still hindered. This PhD research was focused on the development of flexible components for high-performance all-solid-state LIBs.

In this dissertation work, following novel materials were introduced:

(i) Freestanding sulfur/dehydrogenated polyacrylonitrile/ketjen black (S/DPAN/KB) nanofibrous composite cathode was prepared by electrospinning method. The composite nanofibers were heated at low temperature without carbonization of PAN to insure the flexibility and stability of S/DPAN/KB binder-free cathode. ***(ii)*** 3D structured carbon nanofibers (CNFs) were fabricated by electrospinning technique and applied as a lightweight, 3D structured current collector for sulfur-based cathode. ***(iii)*** Poly(dimethylsiloxane) (PDMS)-based solid polymer electrolyte (SPE) for flexible Li/S batteries were obtained by UV-photocrosslinking of ethylene glycol unit containing oligomers and acrylated PDMS.

All prepared materials are original and do not incorporate any material submitted/published before in literature. The results of this research work were presented in several international conferences and 1 full peer-reviewed paper was published, 1 paper was submitted, and 1 paper is being prepared for submission.

- Flexible S/DPAN/KB Nanofiber Composite as Binder-Free Cathodes for Li-S Batteries. *Journal of The Electrochemical Society*. 166 (3) A5396-A5402 (2019), [DOI: 10.1149/2.0571903jes] (IF=3.120).
- Lightweight 3D Structured Nanofiber Current Collector for High Capacity Sulfur Cathode. *Electrochimica Acta.* (IF=5.383), (submitted).

DECEMBER, 2019

Prof. Dr. Memet Vezir KAHRAMAN **Sandugash KALYBEKKYZY**

SYMBOLS

UV	: Ultraviolet light
$\boldsymbol{l}$	: Thickness of the film
$\boldsymbol{r}$	: Radius
$\boldsymbol{R}_\mathbf{b}$	: Bulk resistance
$\mathbf{T_g}$	: Glass transition temperature
$\mathbf{T_{10}}$	: 10 wt.% weight loss temperature
$\mathbf{T_{50}}$	: 50 wt.% weight loss temperature

ABBREVIATIONS

2D	: Two-dimensional
3B	: Üç boyutlu
3D	: Three dimensional
AB	: Acetylene black
AC	: Acryloyl chloride
BJH	: Barrett–Joyner–Halenda
BET	: Brunauer-Emmett-Teller
CF	: Carbon fiber
CNF	: Carbon nanofiber
CNT	: Multi-walled carbon nanotube
cPAN	: Carbonized polyacrylonitrile
CV	: Cyclic voltammetry
DCM	: Dichloromethane
DMAP	: Dimethylaminopyridine
DMF	: N,N-Dimethylformamide
DSC	: Differential scanning calorimetry
EIS	: Electrochemical impedance spectroscopy
EO	: Ethylene oxide
EC:DMC:DEC	: Ethylene carbonate: dimethyl carbonate and diethyl carbonate
ETPTA	: Trimethylolpropane ethoxylate triacrylate
Et_3N	: Triethylamine
FESEM	: Filed-Emission Scanning electron microscopy

FTIR : Fourier Transform Infrared Spectroscopy

GPEs : Gel polymer electrolytes

HMPP : 2-hydroxy-2-methylpropiophenone

KB : Ketjen Black

LCO : $LiCoO_2$

LEDs : Light-emitting diodes

LFP : $LiFePO_4$

LIBs : Lithium-ion batteries

Li/S : Lithium-sulfur

LiTFSI : Lithium bis(trifluoromethane)sulfonimide

LSV : Linear sweep cyclic voltammetry

LTO : $Li_4Ti_5O_{12}$

LTS : $LiTiS_2$

Ni–Cd : Nickel-cadmium

Ni–Mh : Ni-metal hydrides

NMP : N-methyl-2-pyrrolidone

PAN : Polyacrylonitrile

PDMS : Poly(dimethylsiloxane)

a-PDMS : Acrylated poly(dimethylsiloxane)

PEGDA : Poly(ethylene glycol) diacrylate

PEO : Polyethylene oxide

PMMA : Polymethylmethacrylate

PPE : PDMS-PEGDA-ETPTA film

PVdF : Poly(vinylidene fluoride)

PVdF-HFP	: Poly(vinylidene fluoride-co-hexafluoropropylene)
S/C	: Sulfur-carbon
S/DPAN	: Sulfur-dehydrogenated polyacrylonitrile
S/DPAN/KB	: Sulfur/dehydrogenated polyacrylonitrile/ketjen black
SEI	: Solid electrolyte interface
SEM-EDX	: Scanning electron microscope with energy dispersive X-ray spectroscopy
SPE	: Solid polymer electrolyte
TEM	: Transmission electron microscopy
THF	: Tetrahydrofuran
XPS	: X-ray photoelectron spectroscopy
XRD	: X-ray diffraction

LIST OF FIGURES

LIST OF TABLES

1. INTRODUCTION

In recent years, the development of rechargeable LIBs has received exceptional importance due to the growing need for sustainable energy and rapid expansion of the electronics market [1,2]. Particularly, flexible LIBs have become a field of intensive research as a promising power source for forthcoming flexible and wearable electronics such as roll-up displays, bio-implants, wearable devices, and sensing smart displays. However, packaging materials, eco-compatibility, and safety are always complicating the development of flexible batteries. In conventional LIBs, the majority of safety problems as leakage, flammability, and toxicity are caused due to liquid electrolytes, which consist of dissolved Li salt in organic solvents [3]. There is a necessity for all-solid-state batteries with safe and solvent-free electrolytes. In addition, the development of high performance flexible electrodes and their compatibility with solvent-free electrolytes are relevant tasks.

Owing to its advantages like high theoretical specific capacity, safe operating voltage, and low-cost production, Li/S batteries are up-and-coming systems for the next generation flexible powering devices. However, Li/S battery implementation faces several issues related to the insulating nature of sulfur, dissolution of intermediate products in liquid electrolytes, Li dendrite formation and volume expansion during cycling.

The fabrication of flexible sulfur-based cathode and combination with flexible solid-state electrolyte will significantly advance Li/S battery as solid electrolytes suppress the shuttle effect as well as Li dendrite formation and growth. SPEs are full of promise among solid-state electrolytes due to their excellent flexibility, a wide range of electrochemical stability window, high thermal stability, freestanding thin film forming capability, and lack of organic solvents [4].

Our research was directed to the development and improvement of freestanding sulfur-based composite cathodes and solvent-free polymer electrolytes for flexible all-solid-state LIBs. Consequently, (i) sulfur-polyacrylonitrile nanofibrous composite cathode, (ii) 3D structured carbon nanofiber current collector for sulfur-based cathodes, and (iii) polysiloxane-based SPE were investigated.

The dissertation consists of five chapters: Introduction, Literature Review, Material and Method, Results and Discussion, and Summary and Future Work.

Chapter 1 introduces critical aspects and main issues of flexible LIBs that initiated the motivation to do research. Additionally, an overview of the work is given briefly.

Chapter 2 focuses on the general background of rechargeable LIBs and its components. Further, recent studies and key issues related to flexible all-solid-state LIBs, sulfur-based cathode materials, and solid polymer electrolytes are presented as well as approaches to their solution.

Chapter 3 is Materials and Methods. In the beginning, chapter describes general methods of materials preparation and characterization. All synthesis procedures are presented in Experimental part considering the thesis work in three subsections:

(i) *Freestanding Flexible S/DPAN/KB Cathode by Electrospinning Method.*

In this subsection, S/DPAN/KB flexible nanofiber composite was prepared by electrospinning technique and tested as a freestanding cathode for high-performance flexible Li/S batteries. Optimal conditions of the spinning process were established for the preparation of S/PAN/KB nanofibers with high sulfur content. The obtained composite cathode is highly flexible and can be used for LIB powering flexible electronic devices.

(ii) *PAN Derived Electrospun Carbon Nanofibers as 3D Current Collector for Li/S Batteries.*

CNFs with different diameters and void sizes were fabricated by stabilization and carbonization of PAN nanofibers, which were prepared by simple electrospinning technique. The ultralight and porous CNFs were applied as 3D current collector for sulfur-based cathode and remarkably improved electrochemical performance of the electrode compared to the one on Al foil.

(iii) *PDMS-based Flexible Solid Polymer Electrolytes.*

Here we prepared a series of freestanding transparent polymer films with excellent flexibility and improved ionic conductivity at ambient temperature. Cross-linked SPEs were obtained by UV photocrosslinking of ethylene glycol unit containing oligomers and PDMS with acrylic ends with different mass ratios. Electrochemical and mechanical properties of films were investigated.

All characterization and application results and discussions of each study are presented in **Chapter 4** with the same sequence as above in **Chapter 3**.

Chapter 5 points out the major results and overall conclusion of the thesis work. Future directions related to the results of the research work are also provided.

2. LITERATURE REVIEW

Batteries are one of the crucial devices among energy storage systems due to their usage in many electronics and vehicles. Typical batteries are categorized as primary (non-rechargeable) and secondary (rechargeable) [5]. Primary batteries are disposable ones, which are used daily in household devices, e.g. alkaline batteries. The electrochemical reaction occurred in such cells is irreversible. The secondary batteries are multiuse and can be charged several times. The cyclability of rechargeable batteries depends on the chemistry of the cell, operating profile and many other parameters. Lead-acid, nickel-cadmium (Ni–Cd), sodium-sulfur, and sodium nickel chloride are examples of commonly used secondary battery chemistries in energy storage applications. However, over the last two decades, LIBs rapidly replaced Ni–Cd and Ni-metal hydrides (Ni–Mh) due to their relatively high operating potentials, energy density and long cycle life [6]. LIBs are the most promising energy storage system for portable electronic devices, as well as large-scale equipment amid all rechargeable battery systems.

This chapter considers a brief introduction to lithium-ion rechargeable batteries, its components and operating principles. Further, an overview of recent studies on flexible LIBs, lithium-sulfur batteries, and solid polymer electrolytes are presented.

2.1. Lithium-ion Batteries

Since the successful launch in the 1990s, the batteries based on lithium intercalation electrochemistry have dominated the market for more than two decades due to their relatively high operating potentials and long cycle life [7,8]. LIBs have become popular battery technology especially in portable devices and electric vehicles due to their high energy and power density, high coulombic efficiency and low rate of self-discharge.

As shown in Figure 2.1, conventional LIB cell is composed of negative (A) and positive (B) electrodes that are electrically insulated by a polymer membrane wetted in an organic electrolyte containing lithium salt (C). The electrode materials are deposited onto the current collectors (D, E). Usually, Al foil is used for the positive and Cu foil for the negative electrodes [9]. The negative (anode) and positive (cathode) electrodes are composed of active materials that take part in electrochemical reaction during the charge-discharge process. Active materials are powder of particles in various forms like ellipsoid, spherical, fibrous, and their diameters change from nano to micrometers. The electrode is made by mixing active material with conductive additives (mainly carbon based), binding materials as poly(vinylidene fluoride) (PVdF) and applied on current collector by casting thin layer of slurry. The reverse process occurs during discharge [10]. The chemical energy is converted into electrical energy through the redox reaction, which occurs due to the difference in chemical potentials between the cathodes and anodes [11]. In Table 2.1, general terms of LIBs are given.

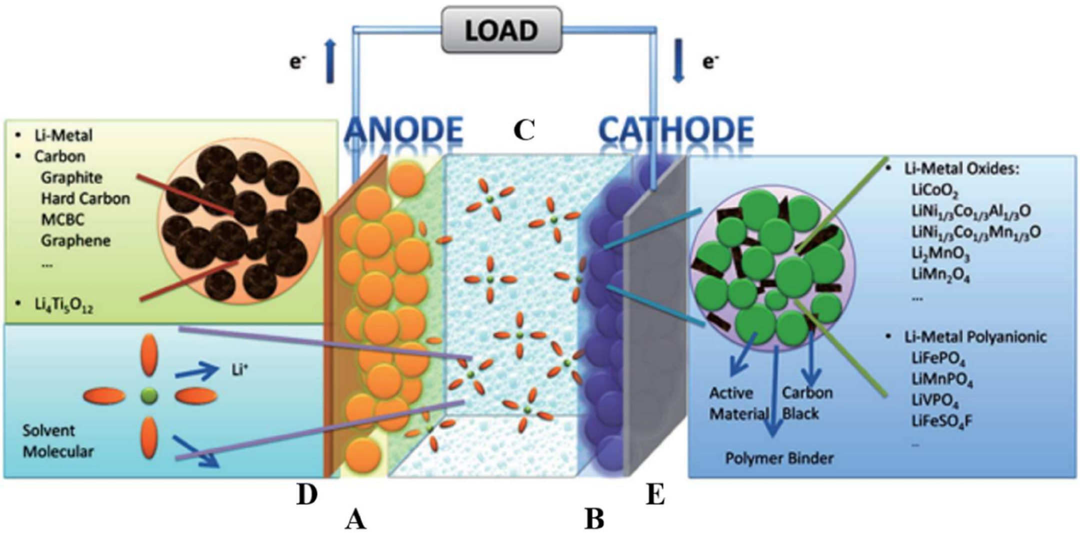

Figure 2.1. The general structure of conventional lithium-ion battery [11].

SONY Corporation commercialized the first LIB, $Li_{1-x}CoO_2$/C cell for portable electronics, which was assembled by Akira Yoshino from Asahi Kasei Corporation and based largely on the work of John Goodenough from the University of Texas [12]. In 1980, Goodenough invented a rechargeable battery with layered structured $LiCoO_2$ (LCO) cathode, where lithium ions can migrate through a liquid electrolyte between electrodes in a cell [13]. This critical discovery was a big step for a modern lithium-ion battery. Since that time, the LIBs have been developing without stop and the capacity in battery increased to > 3.0 Ah for the18650 type cell [15].

Table 2.1. General terms and their explanation used in LIB system [14].

Terms	Explanation
Positive electrode/cathode	An electrode, which has a higher redox potential than the negative electrode.
Negative electrode/anode	An electrode that has a lower redox potential than the positive electrode.
Open-circuit voltage	The voltage between the cathode and anode without load on the battery.
Working voltage	Also called closed-circuit voltage. The voltage between the cathode and anode when there is a load on the battery
Discharging	A process where electrons are released by the negative electrode and low into the positive electrode via the outer circuit. The chemical energy is converted to electrical energy by redox reaction.
Discharge/charge curve	Change of voltage with time during a discharge/charge process.
Discharge capacity	The number of electrons transferred during the discharge for a battery. A discharge capacity of 1 Ah is equivalent to 3600 C.
Discharge rate/C-rate	It is a measure of the rate at which a battery is discharged relative to its maximum capacity. A 1 C rate means that the discharge current will discharge the entire battery in 1 h. A 1/10 C rate represents discharge the entire battery in 10 h.
Cutoff/terminal voltage	The absolute voltage achieved during a charge/discharge process between the electrodes.
Internal resistance	The total resistance between two electrodes, including the resistance from any other components of battery.
Cycle life/cyclability	The number of cycles (charged and discharged), until the battery loses energy significantly or can no longer sustain function of the device it powers.
Internal short circuit	The direct contact of negative electrode with the positive electrode without any barrier.
Charging	The move of electrons from the cathode side to the anode side through the outer circuit.
Constant-voltage charge	A constant voltage charger is maintained at the same input voltage of the battery during the charging process, regardless of the state of charge of the battery. When the voltage reaches the specified voltage, this process ends.
Constant current charge	A constant current charger is maintained at the same current input to a battery during a charging process, regardless of the battery's state of charge. When the current arrives at the specified amperage, this process terminates.
Capacity density	Discharge capacity per mass, area, volume, or of a battery. The unit is usually milliampere-hour per centimeter square or milliampere-hour per gram (mA h/cm^2, mA h/g).

Table 2.1. (Continued)	
Energy density	The nominal battery energy per unit volume or mass. Specific energy density is a characteristic of the battery chemistry and packaging.
Coulombic efficiency	This is a ratio (%) of the total charge extracted from the battery to the total charge put into the battery over a full cycle.
Power efficiency	This is the ratio (expressed as a percentage) of the energy expended by all the circuit components compared with the battery energy consumption.
Power density	The discharge energy per volume or mass of a battery. The unit is usually watt per liter or watt per gram. Specific power density is a characteristic of the battery chemistry and packaging.
Specific capacity	The amount of charge that can be reversibly stored per unit weight (mA h/g)

The most used lithium-ion chemistries and their characteristics are given in Table 2.2. The operating voltage of typical Li-ion cells is about 3.2–3.8 V nominal, which is quite high in comparison with Ni–Mh and Ni–Cd cells operating at 1.2–1.5 V. This is an important feature as it affects the number of connecting cells to reach required pack voltage. In addition to this, LIBs have a lower rate of self-discharge, which indicates that natural loss of capacity over time is less than in other systems. The capacity loss is classified into two: reversible and permanent capacity loss during the energy storage. Reversible capacity loss is the energy lost from the system and can be restored after cycling again, while permanent capacity loss cannot be restored. In general, all energy storage systems have capacity loss over time.

Table 2.2. The most common lithium-ion chemistries [5].

	Lithium Iron Phosphate	Lithium Manganese Oxide	Lithium Titanate	Lithium Cobalt Oxide	Lithium Nickel Cobalt Aluminum	Lithium Nickel Manganese Cobalt
Cathode	LFP	LMO	LTO	LCO	NCA	NMC
Specific energy (Wh/kg)	80-130	105-120	70	120-150	80-220	140-180
Energy density (Wh/L)	220-250	250-265	130	250-450	210-600	325
Specific power (W/kg)	1400-2400	1000	750	600	1500-1900	500-3000
Power density (W/L)	4500	2000	1400	1200-3000	4000-5000	6500
Volts (per cell) (V)	3.2-3.3	3.8	2.2-2.3	3.6-3.8	3.6	3.6-3.7
Cycle life	1000-2000	>500	>4000	>700	>1000	1000-4000
Self-discharge (% per month)	<1%	5%	2-10%	1-5%	2-10%	1%
Cost (per kWh)	\$400-\$1200	\$400-\$900	\$600-\$2000	\$250-\$450	\$600-\$1000	\$500-\$900
Operating temperature range (°C)	-20 to +60	-20 to +60	-40 to +55	-20 to +60	-20 to +60	-20 to +55

2.2. Components of Li-ion Battery

2.2.1. Anode materials

High capacity active materials for anode are essential for the improvement of LIB's electrochemical performance. The use of lithium metal as an anode material for rechargeable batteries is very expensive and unsafe since a short circuit may occur between the electrodes due to the formation of dendrites on Li metal [16]. Most of the commercial LIBs are used graphite as an anode. Graphite has a good cycle life, low working potential, and low cost.

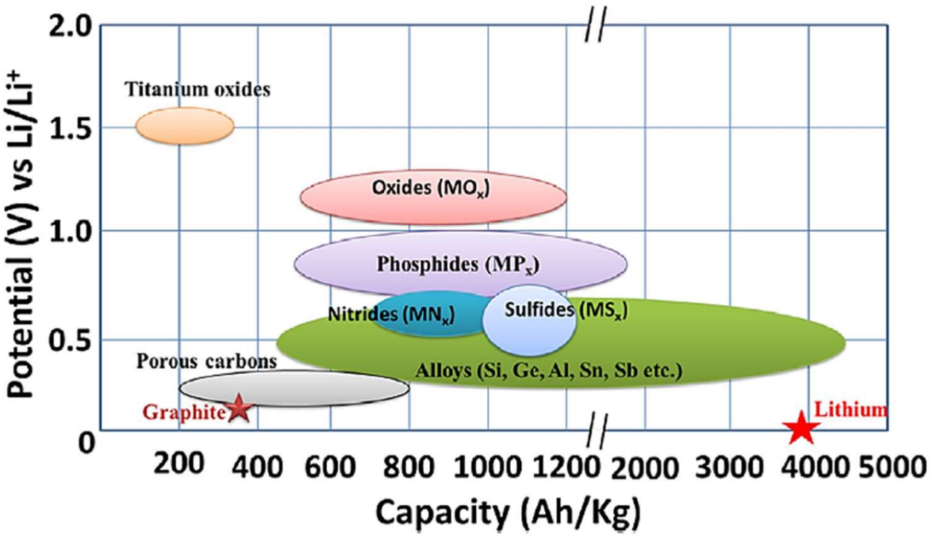

Figure 2.2. Ragone plot of various active anode materials for LIBs. Potential vs. Li/Li^{+} and the corresponding capacity density are shown [16].

However, graphite is not compatible with propylene carbonate-based electrolytes because of the intercalation of propylene carbonate between the graphitic planes that leads to capacity fading. Figure 2.2 shows ragone plot of various anode materials' average discharge potentials and specific capacities. $Li_4Ti_5O_{12}$ (LTO) anode has already been commercialized owing to its safety, high stability (structural), and long cycle life. It is known as "zero strain" intercalation anode out of the change in volume of only 0.2 % during lithiation/delithiation process [17]. Titanium oxides are promising active materials for hybrid electric vehicles among the anodes. Silicon-based materials are also studied widely amid alloying materials and considered as an attractive anode for the next generation LIBs.

At the present, the total capacity of LIB systems is limited mainly by the low capacity of cathode materials.

2.2.2. Cathode materials

In order to meet the growing demand in high capacity LIBs, there is a need for cathode materials with higher capacities than commercially used $LiCoO_2$ (272 mAh g^{-1}), and $LiFePO_4$ (170 mAh g^{-1}). Cathode active materials can be divided into two groups:

1) Intercalation cathode materials

2) Conversion cathode materials

Intercalation cathode materials. Li^+ ions can be inserted in, stored and removed from the intercalation cathode materials. Transition metal oxides, metal chalcogenides, and polyanion compounds are main types of intercalation cathodes [13]. These host network compounds have various crystal structures like layered, spinel, olivine, and tavorite as shown in Figure 2.3.

The $LiTiS_2$ (LTS) is an example of intercalation cathode of layered structure, which was extensively investigated due to its high gravimetric energy density and long cycle life. The LTS was commercialized by Exxon [18]. Nevertheless, transition metal oxide and polyanion cathode materials are more popular for investigation and application owing to their high operating voltage, which results in higher energy storage capability. As it is seen from Figure 2.3 e, specific capacity of typical intercalation cathodes is around 150-200 mAh/g with an average operating voltage 3–5 V vs. Li/Li^+.

$LiCoO_2$ (LCO) is the most common used intercalation cathode material for LIBs with layered crystal structure (Figure 2.3 a). Such transition metal oxides and phosphates undergo oxidation to higher valences when Li^+ is extracted [19]. The operation principle scheme of LIB with LCO cathode is illustrated in Figure 2.4.

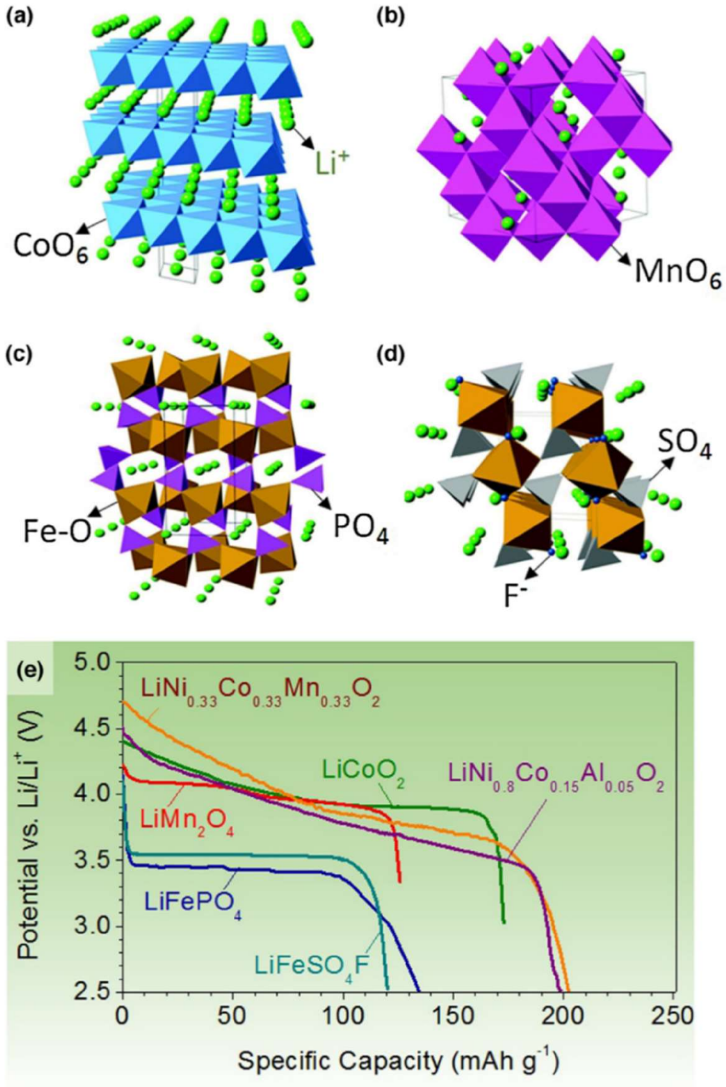

Figure 2.3. Schematic illustration of (a) layered ($LiCoO_2$), (b) spinel ($LiMn_2O_4$), (c) olivine ($LiFePO_4$), (d) tavorite ($LiFeSO_4F$) crystal structured cathode materials and their (e) discharge profiles [20].

The chemical reactions of the typical cell with $LiCoO_2$ (cathode) and graphite (anode) electrodes are as follows:

Anode: $$6C + xLi^+ + xe^- \leftrightharpoons Li_xC_6$$

Cathode: $$LiCoO_2 \leftrightharpoons Li_{1-x}CoO_2 + xLi^+ + xe^-$$

Total reaction scheme: $6C + LiCoO_2 \leftrightharpoons Li_xC_6 + Li_{1-x}CoO_2$

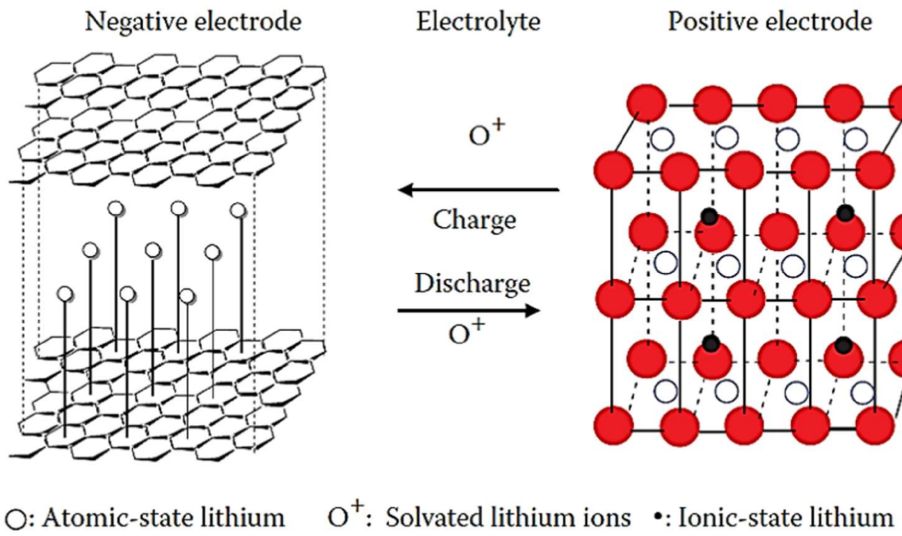

Figure 2.4. The operation principle scheme of LIB with LCO cathode and graphite anode [14].

In the cathode side, Li^+ ions deintercalate from the electrode material, and Co^{3+} oxidizes into Co^{4+} by releasing electrons during the charging process. The inverse reaction occurs during the discharge. In the anode side, Li^+ ions intercalate into the graphite layers, transform into atomic Li by obtaining electron from the lattice. The deintercalation of Li from the graphene layers occurs by losing one electron during the discharge process; as a result, ionic state Li forms [14]. In this way, lithium ion moves between the electrodes during the cycling of LIB. Despite the fact that LCO is the appropriate cathode material for LIBs with high theoretical capacity and good cycling performance, there are some limitations such as low thermal stability, high cost, and capacity fade.

The $Li_2Mn_2O_4$ is a cathode material with a spinel structure (Figure 2.3 b). The main advantages of Mn are low cost, abundance, and non-toxicity [21]. However, it suffers from the low stability in organic electrolytes, which results in poor cyclability [22]. Similarly, lithium nickel oxide, vanadium oxide, and iron oxides are also metal oxide cathode materials.

Each of them has its own limitations, and research efforts on the improvement of active materials are still actively ongoing.

Another type of intercalating cathode is polyanion materials ($LiFePO_4$, $LiFeSO_4F$, Li_2FeSiO_4) [23]. Among them $LiFePO_4$ (LFP) is the most studied and commercially available cathode. It has olivine structure as shown in Figure 2.3 c. LFP is chemically stable during cycling and has good electrochemical performance. However, electrical and ionic conductivities are poor [20].

$Fe(SO_4)F$, $V(PO_4)F$ are examples of tavorite-structured intercalating compounds, which are basically from fluorosulfate and fluorophosphate families. The structure studies and synthesis of $LiFe(SO_4)F$, $LiV(PO_4)F$ based new compounds as cathode materials are still being investigated. Also, electrochemical performance of these compounds should be improved [24].

Conversion cathode materials. Conversion cathodes are promising electrode types that can undergo redox reaction during charge/discharge as expressed below:

Type 1 $MX_z + yLi \rightleftharpoons M + zLi_{(y/z)}X$

Type 2 $yLi + X \rightleftharpoons Li_yX$

Transition metal oxides, phosphides, sulfides, nitrides, and fluorides are examples for the reaction type 1. Since they have metal ions with high valence, higher theoretical capacities are obtained by undergoing conversion reactions. For some active materials, the reaction mechanism can be little different because of the formation of intermediate phases.

The reaction mechanism of conversion cathode materials like S, Se, Br, I, and Te approaches to type 2 [25]. The electronic conductivity of Se and Te is high, thus the rate capability of this cathodes are higher than sulfur-based cathodes. However, sulfur-based cathode materials are the most attractive conversion cathode materials due to the high theoretical specific capacity (1675 mAh g^{-1}) and low cost [26]. Even so, these type of compounds have issues like dissolution of intermediate compounds (Se, S) in organic solvents, poor conductivity (S), and volume expansion (Se, Te). Additionally, Te and Se elements are costly.

In conclusion, sulfur-based materials are the most promising active materials among conversion cathodes and are discussed separately below in all-solid-state LIBs part.

2.2.3. Current collectors

The current collector is an essential component to hold the electrode material, ensure good current conduction and collect the accumulated electrical energy from the electrode [27]. It plays a significant role on battery performance. Two-dimensional (2D) Al foils are the most commonly used current collectors for cathodes in LIBs allowing low cost and mature manufacture. However, the instability of Al metal in organic electrolyte is still a challenge, hindering long-cycle sustainability of electrical conductivity [28]. Its heavy weight, limited surface area and weak adhesion of electrode material are also issues which affect the electrochemical performance of the battery [29,30]. The 3D structured current collectors with porous structure allows to incorporate electrode materials into its voids and hold more active material per specific area. Therefore, the development of 3D structured current collectors with lightweight, chemical stability and ability to keep good adhesion of active materials are necessary for the next-generation LIBs. Especially, current collectors with high conductivity and porous structure are highly desired for active materials with low conductivity as S, Si, LFP etc.

Until now, the various types of current collectors including nickel, stainless steel, and carbon in the form of thin foil, foam, and mesh, were developed in order to improve the electrochemical properties of electrodes [31–35]. Among them, carbon materials are promising alternatives to conventional metal-based current collectors due to their good chemical stability and low mass density, which reduces total weight of the energy storage system, and increase the specific overall energy density. Particularly, carbon fibers (CFs) have many advantages like high conductivity, structural stability, and large surface area, which makes them attractive to use in energy storage devices [36,37]. Use of CFs with interconnected 3D void spaces as 3D structured current collector allows to incorporate electrode materials into its 3D structure and hold more active material per specific area. Beside this, CFs have low cost compared to metallic 3D current collectors. Previously, H. Lu et al. successfully fabricated flexible, mechanical and chemical stable $Li_4Ti_5O_{12}$ electrodes by using commercial CFs as a current collector [38]. Also, Y. Zhang compared Ni foam and carbon fiber cloth as 3D current collectors for Li/S batteries where the cell with CF current collector exhibited enhanced electrochemical performance, showed better rate capability and delivered a highly reversible discharge capacity compared to Ni foam [39]. In conclusion, CFs are up-and-coming materials in fabrication of lightweight, 3D structured high performance active electrodes. Especially, they can be favorable for sulfur-based electrodes, which suffer from low conductivity, volume expansion, and low active material loading.

2.2.4. Separators

Separators are thin porous membranes that physically isolate the negative and positive electrode from each other. The direct contact of positive and negative electrodes leads to an internal short circuit, resulting in a cell failure. Separators usually made of porous polymer or ceramic materials and should be chemically stable in organic electrolytes [5]. In addition to this, the durability and mechanical stability of the membranes are significantly important.

In Figure 2.5, commonly used polymer formulas for separators are given.

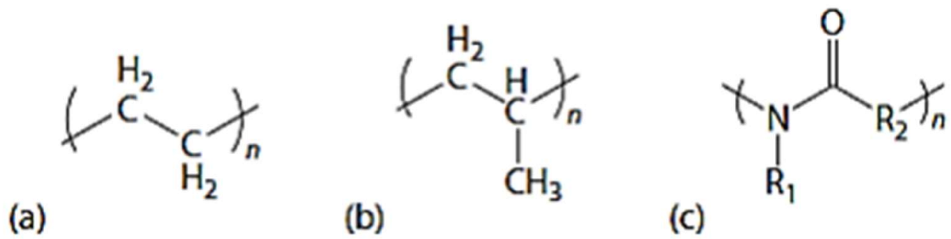

Figure 2.5. Main polymers used for commercial separators: (a) Polyethylene, (b) polypropylene, and (c) polyimide polymers.

Membranes are mainly prepared from the ceramic materials, blend of the polymers, and modified polymers (polyolefins, polyethylene, polypropylene). Coating the separator with ceramics, polymers as poly(vinylidene fluoride) (PVdF), and cross-linking with other polymers are methods of improving/enhancing properties of separators. The safety of LIBs greatly depends on separators [14]. Due to the safety issues, in recent years, the replacement of conventional separators with solid/gel ion conductive membranes is actively being studied and is discussed below in the Electrolytes part.

2.2.5. Electrolytes

A conventional electrolyte is a solution of lithium salt in organic solvents that works as a conductor of lithium ions and enables them to move between electrodes [40]. Several organic solvent types for the electrolytes are shown in Figure 2.6.

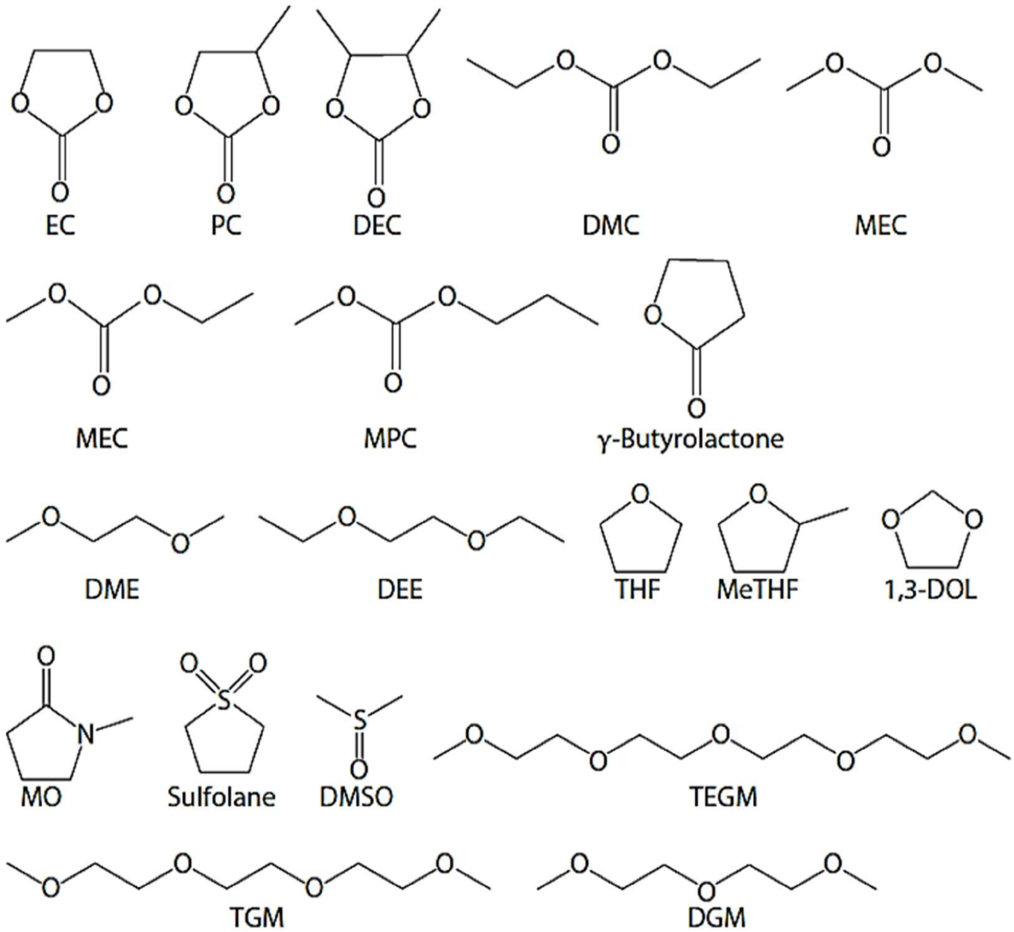

Figure 2.6. Molecular structures of some organic solvents for lithium-ion battery electrolytes.

Among them, carbonate-based solvents with lithium salts (mainly $LiPF_6$, $LiClO_4$, $LiBF_4$) are widely used in LIBs. In addition, each battery manufacturer uses various additives, which is a key secret of the manufacturer. Additives facilitate the formation of solid electrolyte interface (SEI) layer, reduce the irreversible capacity, and some of them increase the thermal stability of the cell. The main advantages of the liquid electrolyte are high conductivity (10^{-3} $\sim 10^{-2}$ S cm^{-1}) and stable contact with electrodes [14]. However, safety issues of LIBs as toxicity of organic solvents, flammability, and leakage are mostly related to liquid electrolytes. Moreover, separators and liquid electrolytes are electrochemically unstable and it limits the application of high voltage cathode materials. By this reason, polymer and ceramic electrolytes are being investigated intensively to replace liquid electrolytes.

Polymer electrolytes can be classified as gel polymer electrolytes (GPEs) and solid polymer electrolytes (SPEs). GPEs are a combination of polymer matrix with liquid electrolyte. They have higher ionic conductivity, better interfacial and mechanical properties compared to SPEs [3]. Additionally, electrolyte leakage is significantly reduced in the use of GPE. Polymers like polyethylene oxide (PEO), polymethylmethacrylate (PMMA), PVdF, poly(vinylidene fluoride-co-hexafluoropropylene) PVdF-HFP, PAN are traditional polymer skeleton for GPEs [41]. However, the mechanical performance of GPEs with the polymers mentioned above is poor, and various methods are being developed to improve the properties. Blending with different polymers, crosslinking, adding nanofillers are some approaches to enhance and functionalize polymer matrix. In Figure 2.7, a brief information about types and advantages of GPEs are given. Furthermore, biodegradable, green polymer-based skeletons are also are being investigated for GPEs [3].

SPEs consists of polymers with ion conductive chains and Li salt. Ionic conductivity at ambient temperature is a challenge for SPEs. Nevertheless, for the development of solid-state batteries, SPEs are the most promising electrolytes and are discussed below in the all-solid-state LIBs part.

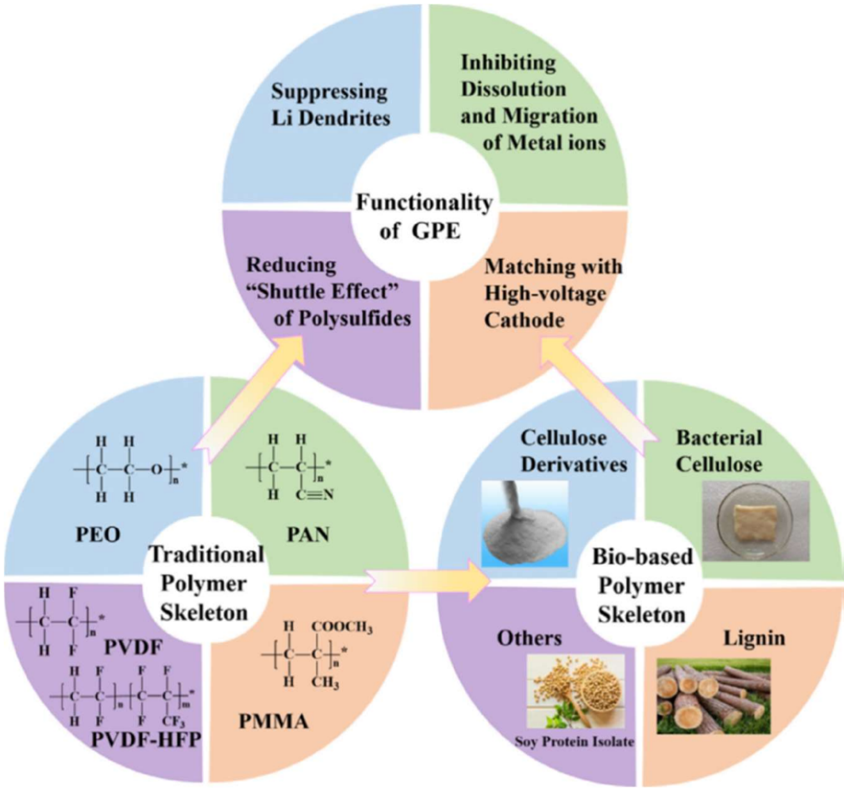

Figure 2.7. Polymer skeleton examples for GPEs and their functionality [42].

2.3. Flexible All-solid-state Li-ion Batteries

"Flexible electronic device" is a general term for devices that can operate when bent, folded, compressed, or stretched. Growing demand for such technologies stresses the importance of the characteristics like portability, convenience and design for consumer [43]. Nowadays, the market for flexible electronics is rapidly growing out of the boundaries of conventional electronics, and in the nearest future these technologies will be implemented to new areas like wearable electronics and medical devices [43,44].

For the last several years, academic and R&D researchers have been working on the development of solid-state flexible LIBs. However, the selection of suitable components and their integration with each other is still an unsolved problem. The packaging materials, rigid electrodes, eco-compatibility, and safety are always complicating the development of flexible batteries.

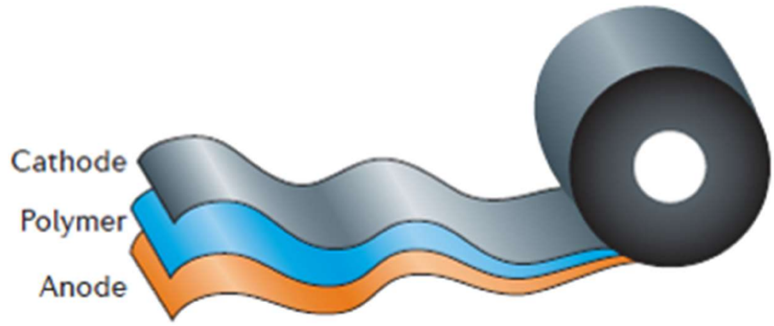

Figure 2.8. Schematic illustration of all-solid-state LIB with flexible components [45].

In order to be a power supply for electronics, flexible LIBs must have a high capacity, and the battery performance should not worsen due to mechanical deformation. Figure 2.8 shows possible schematic illustration of flexible solid-state LIB. Currently, the development of flexible cathode/anode and appropriate solid electrolytes compatible with electrodes is a relevant task for all-solid-state batteries. The sulfur-based cathodes and solid polymer electrolytes are hopeful candidates for all-solid-state batteries and discussed below in two parts.

2.3.1. Sulfur-based cathode for flexible LIBs

Sulfur cathode has a theoretical specific energy of 2567 Wh kg^{-1}, which is remarkably higher than commercial $LiCoO_2$/C lithium-ion batteries [26,46]. Furthermore, sulfur-based cathodes have large capacity, safe operating voltage, and excellent potential for low cost production [47]. Due to these advantages, Li/S batteries are one of the most promising systems for the next generation flexible powering devices.

During discharge/charge process, between sulfur and Li redox reaction occurs as follows:

$$2Li^{+} + S_8 + 2e^{-} \leftrightarrow 2Li_2S_8$$

$$2Li^{+} + Li_2S_8 + 2e^{-} \leftrightarrow 2Li_2S_6$$

$$2Li^{+} + Li_2S_6 + 2e^{-} \leftrightarrow 2Li_2S_4$$

$$2Li^{+} + Li_2S_4 + 2e^{-} \leftrightarrow 2Li_2S_2$$

$2Li^{+} + Li_2S_2 + 2e^{-} \leftrightarrow 2Li_2S$

The overall reaction of Li/S system:

$S_8 + 16Li + 16e^{-} \leftrightarrow 8Li_2S$

Each step of complete reaction influences the operation of Li/S battery. Typical Li/S cell configuration with Li anode is given in Figure 2.9.

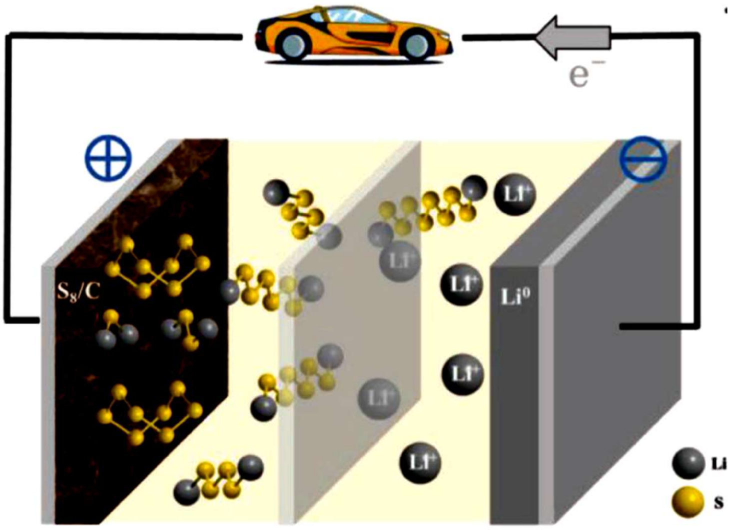

Figure 2.9. Schematic configuration of a typical Li/S cell.

There are several issues, which are still preventing the commercialization of Li/S batteries. The first major problem is insulating nature of sulfur, which results in poor electrochemical accessibility and low utilization of sulfur in the electrode. Due to this point, usually sulfur--carbon (S/C) composite material is used as an electrode. During the preparation of the conventional S/C composite electrode, a large amount of conductive additives (carbon black) and polymer binders (PVdF) are used to provide mechanical stability and electrical connectivity to the whole system. Additives and binders reduce the sulfur content in the electrode, which significantly reduces the overall energy density of the battery [48]. The second issue is a high solubility of lithium polysulfides (intermediated compounds) in organic liquid electrolytes, which leads to side reactions in anode side (shuttle effect). Third is a large volume variation of sulfur during cycling. All these problems result in a rapid capacity fading, low coulombic efficiency, decrease in power capability and poor cycling stability [49,50]. Also, another factor which complicates the commercialization of Li/S batteries is the safety issue related to Li metal anode. The Li dendrite growth and instability of organic liquid electrolytes are always issues for anode.

Various strategies have been developed to solve the above-mentioned problems, such as encapsulation of sulfur in nanostructured carbon materials and combining it with conductive polymers like PAN, [50,51] polyaniline, [52,53] polythiophene, making S/C composite materials adding conductive matrices (Figure 2.10) [54]. Also, loading elemental S into different porous materials like mesohollow, microporous carbon fibers is another established option [55,56]. The use of solid-state polymer electrolytes is an alternative approach, which can help to prevent shuttle effect and Li dendrite growth. Additionally, SPEs may accommodate the volume changes in S electrode due to polymer elasticity.

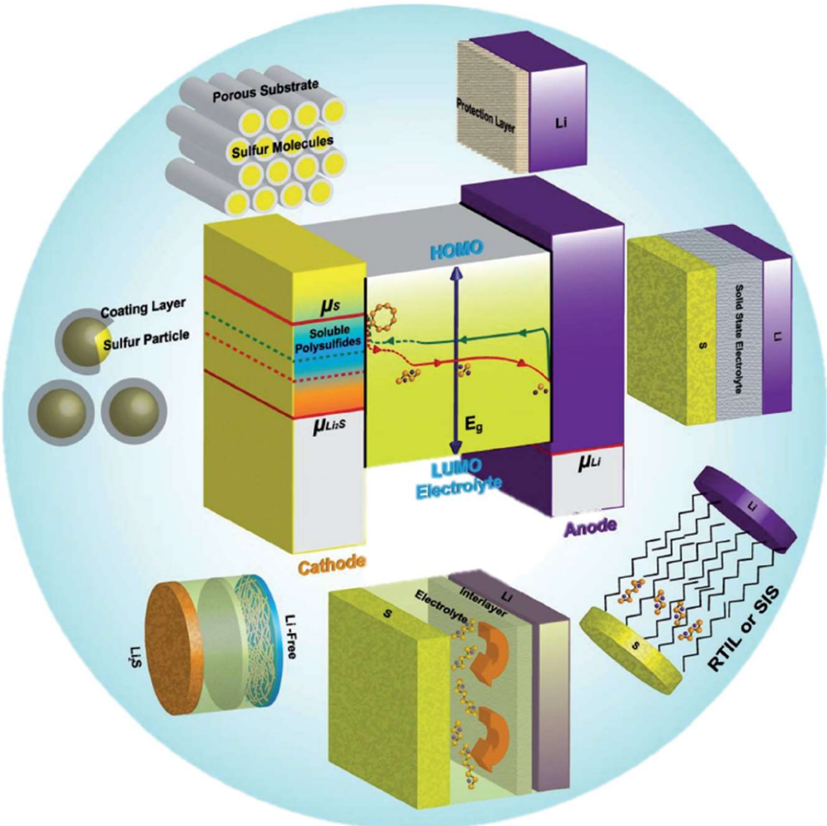

Figure 2.10. Basic approaches to overcome Li/S battery issues [57].

Binder-free, freestanding, sulfur electrodes are also considered to be promising electrodes with high volumetric energy and power density.

The sulfur-dehydrogenated polyacrylonitrile (S/DPAN) could be a valuable system as a freestanding composite electrode. First, Wang et al. reported S/DPAN composite by heating the mixture of sulfur and PAN at 280–300 ºC. Fixing of sulfur by conductive polymer skeleton improved cyclability and capacity of Li-S battery. Embedded sulfur between cyclic rings of conductive DPAN in some degree suppresses polysulfide migration (Figure 2.11) [58].

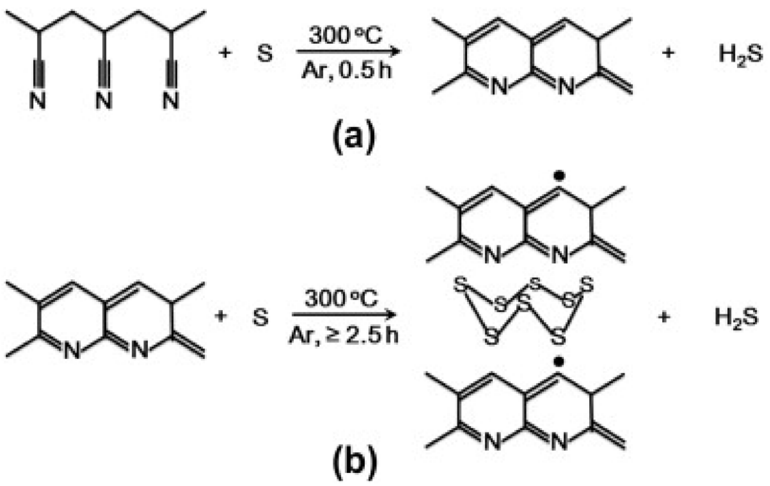

Figure 2.11. Proposed reaction scheme of PAN and sulfur after heat treatment at 300 ºC after (a) 0.5 h and (b) 2.5 h by Wang et al. [59].

The development of nanostructured S/DPAN composites can give an opportunity of making flexible electrodes with different functionalities [49]. Nanofibrous materials are garnering increased attention in the fabrication of materials for LIBs [60]. They have large surface area, high length/diameter ratio, good flexibility, high porosity and multiple functionalities [61]. One of the simplest methods to prepare nanofibers is the electrospinning technique which can be applied to different types of polymers, polymer alloys, and polymers/inorganic composite materials [62–64]. The selection of components for electrospinning method is quite extensive, which is advantageous for the fiber fabrication with different morphology, structure, and functionality. From this perspective, the preparation of S/DPAN cathode materials by electrospinning is an effective option for the development of a flexible electrode. Moreover, nanofibrous cathodes could be compatible with solid polymer electrolytes due to their porous and fibrous structure. The fabrication of flexible S/DPAN electrode and combination with flexible solid polymer electrolyte will significantly advance Li/S battery as solid electrolytes suppress the shuttle effect [65].

Along these lines, another important challenge about solid-state LIBs is the preparation of flexible solid-state electrolytes and their compatibility with electrodes.

2.3.2. Solid state electrolytes

In conventional LIBs, the majority of safety problems as leakage, flammability, and toxicity are caused due to the liquid electrolytes, which consist of dissolved Li salt in organic solvents [3]. Therefore, there is a necessity for all-solid-state batteries with safe and solvent-free electrolytes [66]. There are two types of solid-state electrolytes: polymer and ceramics based electrolytes. Among them, much attention has been devoted to SPEs as a promising candidate for flexible LIBs owing to its benefits like excellent flexibility, a wide range of electrochemical stability window, high thermal stability, thin film forming capability and lack of organic solvents [67]. Generally, SPEs are prepared by dissolution of Li salts in a polar polymer matrix, where Li^+ ions coordinate with the electron-donor groups in the polymer host. Ion conduction occurs by the electric field which forces ions to hop from one coordinating site to another [68,69]. Figure 2.12 shows Li^+ ion migration through the polymer chain and cluster. Usually solvation of ions occurs by coordinating ethylene oxide (EO) units of polymers. Segmental motion of polymer chains is also important for migration of ions [70].

Polymers may contain both crystalline and amorphous regions in their structure. Mainly, transport of ions occurs in the amorphous region of the polymer material [71]. Wright et al. reported the first study of ionic conductivity in crystalline PEO with alkali iodide salts [72]. Following in 1978, Armand applied PEO/alkaline salt complexes as electrolytes for lithium batteries [73]. Since that, a great deal of research has been done on the development of PEO based SPEs by using polymer blends from polycarbonate, polysiloxane, plastic crystal, and hybrid composites for all-solid-state Li-ion batteries [74,75].

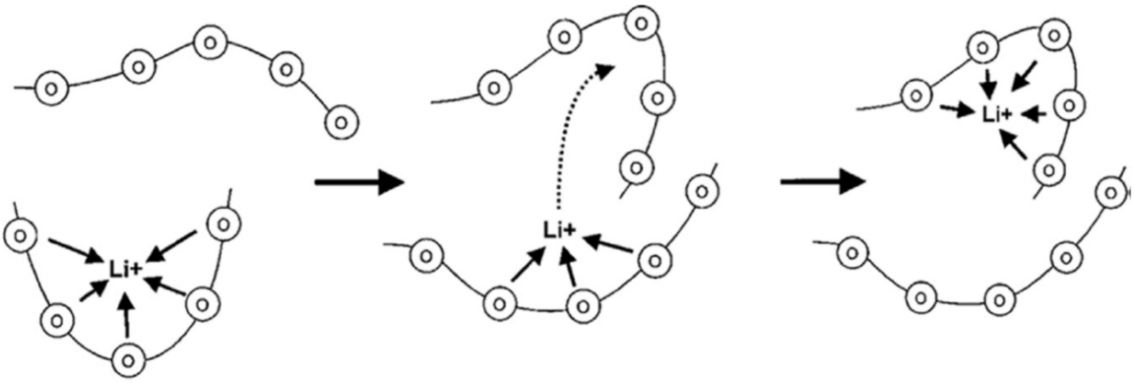

Figure 2.12. Scheme of Li^+ ion migration in PEO based polymer matrix [70].

However, the application of SPEs is limited due to the low ionic conductivity at ambient temperature, which is related to the crystalline nature of PEO [76]. The introduction of an amorphous region into the structure of the electrolyte can enhance the ionic conductivity since the movement of polymer chains, degree of crystallinity, and flexibility greatly affect the ion transport [77]. Polymers with low glass transition temperatures (T_g) are more suitable in order to remain rubbery at room temperature, at the same time to have desired mechanical properties at high temperatures [78]. It is widely known that comb-shaped/cross-linked SPEs prepared with various polymers such as polyacrylates, polyphosphazenes, and polysiloxanes have high flexibility and enhanced amorphous phase [79]. Among them, polysiloxanes have unique/exceptional characteristics of low T_g, related to the flexibility of the Si-O-Si bond which is helpful for Li-ion conduction [80]. Additionally, polysiloxanes have high flexibility, low toxicity and high chemical stability.

There are several successful works on polysiloxane based SPEs with improved ionic conductivity and flexibility [81–83]. PDMS is one of such promising polymers which is popular in industrial/energy storage applications [4,84]. Since it is in liquid form at room temperature, dimensional stability of PDMS has to be improved. Cross-linking or adding appropriate polymer to its structure can improve dimensional and thermal stability of PDMS

[85,86]. Besides, cross-linking hinders crystallization of polymer blend and enhances mechanical strength.

Recently, PDMS-based cross-linked network SPE with polyethylene epoxide was developed by "thiol-epoxy" click chemistry [85]. The ionic conductivity of samples was 1.5×10^{-6} S cm^{-1} at room temperature and Li ion transference number was 0.20. However, these SPEs do not have enough flexibility to apply for the flexible LIBs.

UV photocrosslinking is an alternative way to improve mechanical stability of PDMS-based electrolytes. This process is very simple and fast. Acrylic ended polymers with EO chains like polyethylene glycol diacrylate/triacrylate, ethoxylated triacrylates are great alternatives, which may improve both electrochemical and mechanical properties of SPEs. In addition, the UV cross-linkable polymer blend is suitable for *in-situ* polymerization of SPE within the porous electrode, which is beneficial to develop all-solid-state LIBs. The *in-situ* polymerizable SPEs are promising to develop electrode-electrolyte combined systems for solid-state LIBs.

3. MATERIAL AND METHOD

3.1. Chemical Materials

All chemicals were used as received without further purification. Solvents which were used for SPE preparation were dried before use by molecular sieves (4A). The list of used chemicals is given in Table 3.1.

Table 3.1. The list of chemical materials used in Experimental Part.

Chemicals	**Brand**	**Molecular weight (M_w, M_n, d)**	**Purity**	**Structure**
Polyacrylonitrile, (PAN)	J&K Scientific	$M_w = 150{,}000$	–	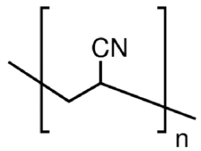
Polyvinylidene fluoride, (PVdF)	Arkema, HSV900	d = 1.78 g/cm^3	–	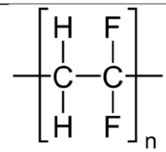
Poly(dimethylsiloxane), (PDMS)	Sigma-Aldrich	viscosity ~65 cSt, M_n = 2750 g/mol	–	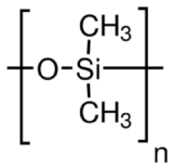

Table 3.1. (Continued)

Poly(ethylene glycol) diacrylate, (PEGDA)	Sigma-Aldrich	$M_n = 575$	–	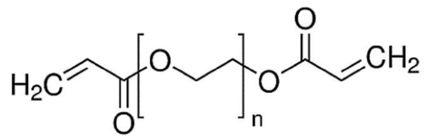
Trimethylolpropane ethoxylate triacrylate, (ETPTA)	Sigma-Aldrich	$M_n \sim 428$	–	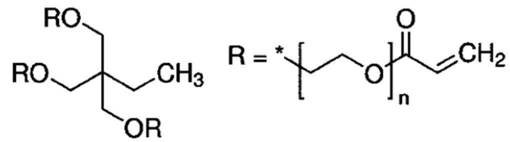
Lithium bis(trifluoromethane)sulfonimide, (LiTFSI)	Sigma-Aldrich	$M_w = 287.09$ g/mol	99.95%	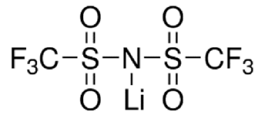
Acryloyl chloride, (AC)	Sigma-Aldrich	$M_w = 90.51$ g/mol	≥ 97%	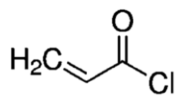
Trichloromethane, (Chloroform)	Sigma-Aldrich	$M_w = 119.38$ g/mol	≥ 99.5%	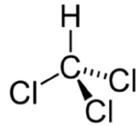
Dichloromethane, (DCM)	Sigma-Aldrich	$M_w = 84.93$ g/mol	≥ 99.8%, anhydrous	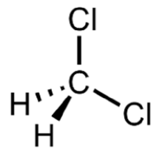

Table 3.1. (Continued)

Tetrahydrofuran, (THF)	AppliChem	M_w = 72.11 g/mol	≥ 99.9%, anhydrous	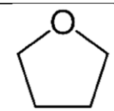
Triethylamine, (Et_3N)	Sigma-Aldrich	M_w = 101.19 g/mol	≥ 99.0%	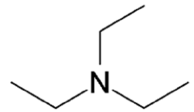
4-Dimethylaminopyridine, (DMAP)	Sigma-Aldrich	M_w = 122.17 g/mol	≥ 99%	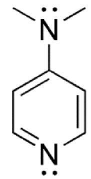
2-hydroxy-2-methylpropiophenone, (HMPP)	Sigma-Aldrich	M_w = 164.20 g/mol	≥ 97%	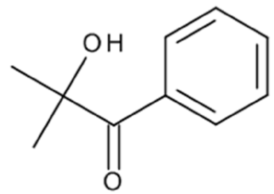
N,N-Dimethylformamide, (DMF)	Sigma-Aldrich	M_w = 203.32 g/mol	99%	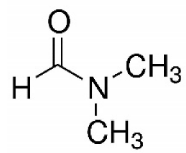

Table 3.1. (Continued)				
N-methyl-2-pyrrolidone, (NMP)	Sigma-Aldrich	M_w = 99.13 g/mol	99.5%	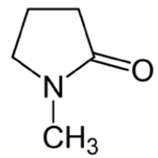
Sulfur	Tengizchevroil	M_w = 32.07 g/mol	98%	S
Ketjen Black, (KB)	MTI Co.	M_w = 12.01 g/mol	99.5%	C
Potassium carbonate	Sigma-Aldrich	M_w = 138.21 g/mol	≥ 99.0%, anhydrous	K_2CO_3
Magnesium sulfate	Sigma-Aldrich	M_w = 120.37 g/mol	99.5%, anhydrous	$MgSO_4$
Multi-walled carbon nanotubes, (CNT), OD: 10-20 nm	US Research Nanomaterials	M_w = 12.01 g/mol	> 95%	C
Conductive acetylene black, (AB)	Arkema	M_w = 12.01 g/mol	–	C

3.2. Characterization Methods and Used Equipment Types

The common methodology and various equipment for investigation/characterization are briefly described below.

Electrospinning method. Electrospinning is a technique, which enables the production of polymer fibers from polymer solutions in high electric fields. PAN nanofibers and PAN nanofibers with sulfur were fabricated by Inovenso Ne200 electrospinning machine.

Ball mill. Fritsch, Pulverisette 7 ball mill was used as a grinding equipment. Rigid balls from zirconia with 2 mm diameters were used to grind S/C powder in ethanol with a mass ratio of powder to ball 1/3.

Tubular furnace. This equipment is used to heat, pyrolyze or carbonize raw materials at high temperatures in air or inert atmosphere. Across International, STF1200 furnace with quartz tube was used for heat treatment of composite materials and nanofibers during the preparation of sulfur-based cathode and nanofiber current collector.

CHNS analyzer. The analyzer determines the mass fraction of carbon, hydrogen, nitrogen and sulfur in organic compounds The sulfur content in electrodes was determined using CHNS chemical analysis, Vario Micro Cube, Elementar.

Filed-Emission Scanning electron microscopy (FESEM). Ultra-high resolution images of all samples were conducted by FESEM, JEOL JSM-7500F equipment. The morphology, surface structure, and cross-section images of nanofibrous materials, polymer films and powders were obtained.

Scanning electron microscope with energy dispersive X-ray spectroscopy (SEM-EDX). The distribution of sulfur in S/DPAN/CNT nanofiber composite and distribution of a-PDMS in cross-linked polymer films were investigated by SEM-EDX analysis using FESEM, JEOL JSM-7500F.

Raman spectroscopy. The structural features of carbonized PAN nanofibers were examined by Raman spectroscopy on a LabRAM HR Evolution spectrometer (HORIBA Scientific, Japan) using Ar^+ ion excitation laser. The spectra of the films were obtained at the laser wavelengths of 633 nm.

Fourier Transform Infrared Spectroscopy (FTIR). The chemical structure of organic samples was investigated by taking FTIR spectra in the range of 400–4000 cm^{-1} using Nicolet iS10 FT-IR, and Agilent Technologies Cary 600 Spectrometers.

X-ray diffraction (XRD). The phase composition of the S, C, S/KB, S/PAN/KB and S/DPAN/KB composites was studied using XRD, SmartLab, Rigaku Co., Japan, (Cu Kα radiation) over a range from 10 to 80°.

X-ray photoelectron spectroscopy (XPS) was used to characterize the chemical composition of the S/DPAN/KB nanofibers. Chemical state of C, S in the composite electrode was determined by surface and point analysis techniques using Thermo Fisher Scientific K-Alfa+ XPS equipment.

Transmission electron microscopy (TEM) analysis were carried out in JEOL JEM - 1400 Plus. Size and morphology of nanofiber materials were investigated by TEM analysis. Samples were dispersed in ethanol, dropped on 400 mesh Cu grid and dried for TEM analysis.

Thermo-gravimetric analysis (TGA). Simultaneous Thermal Analyzer (STA) 6000 was used to analyze the thermal stability of developed cross-linked polymers. The temperature range for all samples was 20–700 °C under nitrogen atmosphere with a heating rate of 10 °C min^{-1}.

Differential scanning calorimetry (DSC). T_g of the materials was determined by DSC, Pyris Diamond DSC equipment. The samples were cooled down to -80 °C, then heated with a rate of 10 °C min^{-1} up to 100 °C. The same condition was used for each sample and the heat flow value was collected from the second heating cycle.

Tensile stress-strain tests. Mechanical properties of freestanding SPEs were analyzed by standard tensile stress-strain tests to measure modules, ultimate tensile strength and elongation at break. The tensile measurements were performed at room temperature on a Materials Testing Machine Z010/TN2S, using a crosshead/an elongation speed of 1 mm/min.

UV lamp. Crosslinking reaction of polymer films was carried out with UV-crosslinking method. Compact Spectroline, ENF-240C/FE UV lamp with λ_{max} = 365 nm was used for all cross-linked samples.

Temperature test chamber. The electrochemical performance of SPEs was tested in a temperature range 25-90 ^{o}C. Temperature test chamber from Xi'an LIB Environmental Simulation Ind. was used during the test.

Cell assembling

Coin cell assembling. For investigation of electrochemical performance of prepared electrode, current collector and SPE materials, CR2032 coin type cells were assembled inside the Ar-filled glove box (MBRAUN, LABmaster Pro Glovebox, <0.1 ppm H_2O and O_2). Lithium metal discs were used as both negative and reference electrode, and polypropylene membrane as a separator, $LiPF_6$ in EC/DMC/DEC (volume ratio of 1:1:1,Targray) as an electrolyte. Disc cutter with 19 mm diameter punching tool was used for separator, and 15 mm for the cathode. The general configuration of the cell is shown in Figure 3.1 a.

Pouch cell assembling. Pouch-type cell was assembled in the argon filled glovebox with one layer of Li metal anode and two layers of flexible nanofiber cathode with dimensions of 25x30 mm separated by a porous polypropylene membrane as shown in Figure 3.1 b. A special, moisture-resistant aluminum laminated film was used to prepare pouch cell cases. After inserting all components into the pouch form, liquid electrolyte is injected from an open side (only one side) of battery pouch. The electrolyte-soaked battery pouch is heat-sealed under vacuum, removing excess gas from inside the pouch. Battery bending and folding tests were done by powering light-emitting diodes (LEDs) with pouch cells.

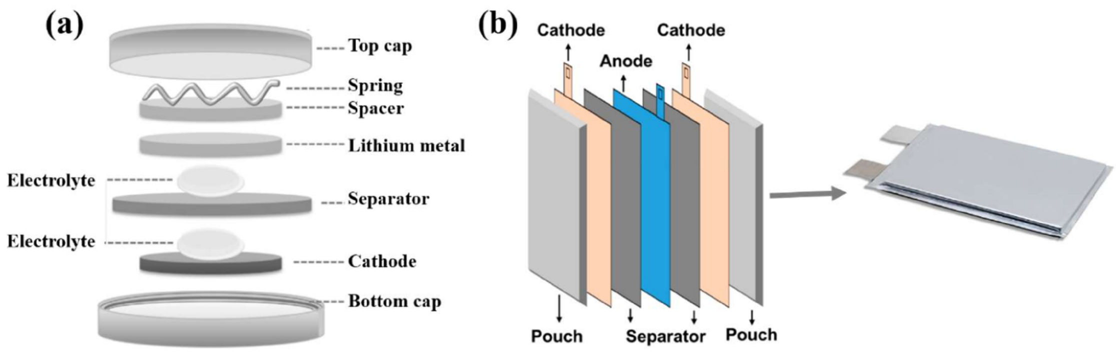

Figure 3.1. Scheme of the (a) coin cell and (b) pouch cell configuration.

Testing electrochemical performance of the cells

Cyclic voltammetry (CV). BioLogic Science Instruments (France) was used to get CV of the electrodes. Linear sweep cyclic voltammetry (LSV) method measures the cell current as a result of a potential change in the range of the working electrode (at a given scan rate). Redox reactions of an electrode, the presence of intermediates and reversibility of the reaction were studied by CV. Cyclic voltammogram of an electron reduction (cathodic) and oxidation (anodic peak) is shown in Figure 3.2 a [87].

Galvanostatic charge/discharge cycling. The capacity and cycling performance of the electrode materials were obtained from the charge/discharge potential profiles. Coin cell type batteries were tested in BT-2000 Arbin Instruments (USA) by applying constant current. As an example, typical potential profile for S/C electrode is shown in Figure 3.2 b [88].

Rate capability (C-rate) tests of electrode materials were investigated at different range of current density in BT-2000 Arbin Instruments (USA). It is a measure of the rate at which a battery is discharged relative to its maximum capacity. A 1 C rate means that the discharge current will discharge the entire battery in 1 h [11].

Electrochemical impedance spectroscopy (EIS). The ionic conductivity of SPEs was determined by EIS using VMP-3 potentiostat/galvanostat (Bio-Logic Instruments) equipment. The impedance of the cell with SPEs was measured as a function of frequency in a range of 1 MHz to 10 Hz, and ionic conductivities of the samples were calculated according to the Nyquist plot. Typical Nyquist plot for a SPEs are given in Figure 3.2 c [89].

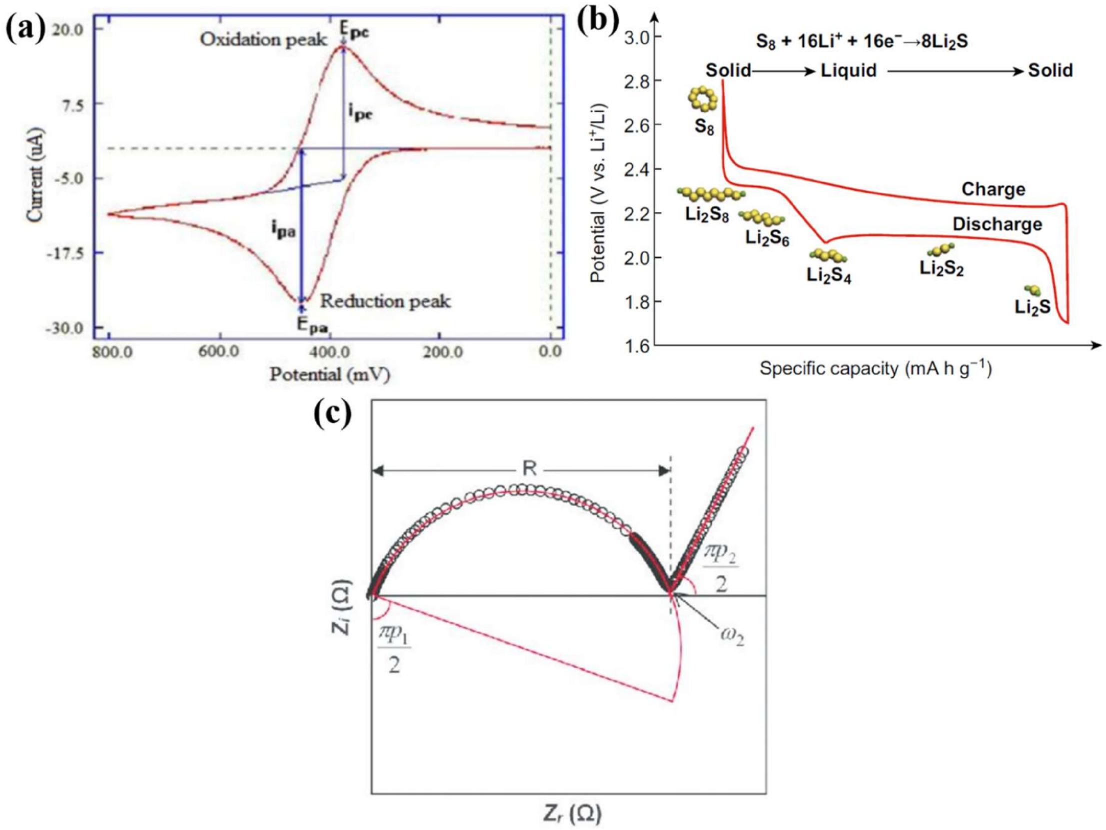

Figure 3.2. Typical (a) CV showing anodic and cathodic current peaks [87], (b) charge/discharge profile for a Li–S battery [88], and (c) Nyquist plot for a polymer electrolyte [89].

The photographs of basic equipment used during the research are shown below.

Basic Equipment Used for Material Preparation, Battery Assembling and Testing

Electrospinning Machine

Tubular Furnace

Planetary Ball Mill

Disassembling Machine

Glove Box

Disc Cutter

Coin Cell Crimper

Battery Test Equipment,
BT-2000 Arbin Instruments

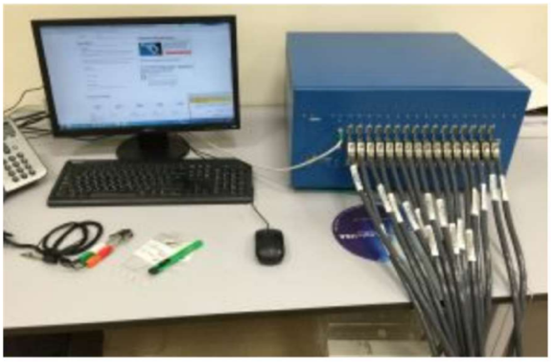

Potentiostat/galvanostat/EIS – VMP3
Bio-Logic Instruments

3.3. Experimental Part

Experimental part comprises the synthesis, preparation procedures of new materials, and application methods. The general information and motivation for the work were reviewed in Chapter 2, Part 2.3 выше. Experimental part was divided into three subsections.

In **subsection 3.3.1,** preparation and characterization of S/DPAN/KB flexible nanofiber composite cathode were described. Flexibility and bendability of the electrode was also studied by assembling pouch cell.

In **subsection 3.3.2,** the fabrication of 3D structured current collector for Li/S batteries was explained in detail. Carbon nanofibers were obtained by electrospinning method with different diameters, void sizes and investigated as a current collector in comparison with conventional ones.

The next **section 3.3.3** covers preparation of PDMS-based SPEs with UV-photocrosslinking process. Electrochemical performance of electrolytes was studied.

3.3.1. Freestanding flexible S/DPAN/KB cathode by electrospinning method

The development of binder-free, freestanding, and flexible sulfur electrode is highly desired to assemble Li/S batteries with high volumetric energy and power density, as it was mentioned above in Chapter 2, section 2.3.1. Here, we prepared the PAN nanofibers filled with S/KB particles (denoted as S/PAN/KB, where KB is Ketjen Black) by a single nozzle electrospinning technique. Further S/PAN/KB nanofibers were heated at 300 ^{o}C temperature to make PAN dehydrogenated, sulfurized, and, therefore, conductive. Benefitting from its structural features, the as-prepared S/DPAN/KB nanofiber cathode exhibited good compatibility with the conventional carbonate-based electrolytes and showed a high coulombic efficiency, long cycle life and good rate capability, demonstrating a great prospect for battery applications.

3.3.1.1. S/KB composite preparation

KB was used as conducting matrix to prepare S/KB composite. S/KB composite was prepared by mixing sulfur and KB in a weight ratio of 95:5, and heat treating in a tubular furnace at 300 ^{o}C in argon for 4 h. After cooling down, the resulting sulfur impregnated KB composite was ground by ball milling for 4 h at 600 rpm. The ball milled composite was used further to prepare the spinning solution.

3.3.1.2. Fabrication of S/DPAN/KB nanofiber composite electrode

Schematic illustration of the electrospinning process is shown in Figure 3.3. The spinning solution was prepared by dissolving 1 g of PAN in 9 g DMF and continuous overnight stirring. S/KB composite was homogeneously dispersed in the PAN solution by sonication for 5 h. Optimized weight ratio of PAN, S/KB composite was 2:3. Dispersed solution was loaded into 10 ml syringe with a stainless steel nozzle and spun by applying voltage of 17 kV with a solution flow rate of 1 mL h^{-1}. The distance between rotating cylinder and nozzle tip was kept as 12 cm. Nanofibers were collected onto a carbon coated aluminum foil (MTI Co.). The obtained S/PAN/KB composite nanofibers were heated in a tubular furnace in Ar with a heating rate of 10 ^{o}C min^{-1} to 300 ^{o}C and kept at this temperature for 1 h to cyclize

PAN polymer chains and sulfurize dehydrogenated PAN in the S/KB composite [90,91]. The resulting S/DPAN/KB nanofiber composite was freestanding, flexible and was directly used as an electrode without any binder.

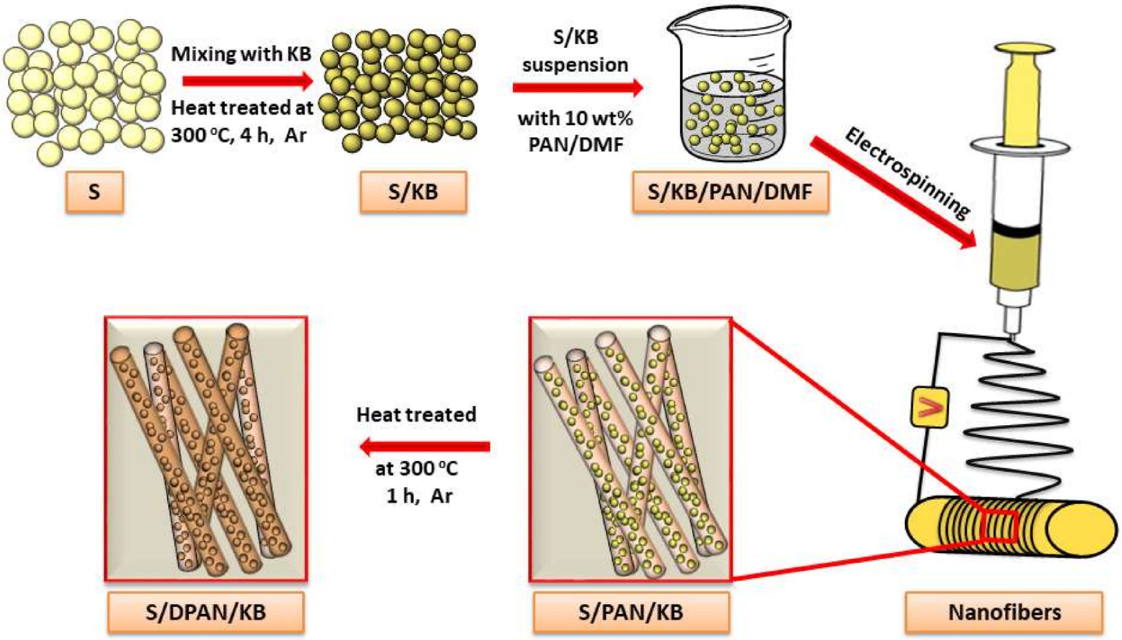

Figure 3.3. Schematic illustration of electrospinning process and fabrication of flexible S/DPAN/KB composite cathode.

3.3.1.3. Characterization of S/DPAN/KB nanofiber composite electrode

The morphologies of the samples were characterized by FESEM, SEM/EDS. XRD, XPS and FTIR were used to characterize the structural properties of the samples. The sulfur content was determined using CHNS analyzer.

All the electrochemical tests were carried out in an argon filled glovebox (MasterLab, MBraun) using coin-type cells (CR2032), with lithium metal discs as both negative and reference electrode, polypropylene membrane as a separator (Celgrad 2400) and a liquid electrolyte $LiPF_6$ in ethylene EC:DMC:DEC (volume ratio of 1:1:1, Targray). The prepared S/DPAN/KB nanofiber composite was cut into disks of 1 cm in diameter and used as a freestanding cathode to assemble the cells. The cells were galvanostatically cycled at different current densities in a potential range of 1.0 – 3.0 V *vs*. Li/Li^+ on multichannel battery tester. Specific capacity and current density were calculated based on the weight of sulfur in the electrode. CV was conducted over a potential range from 1 to 3 V *vs*. Li/Li^+ at a scan rate of 0.1 mV s^{-1}. All the electrochemical measurements were carried out at room temperature. For comparison, a conventional S/DPAN/KB cathode on Al foil current collector was also prepared and tested under similar conditions. In this case, 80 wt% of S/DPAN composite, 10 wt% KB and 10 wt% PVdF were dispersed in NMP. The resulting slurry was applied onto Al foil using doctor blade technique and vacuum dried at 60 ºC for 12 h. In addition, S/KB composition was prepared with the same method in order to compare with S/DPAN systems. Specific capacity and current density were calculated based on the weight of sulfur in the electrode. The mass loading of sulfur was around 1.5 mg cm^{-2} for all samples. In all experiments the area of the cathode was 1.76 cm^2. For bending test, the pouch-type cell was assembled in the argon filled glovebox with one layer of Li metal anode and two layers of freestanding S/DPAN/KB nanofiber composite cathode with dimensions of 25x30 mm separated by porous polypropylene membrane.

3.3.2. PAN derived electrospun carbon nanofibers as 3D current collector for Li/S batteries

Carbon fibers are promising materials in fabrication of lightweight, 3D structured high performance active electrodes. Particularly, they can be favorable for sulfur-based electrodes, which suffer from low conductivity, volume expansion, and low active material loading. In most of the reported studies on 3D carbon current collectors commercial CFs with diameters of more than 5 μm were investigated [28,35,92,93]. The larger diameters result in a higher electrical resistivity of the carbon fibers. Additionally, it results in increased weight and decreased specific surface area of a current collector. Fabrication of CFs with the diameters less than 2 μm could be more beneficial from this point of view.

One of the feasible methods of production CFs is a spinning of polymer precursors [94]. However, conventional mechanical spinning techniques cannot produce fibers with diameters smaller than 2 μm. In contrast to mechanically-driven spinning, electrospinning technology enables production of homogenous, continuous polymer fibers from polymer solutions with diameters in nanometer range at high electric fields [95]. Electrospinning is a potential way of CF production for development of 3D current collectors. In addition, this method is one of the simplest and cost effective techniques to produce CNFs [61].

Herein, we present the fabrication and investigation of electrospun carbon nanofibers with different diameters, void sizes and their application as 3D current collector for sulfur composite electrode. The capacity of sulfur cathode was remarkably enhanced by replacing heavyweight metal current collector with 3D structured CNFs fabricated by simple electrospinning method. The variation of the electrospinning solution concentration allowed to obtain carbonized PAN (cPAN) nanofibers of uniform structure with diameter from several hundred nanometers to several micrometers.

3.3.2.1. Fabrication of carbon nanofibers by electrospinning method

Carbon nanofibers were fabricated by electrospinning apparatus. The homogenous spinning solutions of PAN with the concentrations of 10, 12 and 14 wt% in DMF were prepared by stirring overnight and abbreviated as PAN10, PAN12, PAN14 respectively. The polymer solutions were spun at room temperature for 1 h in an air atmosphere by applying voltage of 17 kV with a solution flow rate of 1 mL h^{-1}. The distance between rotating cylinder and tip of the capillary was 13 cm. A rotating cylinder was covered by an aluminum foil and rotational speed during electrospinning was set at 100 rpm. The stabilization and carbonization of obtained PAN nanofibers were conducted in a tubular furnace. A constant flow of air was maintained through the furnace during the stabilization. The stabilization was carried out by heating the PAN nanofibers from the room temperature to 280 ºC with the heating rate of 5 ºC/min, followed by holding the temperature at 280 ºC for 1 h to complete the stabilization. The stabilized PAN nanofibers easily peeled from the aluminum foil and carbonized under argon atmosphere at temperatures from 600 to 800 ºC for 4 h with the heating rate set at 10 ºC min^{-1}. The mass per unit area of the carbon nanofiber was about ~ 0.85 mg cm^{-2}.

3.3.2.2. Application of CNFs as 3D current collector for S/DPAN/CNT cathode

S/DPAN/CNT composite was synthesized by previously reported method of our group [96]. First, S with PAN in a weight ratio of 75:25 and CNT (2 wt% of total mass) was manually grinded. Further, the mixture was heat treated in a tube furnace at 300 ºC for 4 h in argon atmosphere to form S/DPAN/CNT composite. The slurry was prepared from 80 wt% S/DPAN/CNT composite, 10 wt% AB and 10 wt% PVDF mixed in NMP. The resulting slurry of S/DPAN/CNT were applied to prepared electrospun CNFs by vacuum infiltration technique and dried in a vacuum oven at 60 °C for 12 h.

For comparison, a conventional S/DPAN/CNT cathode on commercial CF and Al foil were also prepared and tested under similar conditions. In this case, 80 wt% of S/DPAN/CNT composite, 10 wt% AB and 10 wt% PVdF were dispersed in NMP. The resulting slurry was casted on Al foil and commercial CF by using doctor blade technique. Specific capacity and current density were calculated based on the weight of sulfur in the electrode.

3.3.2.3. Structure characterization and electrochemical measurements

The morphologies of the samples were characterized by FESEM. XRD and Raman spectroscopy were used to characterize the structural properties of the samples. The sulfur content in the composites was determined using CHNS analyzer.

S/DPAN/CNT composite cathodes incorporated with cPAN CNF current collector were used as working electrodes after vacuum drying at 60 ºC overnight. The areal mass loading of sulfur for all samples was 1.2 ± 0.2 mg cm^{-2}. The coin-type cells (CR2032) were assembled in an argon filled glovebox using lithium metal discs as both negative and reference electrode, polypropylene membrane as a separator (Celgrad 2400) and $LiPF_6$ EC:DMC:DEC (volume ratio of 1:1:1) as an electrolyte. CV was conducted over a potential range from 1 to 3 V vs. Li^+/Li at a scan rate of 0.1 mV s^{-1}. Galvanostatic charge−discharge was carried out on a multichannel battery tester within the voltage range of 1.0 − 3.0 V (vs. Li^+/Li). The specific capacity and current density were calculated based on the weight of sulfur in the electrode. All the electrochemical measurements were carried out at room temperature.

3.3.3. Flexible siloxane-based solid polymer electrolyte

The development of flexible solid-state electrolytes and their compatibility with electrodes are important issues of flexible LIBs. SPEs are full of promise among solid-state electrolytes due to their excellent flexibility, high thermal and electrochemical stability and lack of organic solvents. Particularly, polysiloxane based SPEs are advantageous, and were briefly discussed in Chapter 2, section 2.3.2. Flexibility of Si-O-Si bonds and low T_g improve bending properties and enhance Li-ion conduction of polysiloxane based SPEs. Here, we prepared a series of freestanding, transparent polymer films with excellent flexibility and improved ionic conductivity at ambient temperature. Cross-linked SPEs were obtained by UV-curing of ethylene glycol unit containing oligomers and acrylated PDMS with different mass ratios. Electrochemical and mechanical properties of films were investigated.

3.3.3.1. Acrylation reaction of hydroxyl terminated PDMS

The terminal groups of HO-$(PDMS)_n$-OH were converted to photosensitive acrylate groups (OAc) by reaction with acryloyl chloride to obtain AcO-$(PDMS)_n$-OAc (a-PDMS) polymers by the reported method [97]. HO-$(PDMS)_n$-OH (16.5 g, 6 mmol) and DMAP (0.00732g, 0.06 mmol) was dissolved in $CHCl_3$ (35 ml), placed in a 500 mL round bottom flask and mechanically stirred by overhead stirrer under flow of N_2 gas. After gradually adding Et_3N to the solution, acryloyl chloride was added dropwise over 30 minutes. The mixture was refluxed at 50 °C for 24 h with mild stirring. The $CHCl_3$ was removed by rotary evaporator and residual viscous product dissolved in ethyl acetate. Triethylamine hydrochloride salts were removed from the product by vacuum filtration and ethyl acetate was removed under reduced pressure. The remaining product dissolved in CH_2Cl_2 (80 – 100 mL) and washed with 2M K_2CO_3 solution (15 mL). The isolated viscous solution was dried with $MgSO_4$, filtered out, and solvents were removed under reduced pressure. The reaction scheme of PDMS acrylation is given in Figure 3.4. FTIR spectroscopy results confirmed acrylation of HO-$(PDMS)_n$-OH.

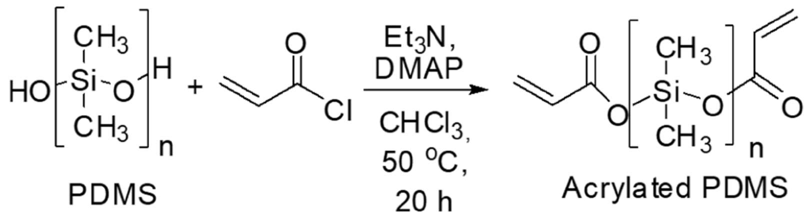

Figure 3.4. The acrylation of hydroxy terminated PDMS.

3.3.3.2. Preparation of flexible polymer films with lithium salt

SPEs composed of a-PDMS, PEGDA, ETPTA and Li salt (LiTFSI) were prepared by UV-crosslinking method. In the first step, homogenous mixture of a-PDMS, PEGDA, and ETPTA were prepared in various stoichiometric mass ratios by stirring at room temperature and abbreviated as PPE. Separately, LiTFSI dissolved in THF with the mass ratio of 2:1 respectively and mixed with PPE blend under continuous stirring for 30 minutes. The molar ratio of [EO]/[Li^+] was varied as 6, 18, and 30. HMPP was used as a photoinitiator, and the concentration was fixed as 3 wt% of total solution. Further, the sample cast between two glass plates to prepare thin polymer films. The casted samples exposed to UV-irradiation for 3 minutes by UV lamp. Prepared cross-linked polymer films were easily removed from the glass plate and placed into vacuum chamber with a heater in the glove box for 24 h at 50 ℃ in order to remove residual solvent. The overall process performed in an argon-filled glove box.

3.3.3.3. Characterization of solid polymer electrolytes

The UV photocrosslinked polymer membranes were investigated by FTIR with a resolution of 16 cm^{-1} and frequency range of 400-4000 cm^{-1}. The gel content of the samples was determined by measuring the weight of the samples before and after solvent extraction in acetone at room temperature for 24 h. Insoluble residue was dried in vacuum oven at 60 °C and the gel content was calculated. The morphologies were characterized by FESEM and SEM/EDS. T_g of the materials was determined by DSC. The samples were cooled down to – 100 °C, then heated with a rate of 10 °C min^{-1} up to 100 °C. The same condition was used for each sample and the heat flow value was collected from the second heating cycle. The thermal stability was tested by TGA in a temperature range of 20–800 °C under nitrogen atmosphere with a heating rate of 10 °C min^{-1}. Mechanical properties of freestanding SPEs were analyzed by standard tensile stress-strain tests to measure modules, ultimate tensile strength and elongation at break. The tensile measurements were performed at room temperature, using a crosshead/an elongation speed of 1 mm/min.

The ionic conductivity of prepared SPEs was determined by EIS. The coin cells (CR2032) were assembled with cross-linked PPEs sandwiching between two stainless steel (SS|PPE|SS). The impedance measurements were carried out from 1 MHz to 10 Hz with a voltage of 0.1 mV in amplitude from room temperature to 90 °C with a temperature interval of 10 °C. The ionic conductivities were calculated by following equation;

$$\sigma = l \,/\, (R_b \cdot r^2 \cdot \pi)$$

where l is the thickness, r and R_b represent radius and bulk resistance of the cross-linked SPEs respectively. R_b is the intercept on the real axis at the high frequency end of the Nyquist plot of complex impedance. The electrochemical stability was measured by assembling coin cell with a stainless steel as a working, Li metal as a reference electrode, cross-linked PPEs as electrolyte and tested at 60 °C with a potential window between 1.5 V to 7.0 V at a scan rate of 0.1 mV s^{-1}. In addition, cyclic voltammetry measurements were done with similar cells at 60 °C with a potential window between - 1.5 V and 1.5 V at a scan rate of 1 mV s^{-1}. All measurements were carried out by using analyzer VMP-3 potentiostat/galvanostat (Bio-Logic Instruments) and coin cells were assembled in an argon-filled glove box (MasterLab, MBraun). Temperature chamber was used for testing at different temperatures.

4. RESULTS AND DISCUSSION

4.1. Freestanding Flexible S/DPAN/KB Cathode by Electrospinning Method

Flexible freestanding S/DPAN/KB cathode for lithium-ion sulfur batteries was prepared by electrospinning technique. The maximum content of sulfur allowed to prepare and maintain stable in flexible S/PAN/KB nanofibers was 54 wt%. In order to achieve 54 wt% S content, PAN and S/KB composite ratio in the DMF solution was varied. It was found that the optimal weight ratio of PAN to S/KB in the spinning solution is 2:3. After the heat treatment of S/PAN/KB nanofibers at 300 ºC for 1 h, the content of sulfur in the composite decreased to 30 wt% due to the sublimation of sulfur. The sulfur content was determined using a CHNS analyzer which is presented in Table 4.1. The partially pyrolyzed and cyclized conductive PAN stabilizes sulfur and suppresses its dissolution into electrolyte [59,90].

Table 4.1. Results of CHNS analysis of the S/PAN/KB and S/DPAN/KB nanofiber composites.

	N [wt%]	**C [wt%]**	**H [wt%]**	**S [wt%]**
S/PAN/KB	10.04 ± 0.10	34.10 ± 0.10	2.23 ± 0.10	54.31 ± 0.10
S/DPAN/KB	14.79 ± 0.10	54.13 ± 0.10	0.90 ± 0.10	30.24 ± 0.10

The phase composition of the S/KB, S/PAN/KB and S/DPAN/KB composites was studied using XRD. The XRD patterns of these composites are shown in **Figure 4.1.** XRD patterns of KB, PAN, sulfur, S/KB, S/PAN/KB and S/DPAN/KB composite nanofibers.Figure 4.1 along with the patterns of the starting S, KB and PAN components. One can see that KB shows a characteristic diffraction peaks with low intensities between 20 and 27 2θ while pristine S exhibits sharp and intense diffraction peaks between 10 and 60 2θ, which indicates its crystalline state. A strong peak at the 2θ = 16.9 observed in the XRD pattern of PAN is due to its crystallinity as well. In the case of the S/KB composite and S/PAN/KB nanofibers, the peaks of crystalline S are still visible but their intensities are substantially reduced due to the uniform distribution of sulfur in the KB and PAN. The characteristic peaks of crystalline sulfur were not observed after heat treatment of the S/PAN/KB nanofibers in which the content of sulfur was 30 wt%. It indicates that sulfur is amorphous and homogeneously distributed in the S/DPAN/KB matrix and could be bound with dehydrogenated PAN during the heat treatment as mentioned in our previous reports [98]. Also, Myung *et al*. proposed that carbon-sulfur chemical bond exists in S/DPAN composites as the interface between sulfur particle and the DPAN layer, which explains the reason for the good electrochemical performances of the S/DPAN/C composites [99]. The FTIR spectra also support a suggestion of formation of heterocyclic compound in the process of dehydrogenation of PAN with sulfur (Figure 4.2). In the FTIR spectrum of PAN shown in Figure 4.2 the peaks at 2244 cm^{-1} and 1454 cm^{-1} represent the –CN and $–CH_2$ groups, respectively. In the obtained S/DPAN/KB composite these characteristic peaks disappear and a new peak appears at 1494 cm^{-1}, which corresponds to a C=C double bond, and a peak at 1358 cm^{-1} is due to a –CH deformation. The peaks at 1427 cm^{-1} and 800 cm^{-1} indicate the formation of cyclic structure during the heat treatment of S/PAN/KB. As reported by J. Wang *et al*., during the heating process sulfur dehydrogenates PAN, which results in forming a conductive chain and the –CN functional groups cyclize in the melt state, resulting in a thermally stable heterocyclic compound, in which elemental sulfur is embedded [59].

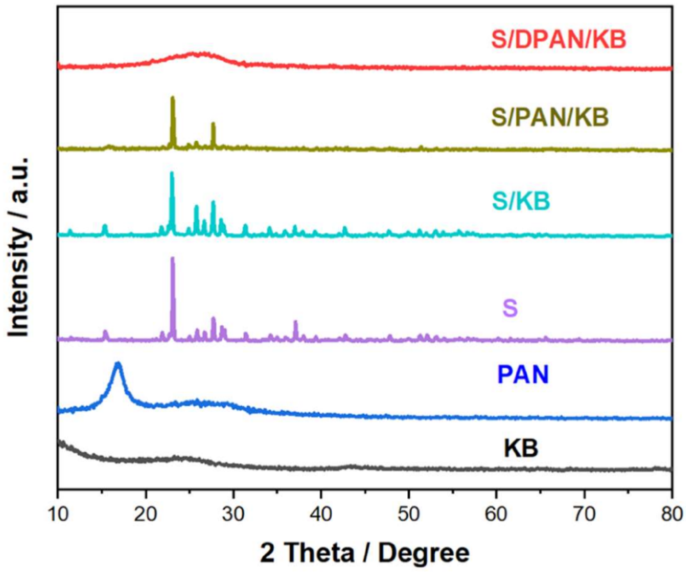

Figure 4.1. XRD patterns of KB, PAN, sulfur, S/KB, S/PAN/KB and S/DPAN/KB composite nanofibers.

XPS was used to characterize the chemical composition of the S/DPAN/KB nanofibers. Figure 4.2 b shows the XPS spectra in the C 1s region. Fitted curves reveal that the C 1s band can be split into three peaks. The main peak at 284.90 eV corresponds to the sp^2-hybridized carbon, the peak at 286.57 eV corresponds to the C–N bonds, and partially to the C–S weak bond as well. The peak at 288.75 eV can be attributed to the C–O species formed by carbon oxidation during the heating process. For the S 2p spectrum (Figure 4.2 c), the peaks at 164.98 eV and 163.61 eV are assigned to S 2p 1/2 and S 2p 3/2 spin-orbit levels of elemental sulfur. The lower binding energy of the S 2p 3/2 state (163.61 eV) than that of elemental sulfur (164.0 eV) indicates the presence of the weak C–S bond in the nanofibers. The minor peak centered at 167.31 eV arises from the sulfate species formed by the oxidation of elemental sulfur during the preparation process. The peak at 161.82 eV can be attributed to the adsorbed H_2S by-product generated in the cyclization reaction of S/DPAN/KB nanofibers.

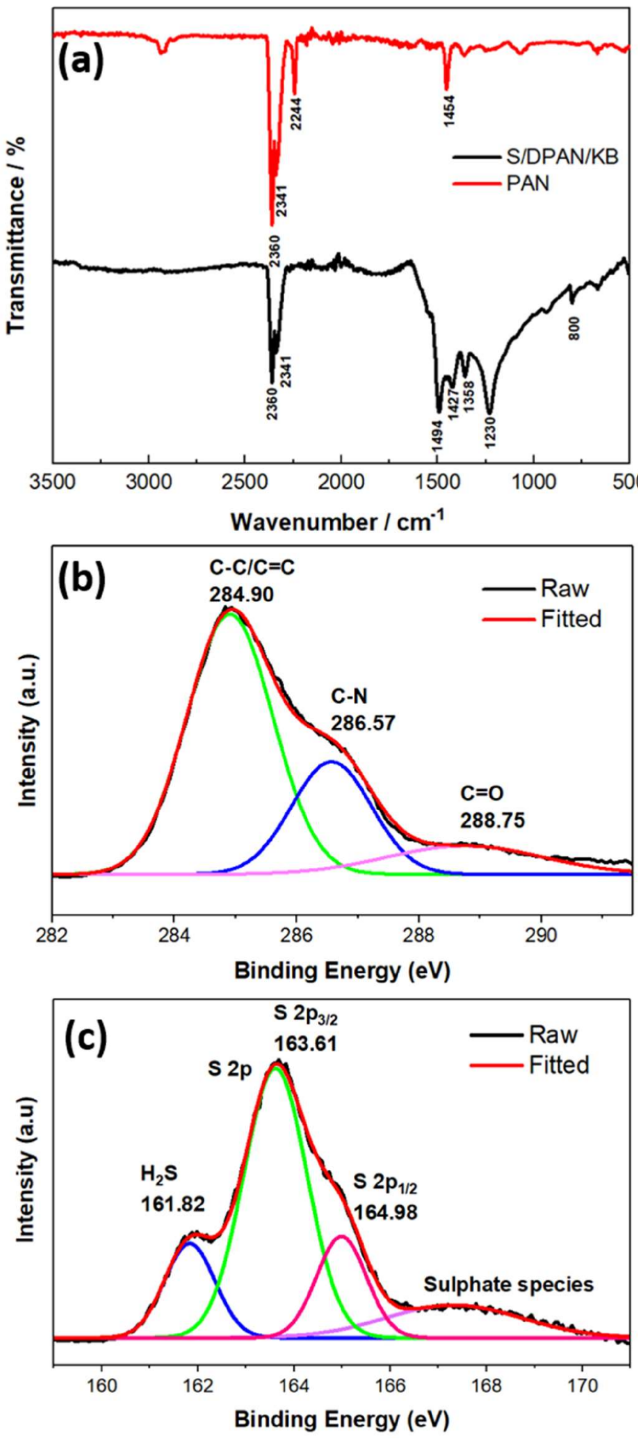

Figure 4.2. (a) FTIR spectra of PAN and S/DPAN/KB, and XPS analysis of S/DPAN/KB nanofibers (b) C 1s spectrum; (c) S 2p spectrum.

The morphology of the as-prepared S/DPAN/KB fibers was investigated using SEM. As observed in the SEM images of both S/PAN/KB and S/DPAN/KB, the obtained fibers have the diameter ranging from 300 to 600 nm, and own a similar morphology and a rough surface due to the presence of S/KB particles (Figure 4.3, c-f).

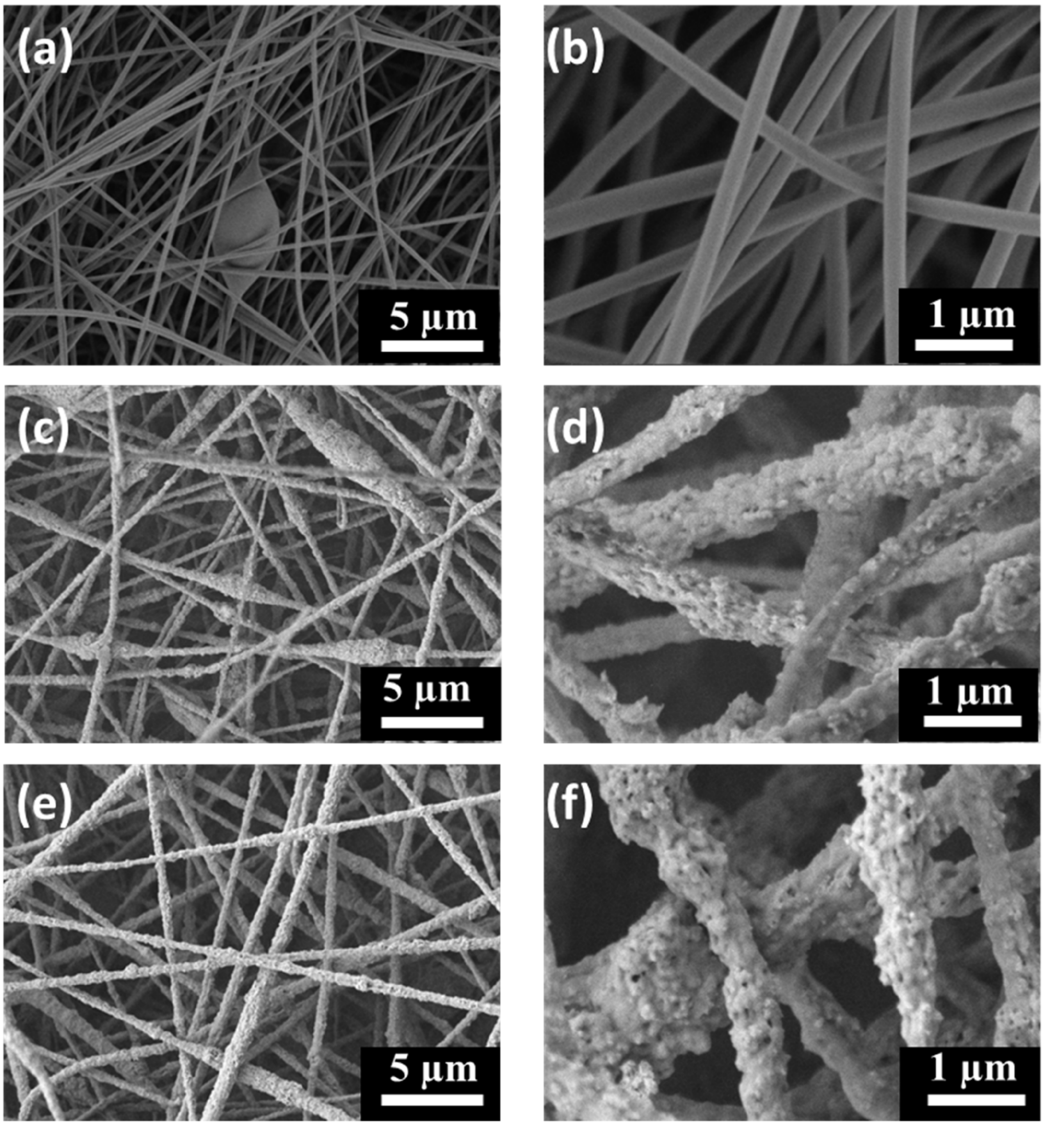

Figure 4.3. SEM images of (a, b) PAN, (c, d) S/PAN/KB nanofibers and (e, f) S/DPAN/KB freestanding composite cathodes.

The fiber diameters are smaller and have no pores only in the case of PAN nanofibers (Figure 4.3, a-b), and this difference with the S/PAN/KB composite was also attributed to the addition of S/KB. Along with this, it shows perceptible pores on the surface of the S/DPAN/KB composite nanofibers which are related with the sublimation of sulfur during the heat treatment and dehydrogenation of PAN, which lead to the formation of these pores and a large weight loss. Figure 4.4 shows TEM image of S/DPAN/KB nanofiber material. The bright spots along the edges of fibers correspond to the pores. The amount of sulfur increased in inner parts of the fibers.

The uniform distribution of components in the fibers was confirmed by SEM/EDS elements mapping in the obtained composites (Figure 4.5). As shown in the first column of Figure 4.5 a, the mapping of sulfur, carbon and nitrogen in the composite indicates that sulfur is uniformly distributed within the PAN fibers, and the S/KB composite was homogeneously mixed before adding to the spinning solution. After the dehydrogenation of the S/PAN/KB composite the S content decreased as explained above, and due to this phenomenon the carbon and nitrogen distribution can be seen more clearly in the SEM/EDS data in the case of S/DPAN/KB (Figure 4.5 b).

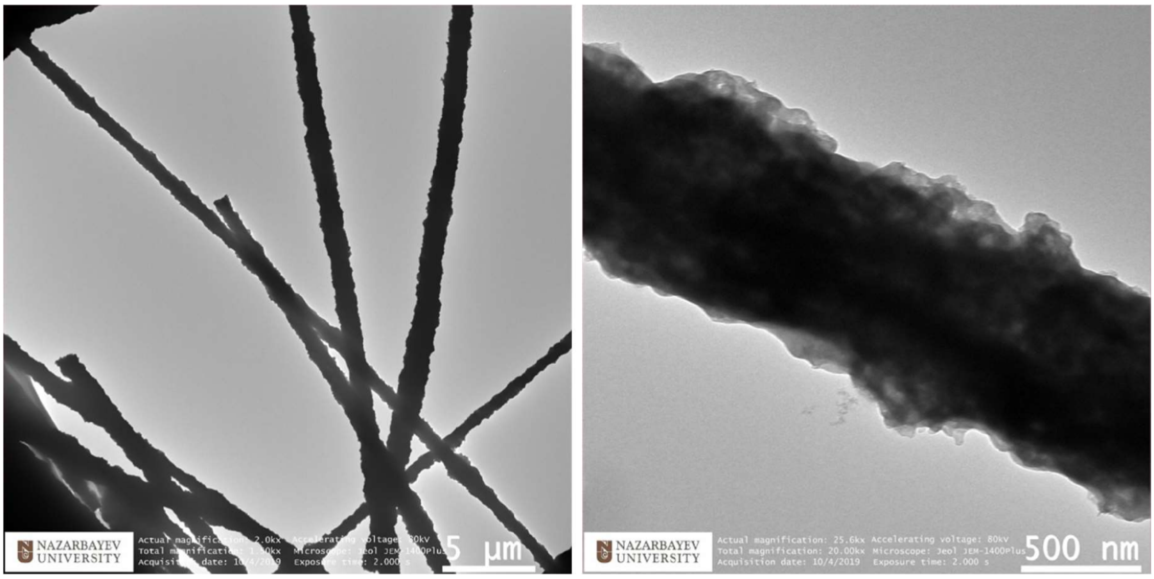

Figure 4.4. TEM images of S/DPAN/KB nanofiber composite.

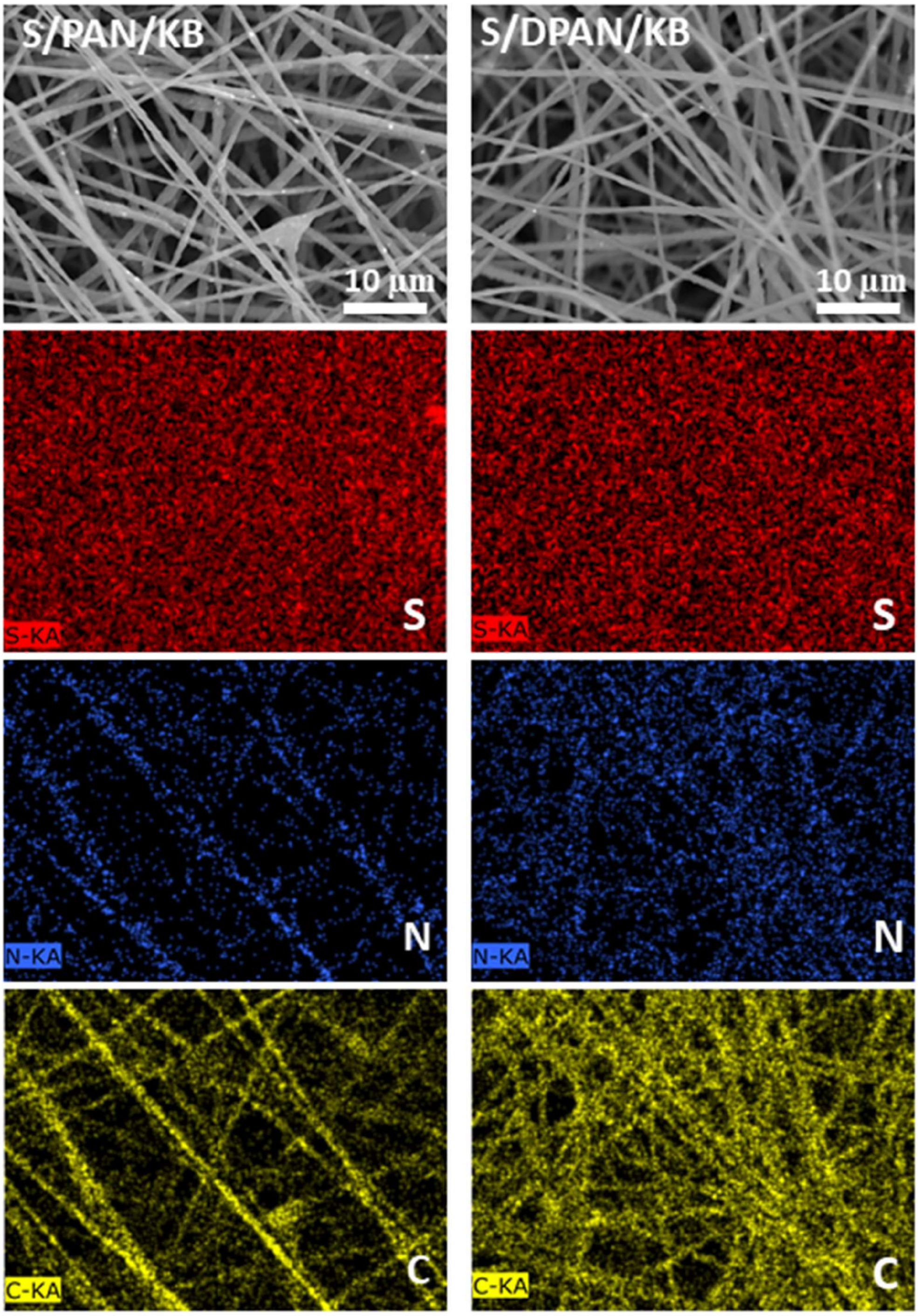

Figure 4.5. SEM/EDS mapping showing the distribution of sulfur (S), nitrogen (N) and carbon (C) in the composites (a) S/PAN/KB with 54 wt% sulfur and (b) S/DPAN/KB with 30 wt% sulfur.

The specific surface area analysis was performed by nitrogen Brunauer-Emmett-Teller (BET) adsorption measurements and Barrett–Joyner–Halenda (BJH) pore size and volume analysis. Figure 4.6 a shows the N_2 sorption/desorption isotherms and Figure 4.6 b presents the pore-size distribution curves of PAN, S/PAN/KB and S/DPAN/KB. S/PAN/KB and S/DPAN/KB exhibit hysteresis curves over a broader range of P/P_0 (0.4–0.9), which is a general characteristic of a mesoporous material. On the other hand, PAN shows a typical type II isotherm which is generally observed in nonporous materials [100]. The BET surface area of PAN obtained by N_2 adsorption analysis is low, 1.26 $m^2\ g^{-1}$. In the case of S/PAN/KB and S/DPAN/KB, the surface areas are around 21.39 $m^2\ g^{-1}$ and 94.73 $m^2\ g^{-1}$, the BJH mean pore diameters are 3.711 nm and 3.717 nm, respectively. After the heat treatment of S/PAN/KB nanofibers, the BET surface area increased due to dehydrogenation of PAN and sublimation of sulfur. The porous structure of the S/DPAN/KB composites can help to avoid the dissolution of polysulfides which is one of the main issues of sulfur-based cathode. It improves the capacity retention by hindering the shuttle effect.

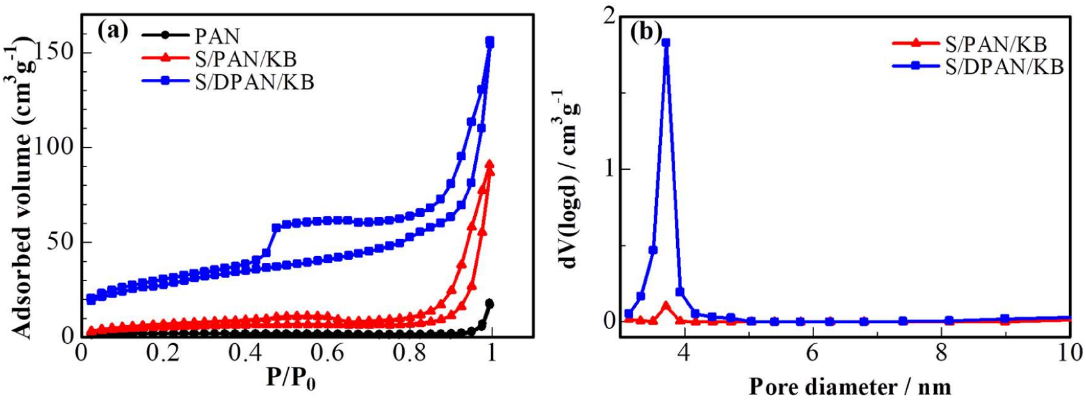

Figure 4.6. (a) N_2 sorption/desorption isotherms of PAN, S/PAN/KB and S/DPAN/KB, and (b) pore-size distributions curve of S/PAN/KB and S/DPAN/KB.

The electrochemical performance of the prepared S/DPAN/KB nanofibers as freestanding cathodes for Li/S batteries were examined in lithium half-cells and compared with the performance of the S/KB and S/DPAN/KB electrodes prepared by slurry casting on Al foil with addition of conductive agent and binder. Figure 4.7 shows the first two CV curves of a cell with (a) S/KB and (b) S/DPAN/KB electrodes on Al foil, and (c) a freestanding nanofiber composite S/DPAN/KB cathode cycled in a potential range of 1.00 – 3.00 V at a scan rate of 0.1 mV s^{-1}. As shown in Figure 4.7 a, the S/KB composite cathode shows two cathodic peaks corresponding to the typical for the S/C composite cathodes two-step conversion reactions. The peak centered at 2.2 V corresponds to the transformation of S_8 to Li_2S_n ($4 \leq n < 8$), while the other peaks centered around 1.8 V correspond to the further reduction of Li_2S_n ($4 \leq n < 8$) to Li_2S/Li_2S_2 [49].

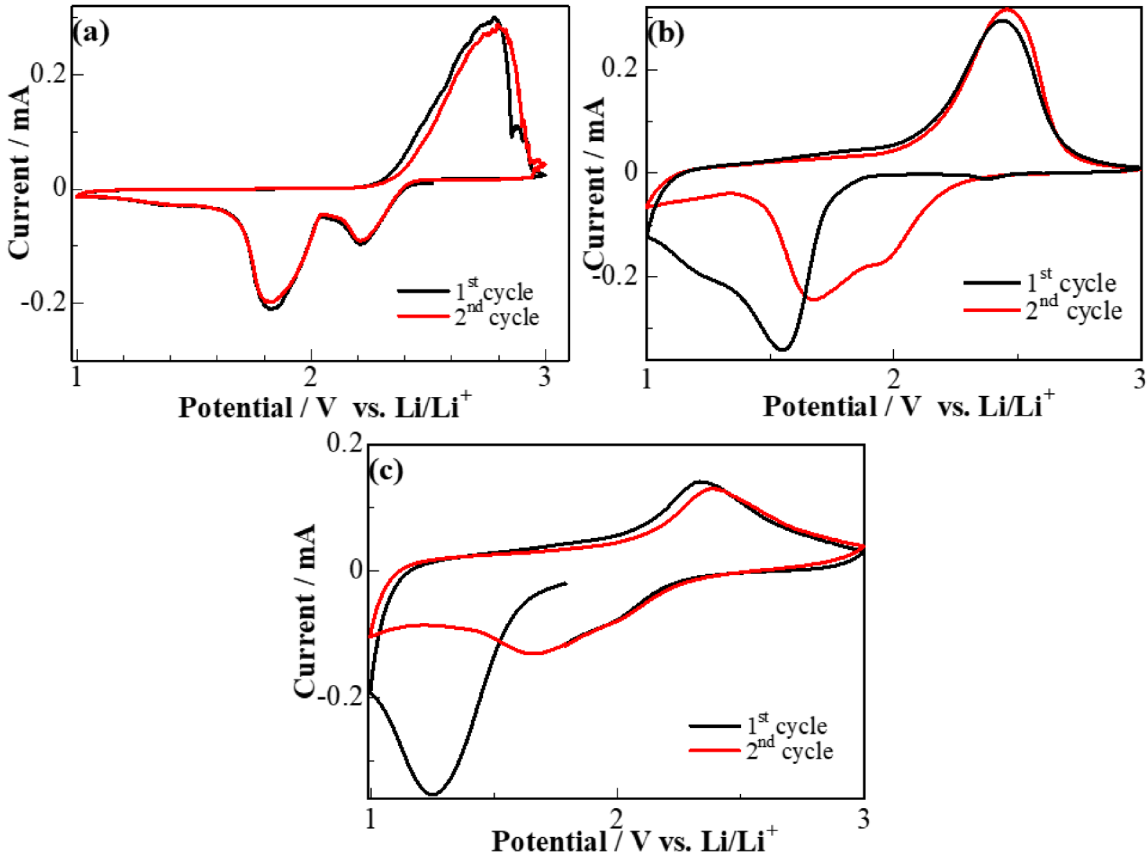

Figure 4.7. CV profiles of cells with (a) S/KB, (b) conventional S/DPAN/KB composite and (c) freestanding S/DPAN/KB nanofiber cathodes. Scan rate 0.1 mV s^{-1}.

There are two partially overlapping anodic peaks in case of the S/KB composite. The main one is centered at 2.9 V (vs. Li/Li^+), and the minor one is centered at a slightly lower potential of 2.7 V, which corresponds to the conversions of Li_2S/Li_2S_2 to the low-order polysulfides and the low-order polysulfides to high-order polysulfides, respectively. In the case of S/PAN cathode, CV curves are different from that of the S/KB composite. One can observe a broad reduction peak at around 1.6 V vs. Li/Li^+ in the first CV cycle of the conventionally prepared S/DPAN/KB composite, which shifts to the higher potentials upon the following cycle (Figure 4.7 b). The further cycling shows two overlapping and reversible reduction peaks at around 2.0 and 1.7 V and a broad oxidation peak at around 2.5 V. Also, there is the first small reduction peak at 2.0 V related to the formation of polysulfides and the second one at 1.7 V related to the further reduction of the polysulfides into lithium sulfide.

Figure 4.8 a shows the charge-discharge profiles of the S/DPAN/KB electrode at 0.1 C, which exhibits a large initial discharge capacity of 1759 mA h g^{-1}. The composite cathode delivers within the second cycle a high discharge capacity of 1128 mAh g^{-1} and a high coulombic efficiency up to ~99%, which corresponds to areal capacity of 1.70 mA h cm^{-2}, since the mass loading of S was around 1.5 mg cm^{-2}. Figure 4.8 b shows that the cell exhibits stable cycling performance at least for 150 cycles and maintaining a reversible capacity of 917 mAh g^{-1} after 150 cycles. The value of capacity fading per cycle is as small as 0.017%. Along with this, the S/DPAN/KB composite cathode exhibits a high coulombic efficiency about 100% over cycling, which could be due to the suppression of the polysulfides shuttle effect by the molecular level binding of sulfur with DPAN and also by porous structure of the fibers, which effectively store soluble products of the reduction of sulfur.

For comparison, the cyclability and rate performance of the S/KB and S/DPAN/KB electrodes prepared by slurry casting on Al foil with addition of conductive agent and binder were analyzed (Figure 4.9). Sulfur content in the composites was around 40 wt% and mass loading of sulfur was kept around 1.5 mg cm^{-2}. Freestanding S/DPAN/KB nanofiber composite cathode and the one prepared by slurry casting show very similar cyclability and gravimetric capacity based on mass of sulfur. However, freestanding S/DPAN/KB composite cathode has 340 mA h g^{-1} capacity calculated based on the composite electrode weight. It is higher for 20% then the capacity of S/DPAN/KB electrodes prepared by slurry casting on Al foil with addition of conductive agent and binder, which is 280 mA h g^{-1}, calculated for the electrode mass including the weight of current collector with the similar sulfur loading of 1.5

mg cm^{-2}. At the same time the cell with S/KB electrode perform poor cyclability and low coulombic efficiency (~80%) due to the dissolution of polysulfide and so called shuttle effect.

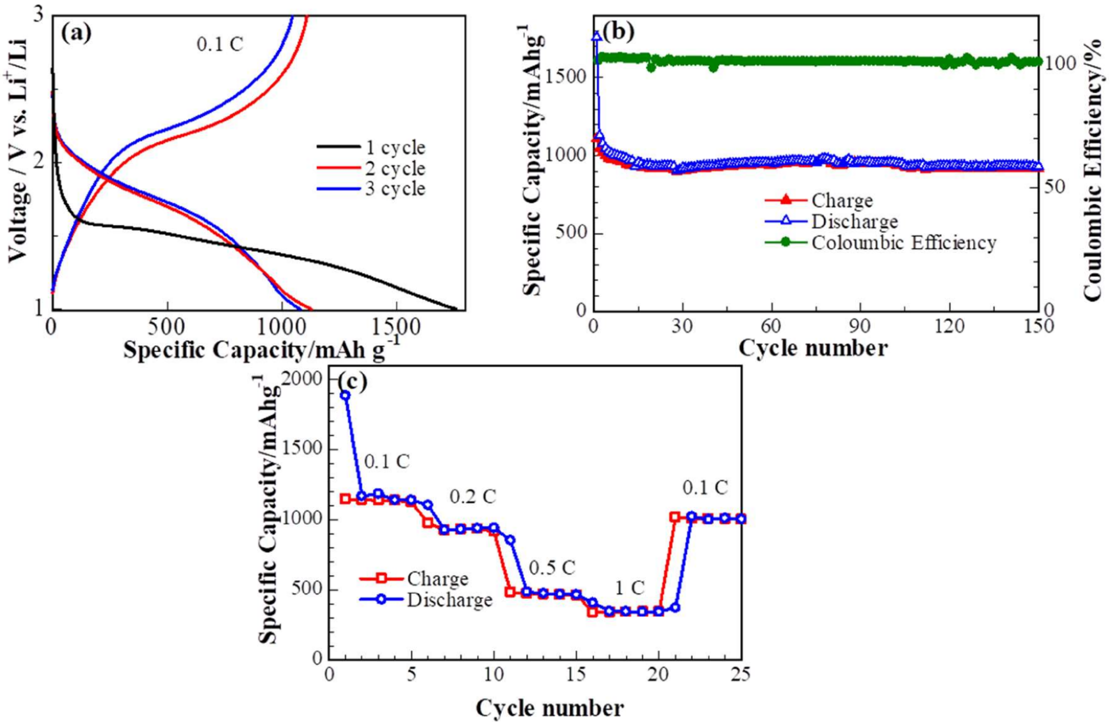

Figure 4.8. (a) Potential profiles, (b) cycle performance at 0.1 C, and (c) rate capability of cells with freestanding S/DPAN/KB composite cathode nanofibers.

In addition to a high capacity and good cyclability, the S/DPAN/KB nanofiber cathode without any current collector and conductive additives demonstrates a good rate capability as well. As shown in Figure 4.8 c, the nanofiber electrode delivers a discharge capacity of 1148 mA h g^{-1} at 0.1 C, 977 mA h g^{-1} at 0.2 C, 483 mA h g^{-1} at 0.5 C, and 342 mA h g^{-1} at 1 C. S/KB and S/DPAN/KB electrodes prepared by slurry casting on Al foil (Figure 4.9 c and d) exhibit slightly better C rate performance compared with freestanding electrode, delivering discharge capacity around 400 and 700 mA h g^{-1} at 1 C, correspondingly. The difference in capacity of cathodes with and without current collector increases with the higher current density, which is related to the rise of resistance in case of freestanding electrode. Nevertheless, the freestanding electrode can still deliver a considerably high reversible capacity of 342 mA h g^{-1} even at a current density of 1 C. Once the current density is reduced back to 0.1 C at the end of the rate capability tests, the discharge capacity of the electrode recovers to 1020 mA h g^{-1}, showing a good tolerance towards a high electric current impact.

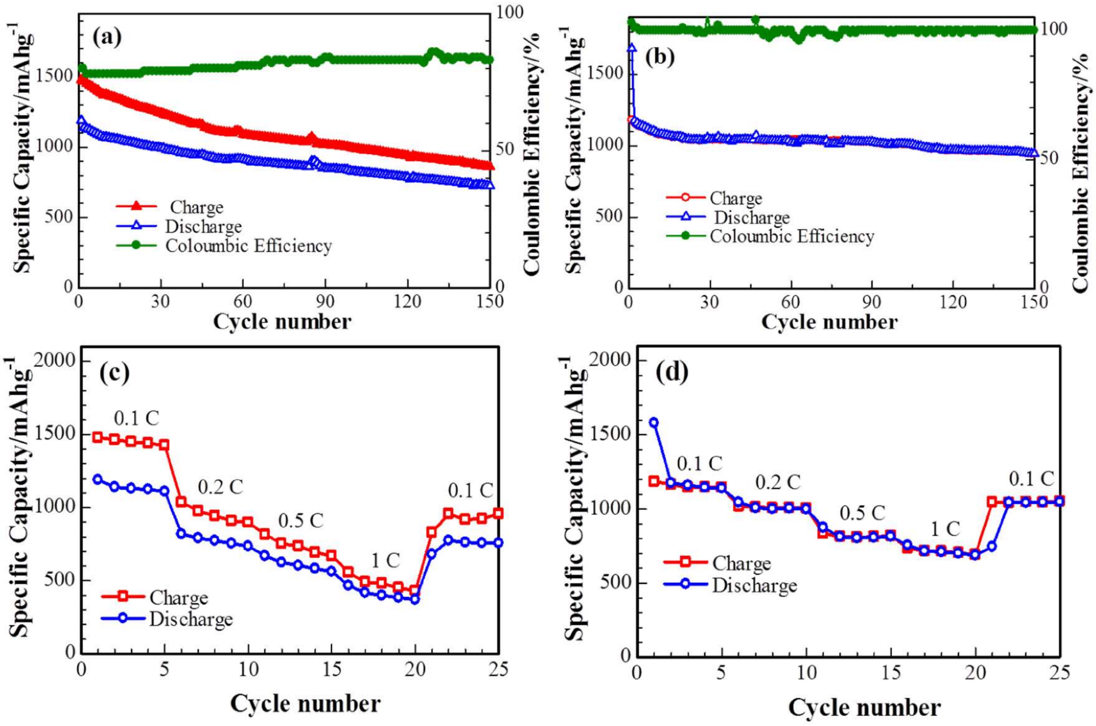

Figure 4.9. Electrochemical performance of cells with the cathodes prepared by conventional slurry casting on Al foil: cycling performance of (a) S/KB and (b) S/DPAN/KB composite cathodes at 0.1 C; and rate capability of (c) S/KB and (d) S/DPAN/KB composite cathode.

After cycling for 100 cycles at current of 150 mA g^{-1}, the cell was disassembled in the fully charged condition and the morphology of the post-cycled freestanding S/DPAN/KB nanofiber cathode was investigated. As shown in Figure 4.10, the shape, size and structural integrity of the original nanofiber electrode are well maintained, demonstrating good structural stability. S/DPAN/KB composite cathode retains the diameter of fibers with no significant change. The surface morphology becomes rougher compared to the fresh electrode, but there is no significant change in the BJH mean pore diameter and surface area of post-cycled nanofiber cathode as shown in Figure 4.11. The surface area of S/DPAN/KB after 100 cycles is around 91.28 m^2 g^{-1} and BJH mean pore diameter is 3.9365 nm.

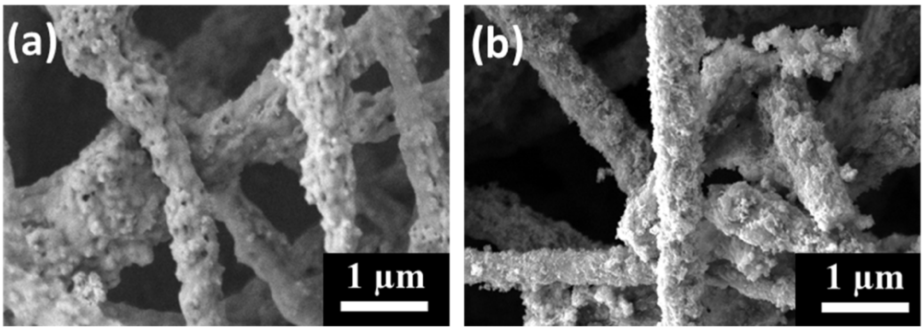

Figure 4.10. SEM images of S/DPAN/KB nanofiber electrode (a) before cycling and (b) after 100 charge-discharge cycles.

Since the S/DPAN/KB nanofiber composite is flexible, the pouch-type cell based on them can be flexible and bendable as well, as shown in Figure 4.12. Even after folding several times, the battery can still power LEDs without noticeable dimming.

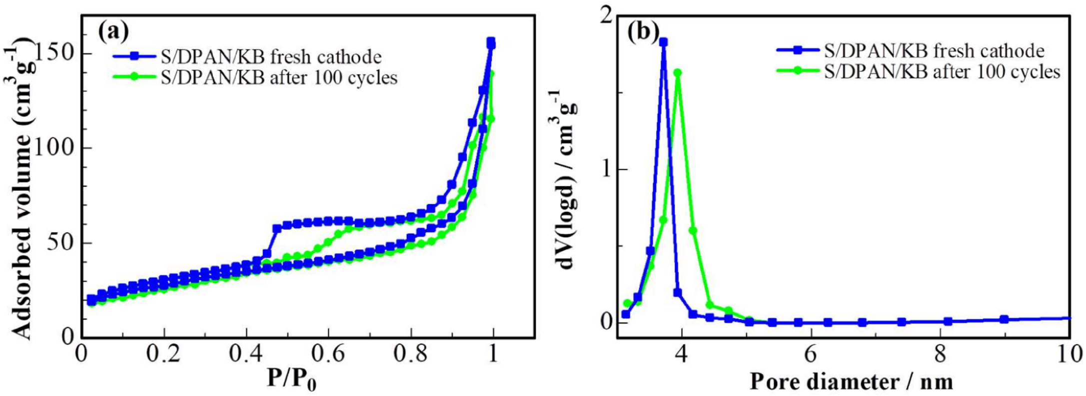

Figure 4.11. (a) N_2 sorption/desorption isotherms and (b) pore-size distributions curves of fresh and cycled (100 cycles) S/DPAN/KB cathode.

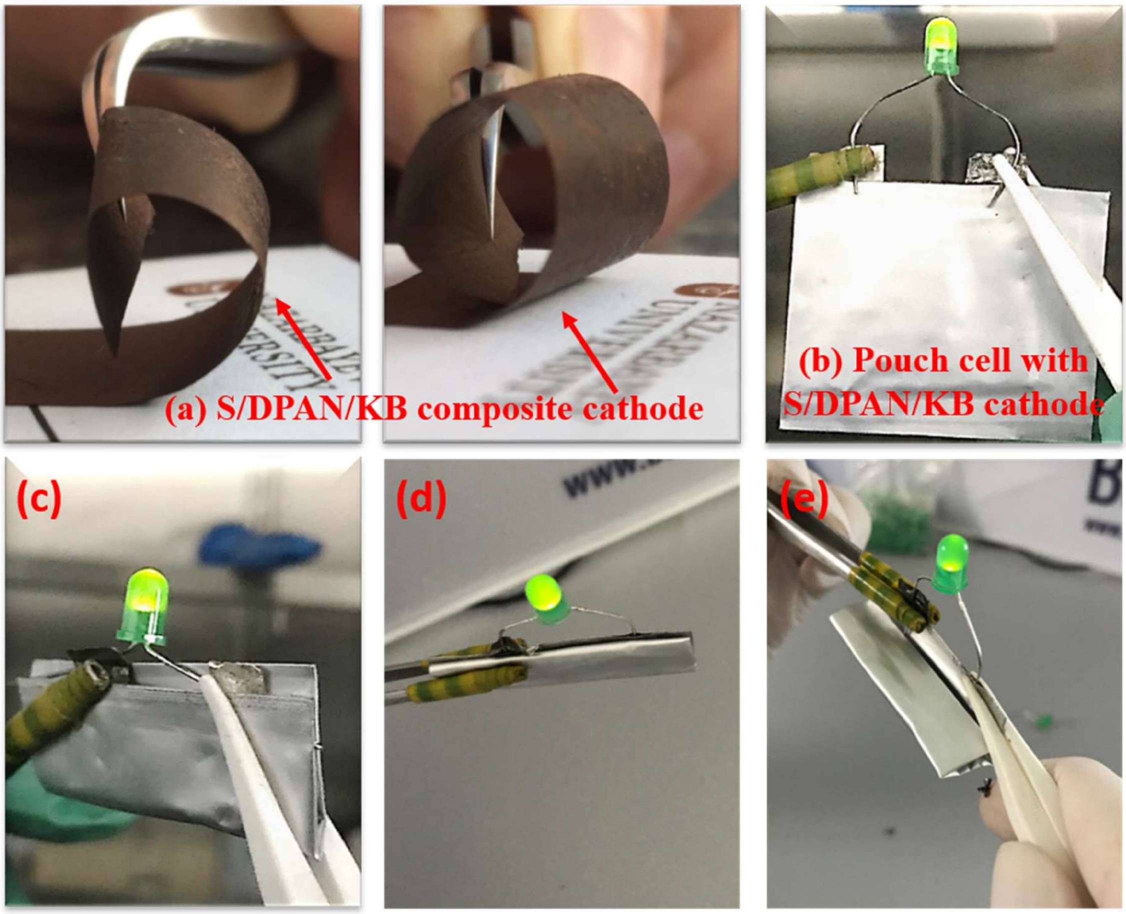

Figure 4.12. Photographs showing (a) the freestanding flexible S/DPAN/KB nanofiber composite cathode and (b) illustration of pouch cell with S/DPAN/KB nanofiber composite cathode powering LED lamps under normal static condition and (c, d, e) under being manually bent.

In summary, we have successfully prepared a sulfur-dehydrogenated PAN-ketjen black nanofiber freestanding composite cathode for flexible Li-S batteries by electrospinning technique. Optimal conditions of spinning process were established for preparation of S/PAN/KB nanofibers with a high sulfur content. Electrochemically active S/DPAN/KB cathode was prepared by heating at low temperature without carbonization of PAN to insure the flexibility and stability of this binder-free cathode. When used as cathode for Li-S batteries, S/DPAN/KB exhibits a good electrochemical performance in carbonate-based electrolyte. It exhibits stable cycling performance at least for 150 cycles and maintains a reversible capacity of 917 mAh g^{-1} after 150 cycles and a good rate capability with a reversible capacity of 342 mA h g^{-1} at 1 C. The value of capacity fading per cycle is as small as 0.017%. Within these properties, the highly flexible composite cathode can be produced in bigger sizes by electrospinning technique and used for LIB powering flexible electronic devices.

4.2. PAN Derived Electrospun Carbon Nanofibers as 3D Current Collector for Li/S Batteries

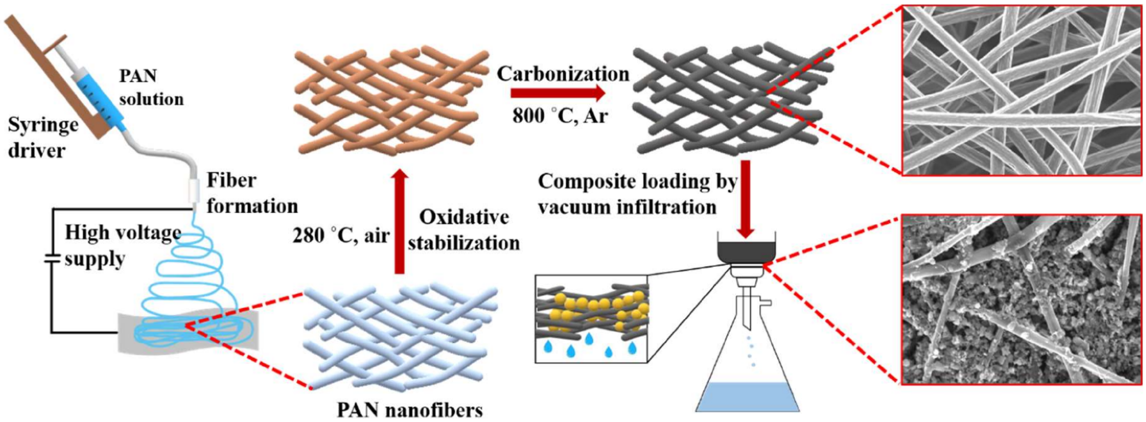

Figure 4.13. Scheme of carbon nanofiber fabrication and sulfur-based cathode preparation.

Schematic representation of the CNF preparation and loading with S/DPAN/CNT cathode is shown in Figure 4.13. As illustrated, after electrospinning of PAN solution with different concentrations, nanofibers were first stabilized in air. Upon the stabilization process, PAN interacts with oxygen and forms cyclized macromolecules, which keeps the fiber morphology unchanged during carbonization at high temperatures [101]. The carbonization of PAN NFs was carried out in the temperature range from 600 ºC to 800 ºC in an inert atmosphere. Afterward, structure and morphology of carbonized PAN (cPAN) NFs were characterized. The SEM images presented in Figure 4.14 show the morphology of the PAN and cPAN NFs derived from 10, 12 and 14 wt% PAN solutions and carbonized at 800 ºC. The SEM images of NFs stabilized, carbonized at 600 ºC and 700 ºC are shown in Figure 4.15. All PAN nanofibers had uniform structure without any beads and fiber diameters for PAN10, PAN12 and PAN14 were approximately ~500 nm, ~1200 nm, ~2400 nm, respectively. The morphologies of the cPAN NFs were similar to those of the precursor electrospun nanofibers (PAN) except for differences in diameters. The average diameter of the cPAN nanofibers was reduced almost by half of the precursor PAN nanofiber diameters, as summarized in Table 4.2.

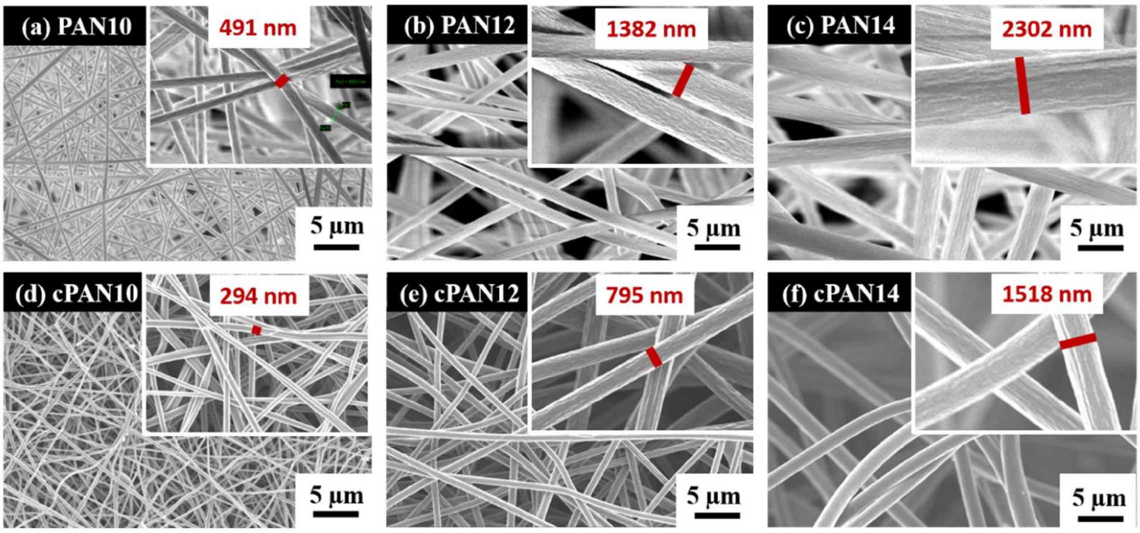

Figure 4.14. SEM images of (a) PAN10, (b) PAN12, (c) PAN14 and carbonized PAN nanofibers at 800 °C (d) cPAN10, (e) cPAN12, (f) cPAN14.

The change in diameter is due to the decomposition by evaluation of gases like H_2O, HCN, N_2 during carbonization process [102]. The void size between the fibers changes from 1 to 3 µm (**Table 4.2**) pursuant to SEM images. Considering the fiber diameter of ~800 nm and void size up to 1.5 µm, cPAN12 could be effectively used as current collector for sulfur composite cathode. The diameter and void size of cPAN10 are too small compared to S/DPAN/CNT composite material, which has a particle size in a range of 0.3-1.5 µm. On the contrary, cPAN14 fibers diameter is around 1.5 µm, and void size is around 3 µm, which complicates holding active material densely packed in its structure and decreases electrical conductivity as well.

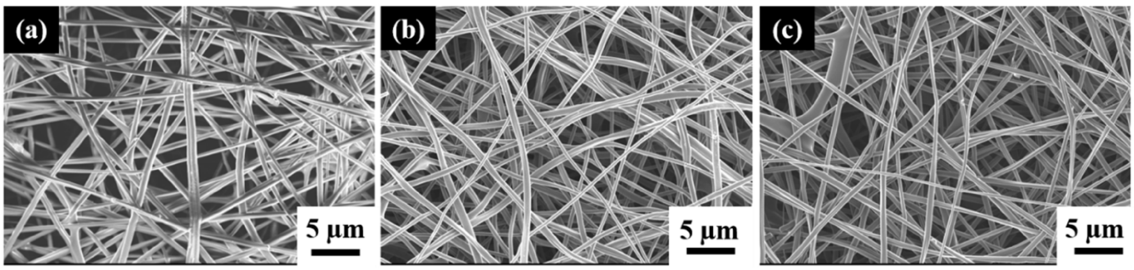

Figure 4.15. SEM images of (a) stabilized at 280 °C, carbonized at (b) 600 °C and (c) 700 °C PAN12 nanofibers.

Table 4.2. Diameter and void size of prepared nanofibers.

<table>
<tr><th>Name</th><th>Diameter of fiber, nm</th><th>Void distance, µm</th><th>Areal density, mg cm^{-2}</th><th>Thickness, µm</th></tr>
<tr><td>PAN10</td><td>~500</td><td>-</td><td rowspan="6">0.85</td><td rowspan="7">~25</td></tr>
<tr><td>PAN12</td><td>~1300</td><td>-</td></tr>
<tr><td>PAN14</td><td>~2500</td><td>-</td></tr>
<tr><td>cPAN10</td><td>~300</td><td>≤ 1</td></tr>
<tr><td>cPAN12</td><td>~800</td><td>≤ 1.5</td></tr>
<tr><td>cPAN14</td><td>~1500</td><td>≤ 3</td></tr>
<tr><td>Commercial carbon fibers</td><td>~7000</td><td>≤ 20</td><td>6.03</td></tr>
<tr><td colspan="5">S/DPAN/CNT particle size ≤ 1.5 µm</td></tr>
<tr><td colspan="3">Al current collector</td><td>4.9</td><td>~15</td></tr>
</table>

Figure 4.16 a shows the XRD patterns of precursor PAN, stabilized and carbonized PAN12 at different temperature ranges. The electrospun PAN nanofiber showed a characteristic strong diffraction peak centered at 2θ~17° and broad an amorphous scattering peak near 2θ ~27 [32] . However, these two peaks have disappeared in the case of stabilized fibers, which indicates the complete destruction of the pure PAN structure and change into aromatic ring/ladder structures during the stabilization [104]. This indicates that stabilization of PAN NFs was sufficiently accomplished within 1 h of heating [105]. It should be noted that the stabilization of conventional PAN takes more than 1 hour because of the heat diffusion rate in micro-sized fibers, therefore the process would be slower than for nano-sized PAN [106]. Further, the effect of temperature was investigated analyzing XRD patterns of carbonized PAN NFs at different temperatures. The cPAN NFs at 600 °C showed a broad amorphous peak centered near the 2θ ~25°. This peak might be related to the (002) c-axis disordered graphite-like material due to the stacking structure of aromatic layer (graphitic layer) [107]. With the increase of carbonization temperature, the intensity and sharpness of this peak gradually raised, suggesting a growing-up of aromatic layers and increase of ordering between graphitic layers [108]. It is known that the degree of graphitization rises with the

temperature [109,110], which is also confirmed by the sharp peak appeared 2θ ~26.8° attributed to the (002) reflection of hexagonal graphite at carbonization temperature 800 °C. It can also be observed by the results of Raman Spectroscopy which is another effective tool for micro structural analysis of carbon based materials [111]. The Raman spectra of cPAN CNFs with the final carbonization temperatures set at 600 °C, 700 °C, and 800 °C are presented in Figure 4.16 b, c, d.

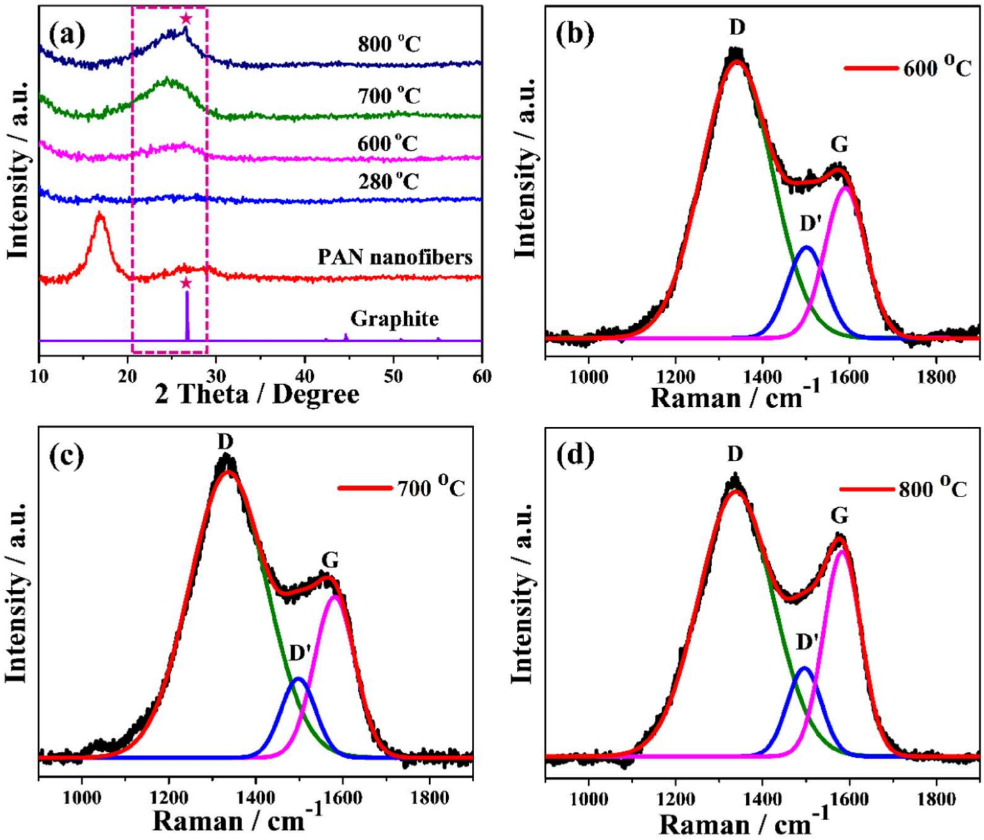

Figure 4.16. (a) XRD patterns and (b, c, d) Raman spectrum with the corresponding curve fitted bands of stabilized and carbonized PAN12 precursor nanofibers at different temperatures.

Carbonized NFs consist of three dominant peaks assigned as D, D' and G bands, as shown in curve-fitting of the peaks of Raman spectra. The D band around Raman shift 1340 cm^{-1} represents the disordered graphitic structure of the CNF and also signifies the sp^3 content present in cPAN NFs [112]. The small and broad D' peak at 1500 cm^{-1} also signifies the presence of defects, but it is due to amorphous sp^2 bonded carbon [113]. The intensity of D peak is higher compared to D' in all samples which shows the presence of more defects due to the amorphous sp^3 than amorphous sp^2. The G band around 1590 cm^{-1} indicates the ordered graphitic structure of the samples, and a broad shape of the peak indicates the small size of the CNFs crystallites [114]. However, it is noteworthy that with an increase in heating temperature intensity of G band in comparison/correspondence to D band increases significantly, which shows improvement in ordering graphitic layers of CNFs. The ordered structure of carbonaceous materials greatly affects the electrical conductivity, therefore cPAN12 carbonized at 800 °C are appropriate CNFs for application as current collector according to fiber diameter/void size as well, as mentioned above. Samples were not treated at temperatures above 800 °C since they become brittle and fragile.

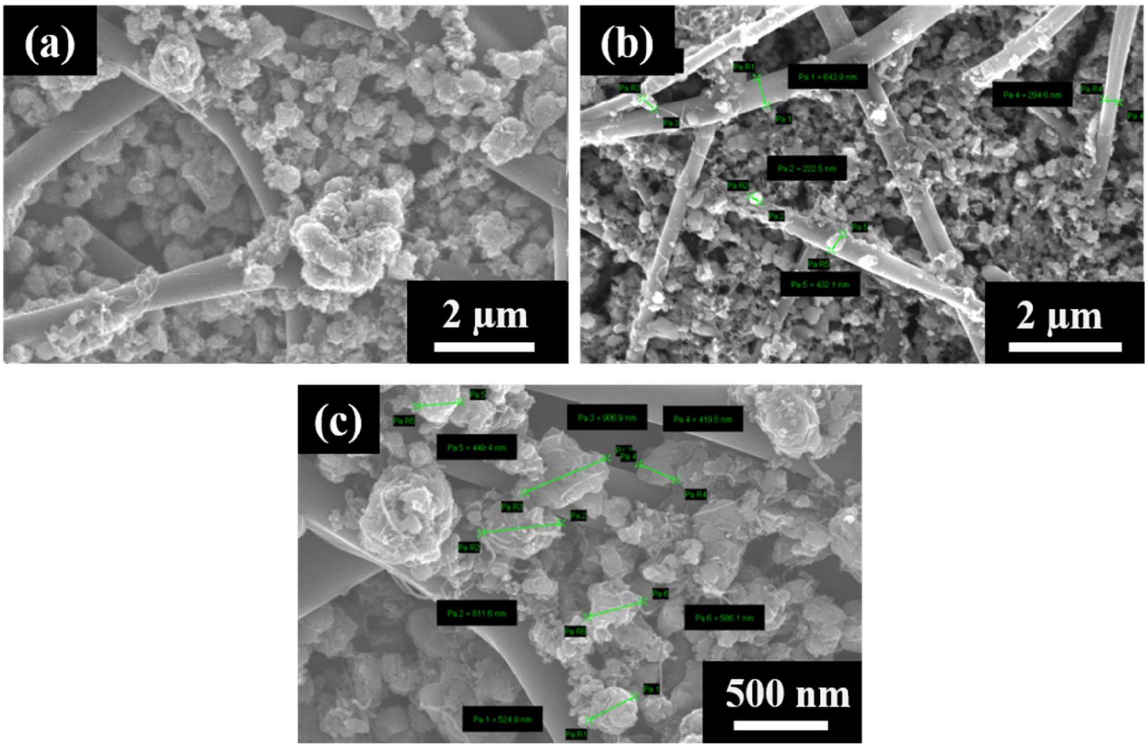

Figure 4.17. SEM images of (a) S/DPAN/CNT composite cathode on cPAN CNF current collector and (b, c) the cross-section view.

The S/DPAN/CNT composite slurry was prepared as electrode material and applied into cPAN12 NFs current collector. The slurry easily has penetrated into cPAN12 NFs by vacuum infiltration. The SEM images in Figure 4.17 displays the uniform distribution of the composite cathode within the nanofibers. From the cross-section images in Figure 4.17 b and c, it can be seen that S/DPAN/CNT composite penetrated deeply into the free spaces in internal CNF voids. The composite with the particle sizes less than 1.5 µm can easily penetrate into the current collector pores and be hold well in its structure.

The electrochemical performance of the S/DPAN/CNT cathode on 3D cPAN NF current collector was tested in lithium half-cells by CV, galvanostatic discharge/charge. Figure 4.18 a shows the CV curve of S/DPAN/CNT cathode during lithiation/delithiation process cycled in a potential range of 1.00–3.00 V at a scan rate of 0.1 mV s^{-1} vs. Li^+/Li. It's well known that CV curves of S/DPAN system are different from that of the S/C composite electrodes due to interaction of sulfur with PAN [115]. A broad reduction peak is observed at around 1.2 V vs. Li^+/Li in the first CV cycle of the S/DPAN/CNT composite, which shifts to the higher potentials upon the following cycles (Figure 4.18 a). The further cycling shows two overlapping and reversible reduction peaks at around 1.9 and 1.6 V and a broad oxidation peak at around 2.4 V. The first small reduction peak at 1.9 V related to the formation of high order polysulfides and the second one at 1.6 V related to the further reduction of the polysulfides into lithium sulfide.

Figure 4.18 b shows the discharge/charge profiles of the S/DPAN/CNT electrodes on cPAN CNF current collector with 1.2 mg cm^{-2} sulfur loading at a current rate of 0.1 C. The S/DPAN/CNT electrode shows a large initial discharge capacity of 2000 mAh g^{-1} which is typical for S/DPAN systems. The composite cathode delivers a high discharge capacity of 1620 mA h g^{-1} within the second cycle and gradually reduces to 1208 mA h g^{-1} in the first 50 cycles (Figure 4.18 c). A stable capacity of about 1100 mAh g^{-1} is received at 100^{th} cycle. The same composite electrode on Al foil with the similar mass loading offers only 1350 mAh g^{-1} and 870 mAh g^{-1} capacity at second and 100^{th} cycles (Figure 4.21**Ошибка! Источник ссылки не найден.** a, b).

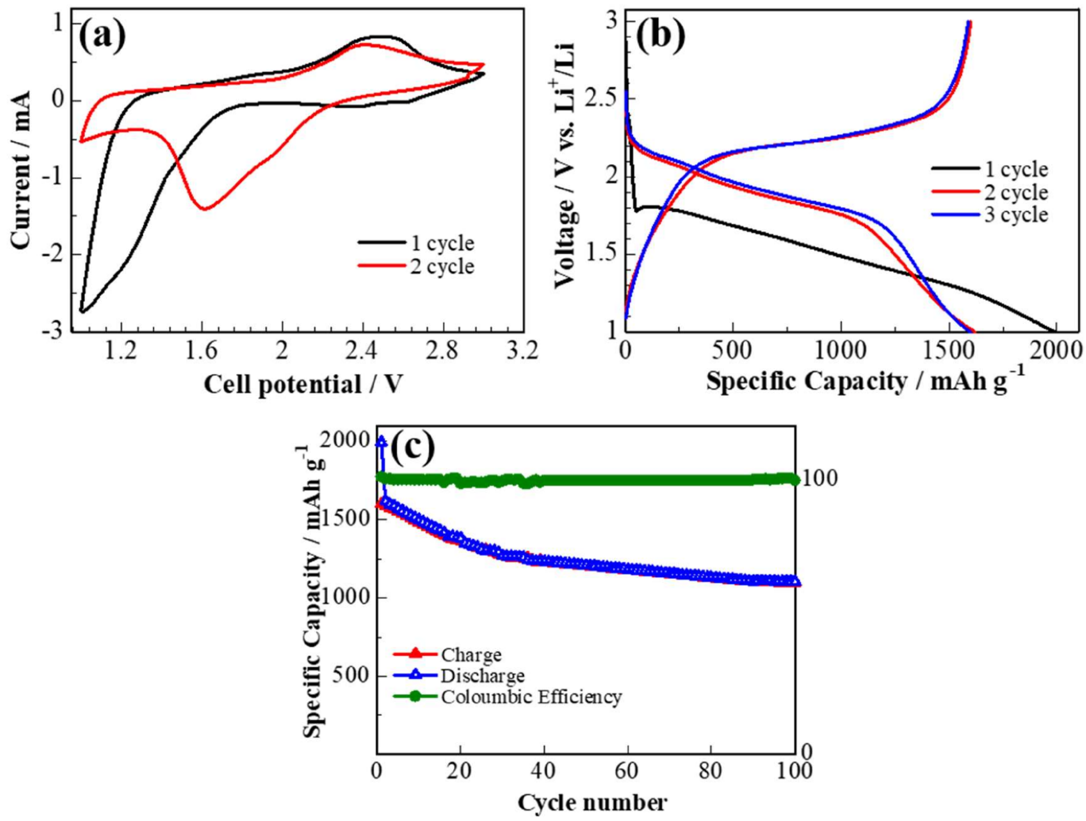

Figure 4.18. (a) CV profile, (b) potential profile and (c) cycle performance of sulfur composite on cPAN CNFs at 0.1 C.

Taking in account that the areal density of whole electrode including cPAN current collector is 4.06 mg cm^{-2} which is lighter than electrode on Al foil with the areal density of 8.10 mg cm^{-2} the capacity was calculated for the unit mass of electrode as 200 and 500 mAh g^{-1}, respectively. So the capacity of the electrode was increase 2.5 times by replacing Al foil with ultralight and porous cPAN CNF current collector. Along with this, the S/DPAN/CNT composite cathode exhibits a high coulombic efficiency about 100% over cycling, which could be due to the suppression of the polysulfides shuttle effect by the molecular level binding of sulfur with DPAN and 3D structure of the fibers, which effectively store soluble products of the reduction of sulfur [90].

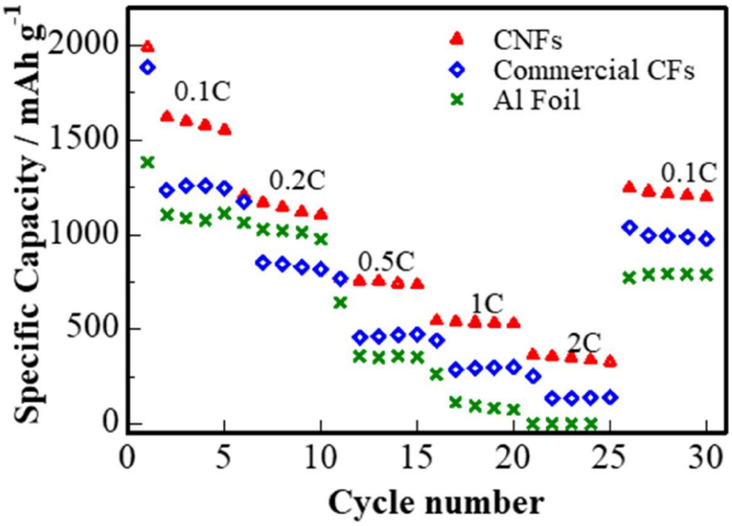

Figure 4.19. Rate capability of cells with sulfur composite cathode on cPAN CNF, commercial CNF current collector and Al foil (discharge capacity).

The rate capabilities of the S/DPAN/CNT electrodes on cPAN CNFs, commercial CF and Al foil with sulfur loading of ~1.2 mg cm^{-2} at different current rates (0.1 C - 2 C) are shown in Figure 4.19. The reversible discharge capacities are 1207, 770, 544, 360 mA h g^{-1} at constant current rates of 0.2 C, 0.5 C, 1 and 2 C, respectively. While the current density is reduced back to 0.1 C, the discharge capacity of the electrode recovers to 1250 mA h g^{-1}, showing a good tolerance toward a high electric current impact. S/DPAN/CNT composite cathode on cPAN CNF overperforms the electrode on commercial CF and Al foil with the same loading of 1.2 mg cm^{-2}. S/DPAN/CNT on commercial CF offers only 1260 mA h g^{-1} at 0.1 C and drops to 141 mA h g^{-1} at 2 C, while the cathode on Al foil fails at current density higher than 0.5 C.

As it is seen from SEM images, the diameter and void distance between fibers of commercial CF are larger for one order and incapable to hold the composite electrode particles (Figure 4.20) which results in lower electrical conductivity.

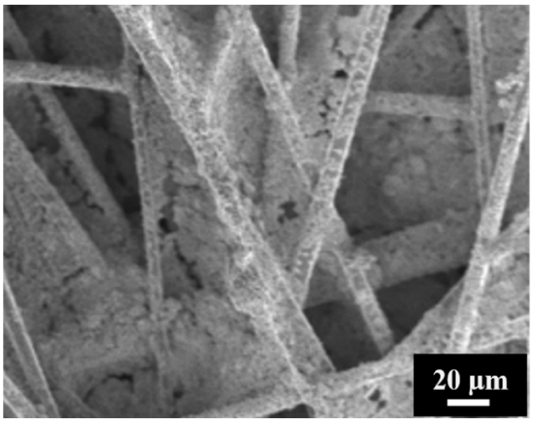

Figure 4.20. SEM image of sulfur based composite cathode on commercial CF current collector.

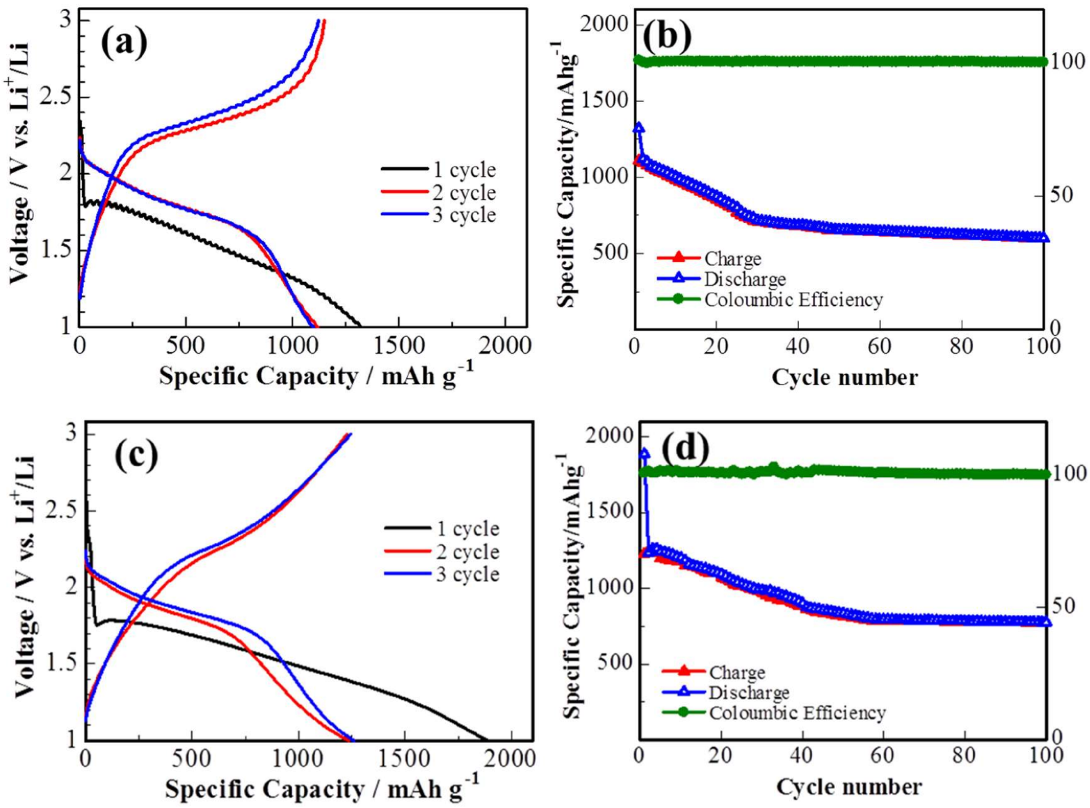

Figure 4.21. (a, b) Potential profile and cycle performance of sulfur composite on Al foil and (c, d) on commercial CFs at 0.1 C, respectively.

The better C rate performance of the cathode on cPAN can be explained by improved bulk conductivity owing to its 3D nanoarchitecture. The relatively poor rate capability of the same electrode on commercial CF in comparison with cPAN CNF current collector is related to lower bulk conductivity and weak adhesion of S/DPAN/CNT particles on fibers.

The comparison of charge/discharge profiles in Figure 4.18 b, Figure 4.21 a and c shows that the lowest polarization was observed for the cathode on cPAN CNF and the highest for Al foil, which correlated with the trend of C rate performance.

In summary, carbon nanofibers were successfully prepared with the controllable diameters less than 2 μm by simple electrospinning method. Optimal conditions of carbonization were established for PAN nanofibers. The areal density of cPAN mat (obtained from 12 wt% PAN solution) was 0.85 mg cm^{-2} with the thickness of ~25 μm, while commercial Al current collector with the same thickness weights 7.33 mg cm^{-2}. Owing to its unique structure, cPAN NFs remarkably improved cycle performance and rate capability of the electrode compared to the one on Al foil. The ultralight and porous cPAN could accommodate a large amount S/DPAN/CNT composite cathode resulting in sulfur mass loading of around 1.2 mg cm^{-2} and the electrode delivered the initial specific capacity of 500 mAh g^{-1} based on the mass of whole electrode.

cPAN NFs are lightweight, chemically stable and have a nano sized voids and fibers, which ensure the compact packing of active material and provide high bulk conductivity of the electrode. Also, they might help to suppress the polysulfide dissolution by trapping them into their porous structure, thus the developed system may be promising candidate for high performance Li/S batteries.

4.3. Flexible Siloxane-based Solid Polymer Electrolyte

SPEs composed of a-PDMS, PEGDA, ETPTA and Li salt (LiTFSI) were prepared by UV photocrosslinking method and abbreviated as PPE. Electrochemical and mechanical properties of SPE films were investigated. Prior to obtaining cross-linked PPE films, AcO-(PDMS)$_n$-OAc was synthesized from HO-(PDMS)n-OH and confirmed by appeared FTIR peaks of acrylic C=C bonds (1633 cm^{-1}) and ester linkage bonds (1708 cm^{-1}). FTIR peaks of hydroxyl terminated and a-PDMS are given in Figure 4.22.

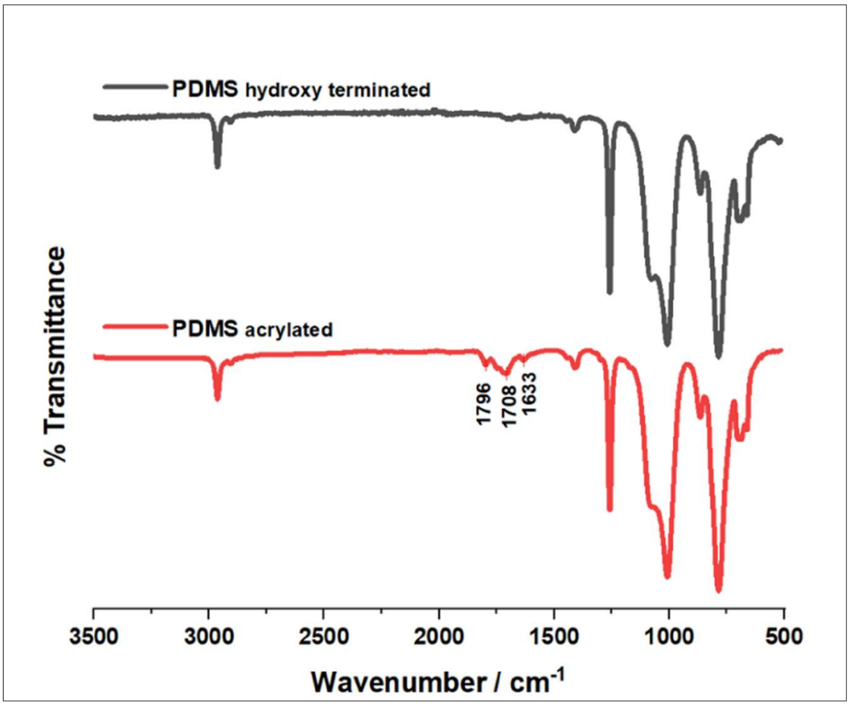

Figure 4.22. FTIR spectra of hydroxy terminated and acrylated PDMS.

Further, cross-linked flexible polymer electrolytes were obtained by UV-irradiation of photosensitive a-PDMS, PEGDA, and ETPTA in different mass ratios. PEGDA is usually used in photo-curing to modify the polymerization process. It controls the cross-linking density of the final networks, thus tailoring the physical properties of the cured membranes. Here, PEGDA was chosen to make easier transport of Li^+ ions in the polymer network due to its pendant ethoxy groups in the structure. ETPTA also has ethoxy groups which is important for ion conduction, as it was explained above [116]. The sketched representation of cross-linked SPE film is given Figure 4.23.

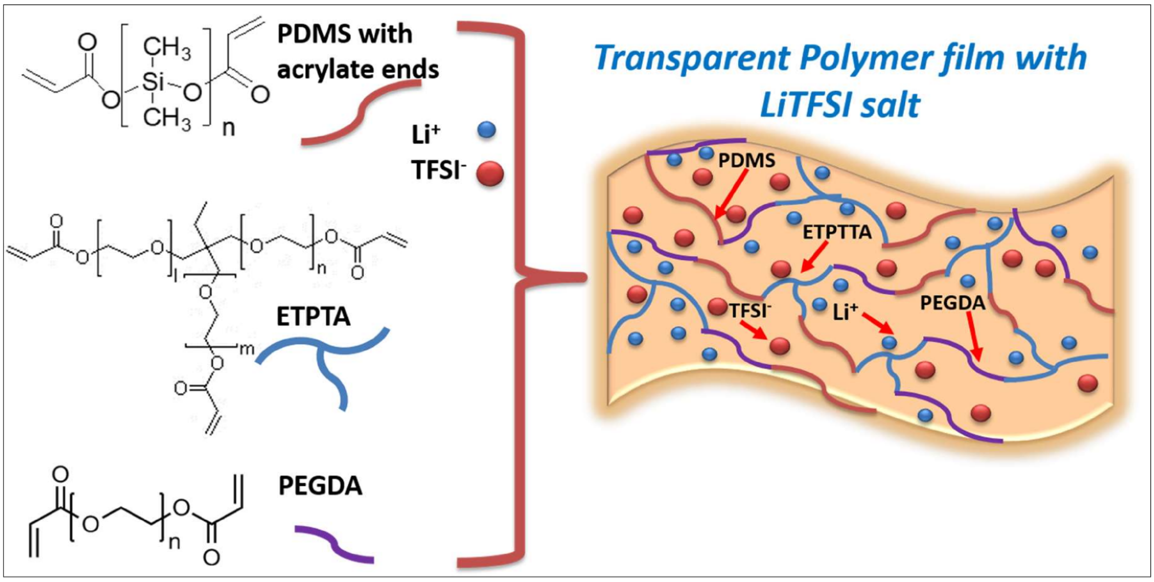

Figure 4.23. Sketched representation of cross-linked polymer film structure as a flexible solid-state electrolyte.

Table 4.3. UV-photocrosslinked SPEs with different compositions.

Sample	**Composition (wt%)**				
	a-PDMS	**PEGDA**	**ETPTA**	**[EO]/[Li$^+$]**	**Thickness (μm)**
PPE10	10	70	20	30	
PPE10	10	70	20	18	
PPE10	10	70	20	6	
PPE15	15	65	20	6	90 ±10
PPE5	5	75	20	6	
PPE0	0	80	20	6	

First, cross-linked PPE10 polymer films with [EO]/[Li$^+$] ratios 6, 18, 30 were prepared and characterized to investigate optimal salt ratio in SPE. Further, PPE with 5. 10, 15 wt% and without AcO-(PDMS)$_n$-OAc were prepared to examine a-PDMS effect on SPE properties. The SPE formulations are given in Table 4.3. Polymer membranes were easily detached from the glass plate.

UV-crosslinking reaction of the PPE SPEs analyzed by the FTIR peaks of acrylic C=C bonds (1610–1625 cm^{-1}) of the ETPTA monomer, AcO-$(PDMS)_n$-OAc and PEGDA before and after UV-irradiation. Figure 4.24 shows that after UV photocrosslinking, peaks of acrylic bonds disappeared and cross-linked PPE films were successfully formed.

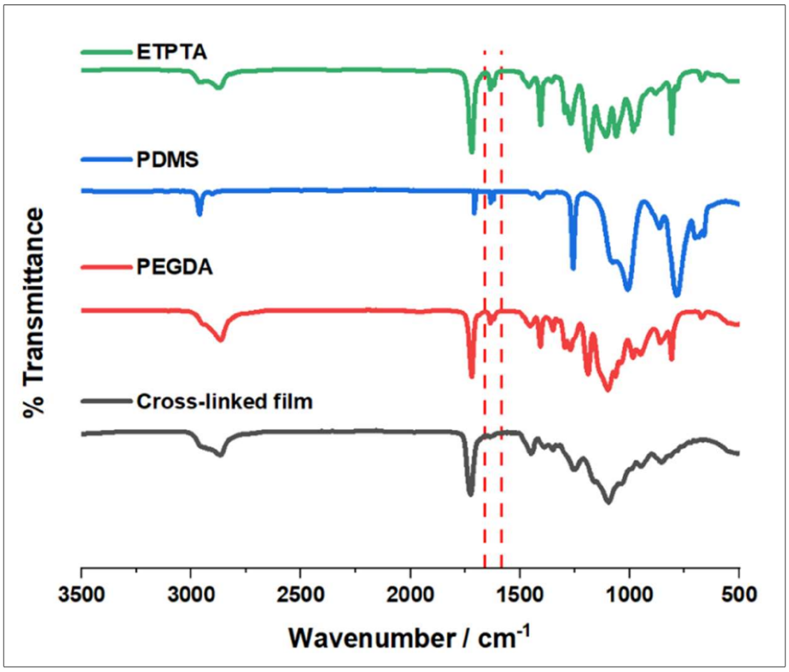

Figure 4.24. FTIR spectra of prepared cross-linked PPE film.

The PPE films also were characterized by measuring its gel content after solvent (acetone) extraction. It should be noted that for all prepared samples, gel content was found over 99%, which indicates/verifies that all obtained films were fully cross-linked.

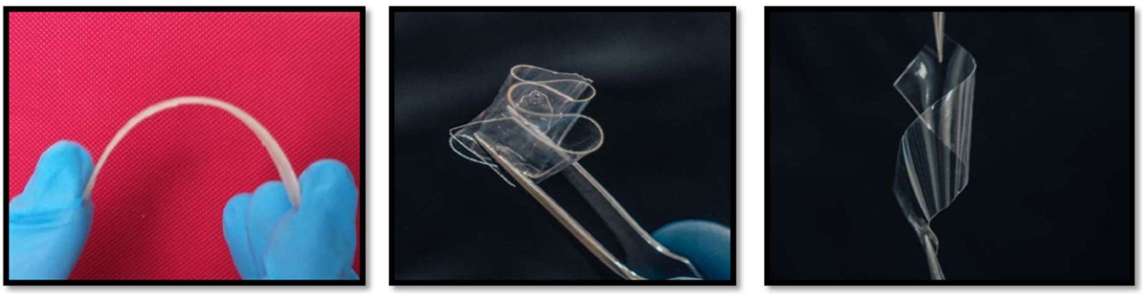

Figure 4.25. A representative photograph of a free-standing, flexible PPE10 SPE with $[EO]/[Li^+] = 6$.

All thin polymer films are transparent and freestanding. Figure 4.25 shows the photograph of a free-standing PPE10 membrane with [EO]/[Li^+] = 6 as a representative for all prepared PPE films. All PDMS-based SPEs are flexible and mechanical bendable, which is also shown in Figure 4.25. The surfaces of SPEs are smooth and homogenous as seen from SEM images in Figure 4.26 (a, b, c). From the both surface and cross-section view of films (Figure 4.26 d, e), it can be seen that Li salt was dissolved well in the polymer mixture during the preparation and didn't precipitate after film formation. In addition, in Figure 4.27, the SEM-EDS analysis shows a homogenous distribution of S, F from LiTFSI, and Si from a-PDMS within the cross-linked film. Thickness of all cross-linked films were in a range of 80-100 μm.

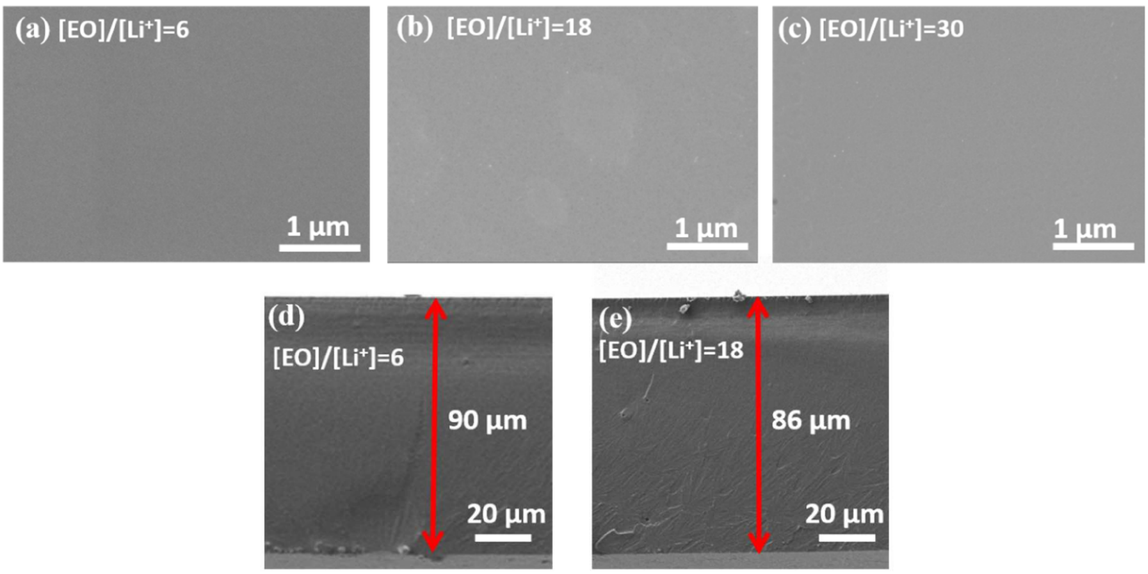

Figure 4.26. (a, b, c) the SEM images and (d, e) cross-section images of PPE10 SPEs with different Li salt loadings.

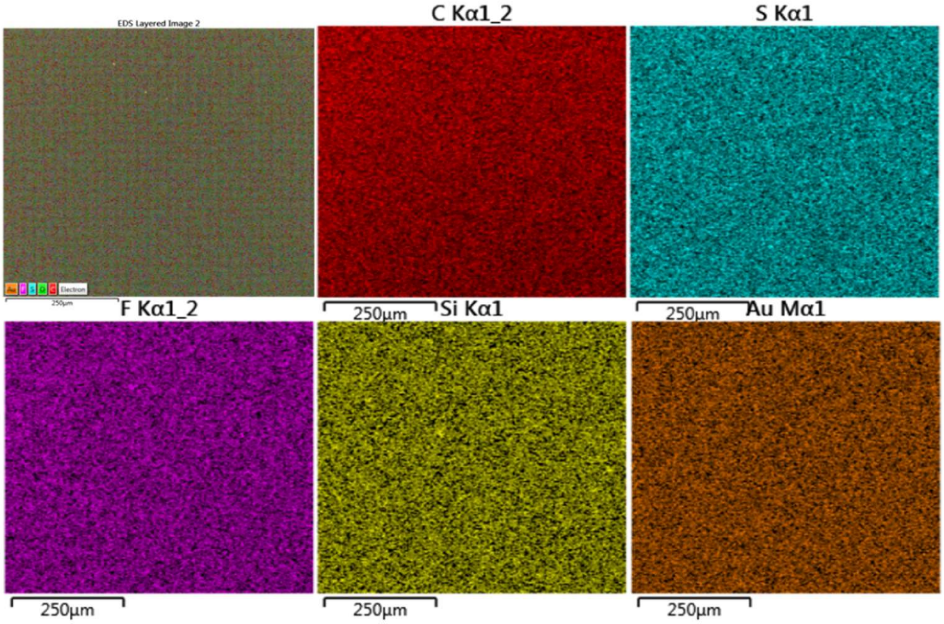

Figure 4.27. SEM/EDS images of PPE10 SPE with [EO]/[Li^+] = 6.

Thermal behavior of the samples was studied by the thermal gravimetric analysis (TGA) with the temperature range from 20 °C to 800 °C under nitrogen atmosphere and a heating rate of 10 °C min^{-1}. The slight weight loss in all samples of about 3–4% below 150 °C is due to the moisture absorbed during the preparation of samples (Figure 4.28). The main degradation of all samples starts from 300 to 450 °C, which corresponds to the decomposition of polymers and LiTFSI. Addition of higher amounts of LiTFSI doesn't affect the thermal stability of the polymer film significantly, which can be observed from the thermograms. Also with the increase of a-PDMS content in the polymer network, the thermal stability reduces insignificantly. The both TGA curves of SPEs with different Li salt and a-PDMS loadings are very similar to each other. The T_{10} (the temperature of 10 wt.% weight loss) and T_{50} (50% weight loss) values are very similar for all cross-linked PPE samples. In particular, very high value of T_{10} was observed about 320 °C, and T_{50} of about 380 °C. These results indicate that the PPE membranes can be safely applied as a SPE at high temperature ranges.

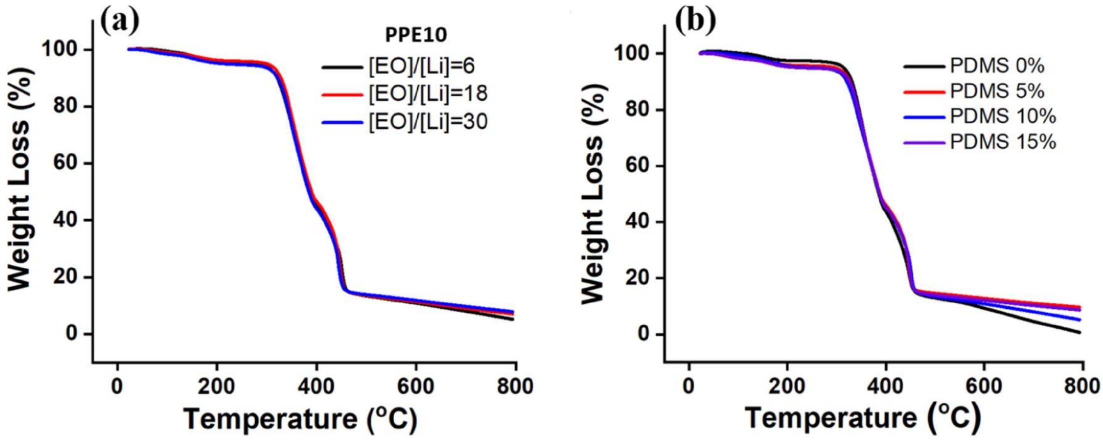

Figure 4.28. Thermo-gravimetric analysis of SPEs with various amount of (a) Li salt and (b) acrylated PDMS ($[EO]/[Li^+] = 6$).

The DSC studies were performed to investigate glass transition temperature (T_g) of PPE electrolyte membranes and results are shown in Table 4.4. According to results, T_g value of the most films were not observed which is normal for cross-linked polymers. Only PPE15 has showed T_g value of –52. All results indicate that a-PDMS loading disrupts the crystallinity of the polymers. In Appendix representative DSC thermograms are given.

Table 4.4. Mechanical properties and T_g values of SPE films.

	a-PDMS (wt%)	**$[EO]/[Li^+]$**	**T_g (°C)**	**Tensile Strength (MPa)**	**Elongation at break (%)**	**Young's Modulus (MPa)**
PPE0	0	6	no	1.68	12.99	14.03
PPE5	5	6	no	1.37	7.50	16.61
PPE10	10	6	no	0.91	6.6	16.03
PPE15	15	6	-52	0.70	5.96	14.22
PPE10	10	18	no	0.86	4.52	20.75
PPE10	10	30	no	1.95	5.37	34.75

The results of stress-strain tests are also given in Table 4.4. Young's modulus values of PPE0, PPE5, PPE10, PPE15 are very similar to each other. However, it slightly increases with the increase of Li salt, which is expected due to the incorporation of salt into the polymer chains. The mechanical strength is degreased with the increase of polymer chain flexibility. The mechanical strength of the electrolyte is expected to be sufficient to prevent short-circuit of lithium ion batteries, thus enabling the safety of LIBs.

Electrochemical measurements of the SPE

The temperature dependence of the ionic conductivity is measured by EIS and sandwiching PPE SPEs between two stainless steel (SS|PPE|SS). Conductivities of PPE polymer films with different amount of PDMS and [EO]/[Li^+] ratios of 6, 18, 30 were investigated. Figure 4.29 shows the conductivities of PPE films with various amount of a-PDMS ([EO]/[Li^+] = 6 is given as representative) and Li salt.

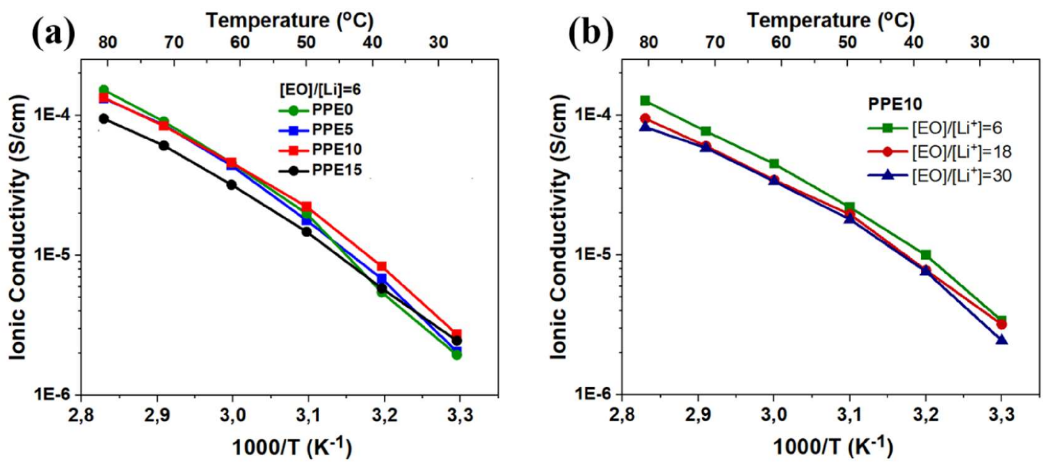

Figure 4.29. Ionic conductivity of the PPE SPEs with various amount of (a) PDMS and (b) Li salt as a function of temperature plots.

Ionic conductivity of the samples increases with an increase of a-PDMS concentration. Here, the important point is that at lower temperatures ionic conductivity of PPE membranes was improved significantly due to the presence of a-PDMS in the structure. a-PDMS increases amorphousness of the polymer film and enables Li^+ ion movement. At higher temperatures crystallinity of PEGDA and ETPTA degreases, thus the conductivity of SPEs increases, which is a typical phenomenon for polymers with –EO chains. An increase of PDMS concentration above 15 wt.% leads to the phase separation of polymer mixture. Thereby, PPE10 film conductivities with various [EO]/[Li^+] ratios are given in Figure 4.29 b. The ionic conductivity values of SPEs increase with an increase in the salt loading. The dissociation of LiTFSI occurs due to the strong interaction of lithium cations with the EO chains of both PEGDA and ETPTA. Ionic conductivity of SPE PPE10, [EO]/[Li^+] = 6 is better than other SPEs. It has ionic conductivity in the range of 1.5×10^{-6} S cm^{-1} at room temperature to 1.01×10^{-4} S cm^{-1} at 80 °C.

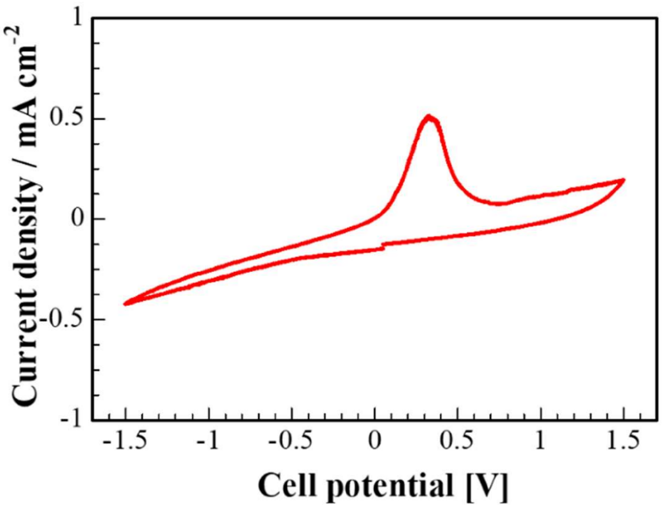

Figure 4.30. Cyclic voltammogram of the cell with SPE PPE10 ([EO]/[Li^+] = 6) at 60 °C at a rate of 1 mV s^{-1}.

Electrochemical stability window is an important parameter for application of SPEs in LIBs. For investigation of electrochemical stability CV and LSV measurements were conducted assembling stainless steel/PPE10/Li coin cells at 60 °C. Figure 4.30 shows the CV of the samples which were performed from -1.5 to 1.5 V at a scan rate of 0.1 mV s^{-1}. The lithium stripping/deposition peak was observed at a range of 0-0.5 V. It confirms the proper working of the SPE in lithium cell and presence of ion transporting interface. Oxidative degradation of the PPE SPE films started at approximately 4.8 V at 60 °C and was not observed at room temperature (Figure 4.31 a, b). This indicates that the cross-linked PDMS-based PPE SPEs have high electrochemical stability and can be applied for high-voltage lithium-ion batteries.

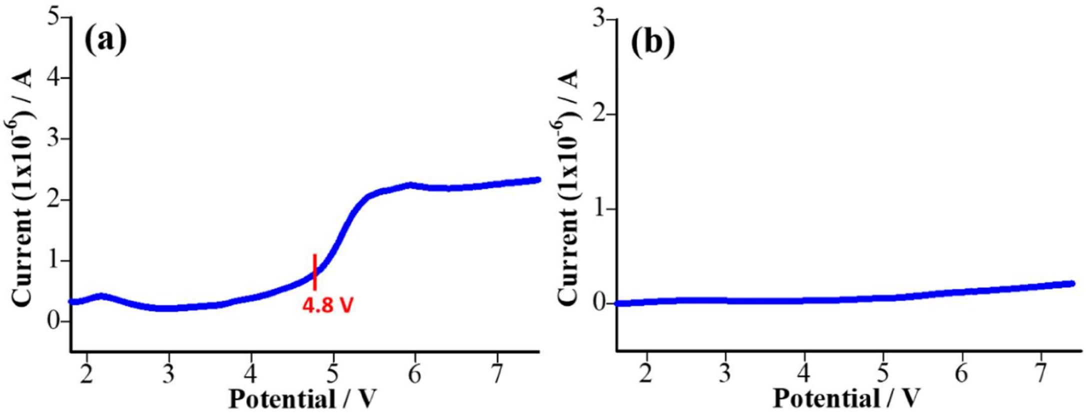

Figure 4.31. LSV of stainless steel/PPE10/Li coin cell at (a) 60 °C and (b) 25 °C at a rate of 0.1 mV s^{-1}.

In summary, series of flexible SPE films with a-PDMS were developed and studied. Among the prepared SPEs, PPE10 has good ionic conductivity in the range of 1.5×10^{-6} S cm^{-1} at room temperature and 1.01×10^{-4} S cm^{-1} at 80 °C. The mechanical strength of the electrolytes is good to apply in LIBs. The results of TGA analysis of PPE membranes indicate that membranes can be safely applied as a SPE at high temperature ranges. In addition, cross-linked PDMS-based PPE SPEs have high electrochemical stability and can be applied for high-voltage lithium-ion batteries.

5. SUMMARY AND FUTURE WORK

This doctoral thesis directed to the development of flexible components for solid-state Li/S batteries. The research mainly focuses on the synthesis of new materials, their characterization and application. In the scope of the research work, S/DPAN/KB flexible composite cathode, 3D carbonized PAN nanofiber current collector, and flexible PDMS-based SPE were prepared and examined as possible alternative components for high performance Li/S batteries. The main results are summarized below:

- Flexible S/DPAN/KB freestanding composite cathode have successfully prepared by electrospinning technique. When applied as cathode for Li/S batteries, S/DPAN/KB exhibits stable cycling performance at least for 150 cycles and maintains a reversible capacity of 917 mAh g^{-1} after 150 cycles and a good rate capability with a reversible capacity of 342 mA h g^{-1} at 1 C. The value of capacity fading per cycle is as small as 0.017%. S/DPAN/KB electrode can be used as ready cathode and doesn't need any binder and current collector. It has highly porous and interconnected fibrous nanostructure which makes easier to incorporate with SPEs by *in-situ* polymerization.
- Carbon nanofibers were successfully fabricated with the controllable diameters less than 2 μm by electrospinning method. Optimal conditions of carbonization were established for PAN nanofibers. The areal density of cPAN NFs (obtained from 12 wt% PAN solution) was 0.85 mg cm^{-2} with the thickness of ~25 μm, while commercial Al current collector with the same thickness weights 7.33 mg cm^{-2}. The capacity of the sulfur cathode was remarkably enhanced by replacing heavyweight metal current collector with 3D structured CNFs. The electrode capacity was improved from 200 to 500 mAh per the mass of the whole electrode including the current collector. The porous structure might help to suppress the polysulfide dissolution by trapping them into their pores, thus the developed system may be promising candidate for high performance Li/S batteries.
- SPEs were obtained by UV photocrosslinking of ethylene glycol unit containing oligomers and acrylated PDMS. Electrochemical and mechanical properties of films were investigated. The TGA results indicate that the PPE membranes can be safely

applied as a SPE at high temperature ranges. The ionic conductivity of PPE membranes was improved significantly due to the presence of PDMS in the structure. The lithium stripping/deposition peak was observed from CV and confirms the proper working of the SPE in lithium cell and presence of ion transporting interface. PDMS-based PPE SPEs have high electrochemical stability and can be applied for high-voltage lithium-ion batteries.

The main idea of this research work is assembling all-solid-state Li/S battery with flexible components. Now, the compatibility of prepared S/DPAN/KB flexible cathode and cross-linked PPE SPE is another important task for research. The future works are planning to be directed on assembling full all-solid-state Li/S cell using the aforementioned flexible S/DPAN/KB cathode and PPE SPEs. In order to achieve successful results, several research works are going to be continued:

- Ionic conductivity of PPE electrolytes at ambient temperature will be improved by further investigation and variation of polymer/salt ratios and 1 paper will be submitted SCI-indexed journal.
- The new methods of increasing S mass loading in nanofibrous S/DPAN/KB cathode as well as improvement of electrochemical performance will be investigated.
- *in-situ* fabrication and cell designing/assembling strategies will be developed to fabricate S/DPAN/KB-PPE systems for all-solid-state batteries. The compatibility and electrochemical performance of sulfur-based cathode with solid-state electrolyte will be investigated.
- Final step will be flexible all-solid-state pouch cell battery assembling with developed sulfur-based cathode and PDMS-based SPE.

REFERENCES

[1] Manthiram, A. (2017). An Outlook on Lithium Ion Battery Technology. ACS Central Science, 3(10), 1063–1069.

[2] Zheng, F., Kotobuki, M., Song, S., Lai, M.O., Lu, L. (2018). Review on solid electrolytes for all-solid-state lithium-ion batteries. Journal of Power Sources, 389, 198–213.

[3] Zhu, M., Wu, J., Wang, Y., Song, M., Long, L., Siyal, S.H., Yang, X., Sui, G. (2019). Recent advances in gel polymer electrolyte for high-performance lithium batteries. Journal of Energy Chemistry, 37, 126–142.

[4] B. Puthirath, A., Patra, S., Pal, S., M., M., Puthirath Balan, A., S., J., Tharangattu N., N. (2017). Transparent flexible lithium ion conducting solid polymer electrolyte. Journal of Materials Chemistry A, 5(22), 11152–11162.

[5] Warner, J. (2015). The Handbook of Lithium-Ion Battery Pack Design. Elsevier, MI, USA.

[6] Lundgren, C.A., Xu, K., Jow, T.R., Allen, J., Zhang, S.S. (2017). Lithium-Ion Batteries and Materials. in: Springer Handb. Electrochem. Energy, Springer Berlin Heidelberg, Berlin, Heidelbergpp. 449–494.

[7] Tarascon, J.M., Armand, M. (2001). Issues and challenges facing rechargeable lithium batteries. Nature, 414(6861), 359–67.

[8] Winter, M., Barnett, B., Xu, K. (2018). Before Li Ion Batteries. Chemical Reviews, 118(23), 11433–11456.

[9] Xu, Z.L., Kim, J.K., Kang, K. (2018). Carbon nanomaterials for advanced lithium sulfur batteries. Nano Today, 19, 84–107.

[10] Myung, S.T., Hitoshi, Y., Sun, Y.K. (2011). Electrochemical behavior and passivation of current collectors in lithium-ion batteries. Journal of Materials Chemistry, 21(27), 9891–9911.

[11] Gao, J., Shi, S.-Q., Li, H. (2016). Brief overview of electrochemical potential in lithium ion batteries. Chinese Physics B, 25(1), 018210.

[12] Yoshino, A., Sanechika, K., Nakajima, T. (1985). Japanese Patent 1989293, 1985.

[13] Nitta, N., Wu, F., Lee, J.T., Yushin, G. (2015). Li-ion battery materials: Present and future. Materials Today, 18(5), 252–264.

[14] Rogers, J.A., Maznev, A.A., Banet, M.J., Nelson, K.A. (2000). Optical Generation and Characterization of Acoustic Waves in Thin Films: Fundamentals and Applications. Annual Review of Materials Science, 30(1), 117–157.

[15] Goodenough, J.B., Park, K.S. (2013). The Li-ion rechargeable battery: A perspective. Journal of the American Chemical Society, 135(4), 1167–1176.

[16] Goriparti, S., Miele, E., Angelis, F. De, Di, E., Proietti, R., Capiglia, C. (2014). Review on recent progress of nanostructured anode materials for Li-ion batteries. Journal of Power Sources, 257, 421–443.

[17] Wang, L., Tang, C., Takeuchi, K.J., Takeuchi, E.S., Marschilok, A.C. (2018). Synthesis and Characterization of Li 4 Ti 5 O 12 Anode Materials with Enhanced High-Rate Performance in Lithium-Ion Batteries. MRS Advances, 3(11), 575–580.

[18] WHITTINGHAM, M.S. (1976). Electrical Energy Storage and Intercalation Chemistry. Science, 192(4244), 1126–1127.

[19] Fergus, J.W. (2010). Recent developments in cathode materials for lithium ion batteries. 195, 939–954.

[20] Islam, M.S., Fisher, C.A.J. (2014). Lithium and sodium battery cathode materials: computational insights into voltage, diffusion and nanostructural properties. Chemical Society Reviews, 43(1), 185–204.

[21] Kim, D.K., Muralidharan, P., Lee, H.-W., Ruffo, R., Yang, Y., Chan, C.K., Peng, H., Huggins, R.A., Cui, Y. (2008). Spinel LiMn 2 O 4 Nanorods as Lithium Ion Battery Cathodes. Nano Letters, 8(11), 3948–3952.

[22] Thackeray, M.M. (1997). Manganese oxides for lithium batteries. Progress in Solid

State Chemistry, 25(1–2), 1–71.

[23] Nanjundaswamy, K. (1996). Synthesis, redox potential evaluation and electrochemical characteristics of NASICON-related-3D framework compounds. Solid State Ionics, 92(1–2), 1–10.

[24] Fan, S.-H., Shao, G.-Q., Zhu, C., Ma, F.-F., Mao, J.-W., Zhang, A.-L., Xie, G.-Z., Yan, J.-L., Zhang, Y. (2018). Crystal structure and electrochemical properties of LiFe1-V PO4F1-O cathode materials for lithium-ion batteries. Electrochimica Acta, 280, 248–257.

[25] Yu, S.-H., Feng, X., Zhang, N., Seok, J., Abruña, H.D. (2018). Understanding Conversion-Type Electrodes for Lithium Rechargeable Batteries. Accounts of Chemical Research, 51(2), 273–281.

[26] Ji, X., Nazar, L.F. (2010). Advances in Li–S batteries. Journal of Materials Chemistry, 20(44), 9821.

[27] Wang, K., Luo, S., Wu, Y., He, X., Zhao, F., Wang, J., Jiang, K., Fan, S. (2013). Super-aligned carbon nanotube films as current collectors for lightweight and flexible lithium ion batteries. Advanced Functional Materials, 23(7), 846–853.

[28] Peng, H.J., Xu, W.T., Zhu, L., Wang, D.W., Huang, J.Q., Cheng, X.B., Yuan, Z., Wei, F., Zhang, Q. (2016). 3D Carbonaceous Current Collectors: The Origin of Enhanced Cycling Stability for High-Sulfur-Loading Lithium–Sulfur Batteries. Advanced Functional Materials, 26(35), 6351–6358.

[29] Johnson, B.A., White, R.E. (1998). Characterization of commercially available lithium-ion batteries. Journal of Power Sources, 70(1), 48–54.

[30] Arora, P. (1998). Capacity Fade Mechanisms and Side Reactions in Lithium-Ion Batteries. Journal of The Electrochemical Society, 145(10), 3647–3667.

[31] Zharbossyn, A., Mukanova, A., Nurpeissova, A., Urazbayev, A., Kim, S.-S., Bakenov, Z. (2017). Graphene Coated Ni Foam As a Current Collector for N-Type Doped Si Thin Film Anode for Li-Ion Batteries. in: MA2017-02, p. 186.

[32] Ryu, H.S., Ahn, H.J., Kim, K.W., Ahn, J.H., Lee, J.Y., Cairns, E.J. (2005). Self-discharge of lithium-sulfur cells using stainless-steel current-collectors. Journal of Power Sources, 140(2), 365–369.

[33] Chung, S.H., Manthiram, A. (2013). Nano-cellular carbon current collectors with stable cyclability for Li-S batteries. Journal of Materials Chemistry A, 1(34), 9590–9596.

[34] Zhang, B., Kang, F., Tarascon, J.M., Kim, J.K. (2016). Recent advances in electrospun carbon nanofibers and their application in electrochemical energy storage. Progress in Materials Science, 76, 319–380.

[35] Chung, S.H., Manthiram, A. (2014). Low-cost, porous carbon current collector with high sulfur loading for lithium-sulfur batteries. Electrochemistry Communications, 38, 91–95.

[36] Hu, L., Wu, H., Mantia, F. La, Yang, Y., Cui, Y. (2010). Thin, Flexible Secondary Li-Ion Paper Batteries. 4(10), 5843–5848.

[37] Leijonmarck, S., Cornell, A., Lindbergh, G., Wågberg, L. (2013). Flexible nano-paper-based positive electrodes for Li-ion batteries-Preparation process and properties. Nano Energy, 2(5), 794–800.

[38] Lu, H., Hagberg, J., Lindbergh, G., Cornell, A. (2017). Li4Ti5O12 flexible, lightweight electrodes based on cellulose nanofibrils as binder and carbon fibers as current collectors for Li-ion batteries. Nano Energy, 39(January), 140–150.

[39] Zhang, Y., Bakenov, Z., Zhao, Y., Konarov, A., Wang, Q., Chen, P. (2014). Three-dimensional carbon fiber as current collector for lithium/sulfur batteries. Ionics, 20(6), 803–808.

[40] Marcinek, M., Syzdek, J., Marczewski, M., Piszcz, M., Niedzicki, L., Kalita, M., et al. (2015). Electrolytes for Li-ion transport - Review. Solid State Ionics, 276, 107–126.

[41] Kuo, P.L., Wu, C.A., Lu, C.Y., Tsao, C.H., Hsu, C.H., Hou, S.S. (2014). High

Performance of Transferring Lithium Ion for Polyacrylonitrile-Interpenetrating Cross linked Polyoxyethylene Network as Gel Polymer Electrolyte. ACS Appl Mater Interfaces, 6(5), 3156–3162.

[42] Zhu, M., Wu, J., Wang, Y., Song, M., Long, L., Siyal, S.H., Yang, X., Sui, G. (2019). Recent advances in gel polymer electrolyte for high-performance lithium batteries. Journal of Energy Chemistry, 37, 126–142.

[43] Gwon, H., Hong, J., Kim, H., Seo, D.-H., Jeon, S., Kang, K. (2014). Recent progress on flexible lithium rechargeable batteries. Energy Environ. Sci., 7(2), 538–551.

[44] Choi, K.H., Cho, S.J., Kim, S.H., Kwon, Y.H., Kim, J.Y., Lee, S.Y. (2014). Thin, deformable, and safety-reinforced plastic crystal polymer electrolytes for high-performance flexible lithium-ion batteries. Advanced Functional Materials, 24(1), 44–52.

[45] Manthiram, A., Yu, X., Wang, S. (2017). Lithium battery chemistries enabled by solid-state electrolytes. Nature Reviews Materials, 2(4), 16103.

[46] Wu, Y., Gao, M., Li, X., Liu, Y., Pan, H. (2014). Preparation of mesohollow and microporous carbon nanofiber and its application in cathode material for lithium-sulfur batteries. Journal of Alloys and Compounds, 608, 220–228.

[47] Zhao, Y., Zhang, Y., Bakenova, Z., Bakenov, Z. (2015). Carbon/Sulfur Composite Cathodes for Flexible Lithium/Sulfur Batteries: Status and Prospects. Frontiers in Energy Research, 3, 2.

[48] Wang, H., Yang, Y., Liang, Y., Robinson, J.T., Li, Y., Jackson, A. (2011). Graphene-Wrapped Sulfur Particles as a Rechargeable Lithium À Sulfur Battery Cathode Material with High Capacity and Cycling Stability. Nano Lett., 11, 2644–2647.

[49] Zeng, L., Pan, F., Li, W., Jiang, Y., Zhong, X., Yu, Y. (2014). Free-standing porous carbon nanofibers-sulfur composite for flexible Li-S battery cathode. Nanoscale, 6(16), 9579–9587.

[50] Li, Q., Liu, M., Qin, X., Wu, J., Han, W., Liang, G., Zhou, D., He, Y.B., Li, B., Kang,

F. (2016). Cyclized-polyacrylonitrile modified carbon nanofiber interlayers enabling strong trapping of polysulfides in lithium-sulfur batteries. Journal of Materials Chemistry A, 4(33), 12973–12980.

[51] Zhang, Y., Zhao, Y., Bakenov, Z., Konarov, A., Chen, P. (2014). Preparation of novel network nanostructured sulfur composite cathode with enhanced stable cycle performance. Journal of Power Sources, 270, 326–331.

[52] Wu, F., Chen, J., Li, L., Zhao, T., Chen, R. (2011). Improvement of rate and cycle performence by rapid polyaniline coating of a MWCNT/sulfur cathode. Journal of Physical Chemistry C, 115(49), 24411–24417.

[53] Li, G.C., Li, G.R., Ye, S.H., Gao, X.P. (2012). A Polyaniline-coated sulfur/carbon composite with an enhanced high-rate capability as a cathode material for lithium/sulfur batteries. Advanced Energy Materials, 2(10), 1238–1245.

[54] Li, C., Zou, Y., Duan, J., Wang, Y., Qi, Z., Li, Z. (2018). Polythiophene lamella wrapped sulfur as cathode for rechargeable lithium sulfur batteries. Materials Letters, 218(May), 142–145.

[55] Wu, Y., Gao, M., Li, X., Liu, Y., Pan, H. (2014). Preparation of mesohollow and microporous carbon nanofiber and its application in cathode material for lithium-sulfur batteries. Journal of Alloys and Compounds, 608, 220–228.

[56] Li, J., Li, K., Li, M., Gosselink, D., Zhang, Y., Chen, P. (2014). A sulfur-polyacrylonitrile/graphene composite cathode for lithium batteries with excellent cyclability. Journal of Power Sources, 252, 107–112.

[57] Yin, Y.X., Xin, S., Guo, Y.G., Wan, L.J. (2013). Lithium-sulfur batteries: Electrochemistry, materials, and prospects. Angewandte Chemie - International Edition, 52(50), 13186–13200.

[58] Zhang, Y., Bakenov, Z., Zhao, Y., Konarov, A., Doan, T.N.L., Malik, M., Paron, T., Chen, P. (2012). One-step synthesis of branched sulfur/polypyrrole nanocomposite cathode for lithium rechargeable batteries. Journal of Power Sources, 208, 1–8.

[59] Wang, J., Yang, J., Wan, C., Du, K., Xie, J., Xu, N. (2003). Sulfur composite cathode materials for rechargeable lithium batteries. Advanced Functional Materials, 13(6), 487–492.

[60] Liu, Q., Zhu, J., Zhang, L., Qiu, Y. (2018). Recent advances in energy materials by electrospinning. Renewable and Sustainable Energy Reviews, 81(September), 1825–1858.

[61] Baştürk, E., Çakmakçi, E., Madakbaş, S., Kahraman, M.V. (2017). Surface and proton conductivity properties of electrospun poly(vinyl butyral)/polyaniline nanofibers. Advances in Polymer Technology, 37, 1774–1781.

[62] Huang, L., Cheng, J., Qu, G., Li, X., Hu, Y., Ni, W., Yuan, D., Zhang, Y., Wang, B. (2015). Porous carbon nanofibers formed in situ by electrospinning with a volatile solvent additive into an ice water bath for lithium-sulfur batteries. RSC Advances, 5(30), 23749–23757.

[63] Oktay, B., Baştürk, E., Kahraman, M.V., Apohan, N.K. (2018). Thiol-yne photo-clickable electrospun phase change materials for thermal energy storage. Reactive and Functional Polymers, 127, 10–19.

[64] Eminoğlu, E.M., Kahraman, M.V. (2013). Novel polythiophene based nanofibers obtained by simultaneous electrospinning and UV. Synthetic Metals, 183, 29–35.

[65] Dirlam, P.T., Glass, R.S., Char, K., Pyun, J. (2017). The use of polymers in Li-S batteries: A review. Journal of Polymer Science, Part A: Polymer Chemistry, 55(10), 1635–1668.

[66] Fu, G., Soucek, M.D., Kyu, T. (2018). Fully flexible lithium ion battery based on a flame retardant, solid-state polymer electrolyte membrane. Solid State Ionics, 320(March), 310–315.

[67] Aziz, S.B., Woo, T.J., Kadir, M.F.Z., Ahmed, H.M. (2018). A conceptual review on polymer electrolytes and ion transport models. Journal of Science: Advanced Materials and Devices, 3(1), 1–17.

[68] Macglashan, G.S., Andreev, Y.G., Bruce, P.G. (1999). Structure of the polymer electrolyte poly (ethylene oxide) 6 : LiAsF 6. 398(April), 5–7.

[69] Chen, R., Qu, W., Guo, X., Li, L., Wu, F. (2016). The pursuit of solid-state electrolytes for lithium batteries: from comprehensive insight to emerging horizons. Materials Horizons, 3(6), 487–516.

[70] Yue, L., Ma, J., Zhang, J., Zhao, J., Dong, S., Liu, Z., Cui, G., Chen, L. (2016). All solid-state polymer electrolytes for high-performance lithium ion batteries. Energy Storage Materials, 5, 139–164.

[71] Meyer, W.H. (1998). Polymer Electrolytes for Lithium-Ion Batteries. Advanced Materials, 10(6), 439–448.

[72] Fenton, D.E., Parker, J.M., Wright, P.V. (1973). Complexes of alkali metal ions with poly(ethylene oxide). Polymer, 14(11), 589.

[73] Armand, M. (1994). The history of polymer electrolytes. Solid State Ionics, 69(3–4), 309–319.

[74] Arya, A., Sharma, A.L. (2017). Polymer electrolytes for lithium ion batteries: a critical study. Ionics, 23(3), 497–540.

[75] Agrawal, R.C., Pandey, G.P. (2008). Solid polymer electrolytes: materials designing and all-solid-state battery applications: an overview. Journal of Physics D: Applied Physics, 41(22), 223001.

[76] Zhou, D., Shanmukaraj, D., Tkacheva, A., Armand, M., Wang, G. (2019). Polymer Electrolytes for Lithium-Based Batteries: Advances and Prospects. Chem, 5(9), 2326–2352.

[77] Rossi, N.A.A., Zhang, Z., Schneider, Y., Morcom, K., Lyons, L.J., Wang, Q., Amine, K., West, R. (2006). Synthesis and characterization of tetra- and trisiloxane-containing oligo(ethylene glycol)s- highly conducting electrolytes for lithium batteries. Chemistry of Materials, 18(5), 1289–1295.

[78] Grewal, M.S., Tanaka, M., Kawakami, H. (2019). Bifunctional poly(ethylene glycol)

based crosslinked network polymers as electrolytes for all-solid-state lithium ion batteries. Polymer International, 68(4), 684–693.

[79] Kuo, P.L., Liang, W.J., Lin, C.L. (2002). Solid polymer electrolytes, 2: Preparation and ionic conductivity of solid polymer electrolytes based on segmented polysiloxane-modified polyurethane. Macromolecular Chemistry and Physics, 203(1), 230–237.

[80] Zhang, Z., Jin, J., Bautista, F., Lyons, L., Shariatzaden, N., Sherlock, D., Amine, K., West, R. (2004). Ion conductive characteristics of cross-linked network polysiloxane-based solid polymer electrolytes. Solid State Ionics, 170(3–4), 233–238.

[81] Nair, J., Destro, M., Gerbaldi, C., Bella, F. (2015). Siloxane Diacrylate-based All-Solid Polymer Electrolytes for Lithium Batteries. International Journal of Membrane Science and Technology, 2(1), 23–27.

[82] Oh, B., Vissers, D., Zhang, Z., West, R., Tsukamoto, H., Amine, K. (2003). New interpenetrating network type poly(siloxane-g-ethylene oxide) polymer electrolyte for lithium battery. Journal of Power Sources, 119–121, 442–447.

[83] Boaretto, N., Joost, C., Seyfried, M., Vezzù, K., Di Noto, V. (2016). Conductivity and properties of polysiloxane-polyether cluster-LiTFSI networks as hybrid polymer electrolytes. Journal of Power Sources, 325, 427–437.

[84] Bharwal, A.K., Manceriu, L., Iojoiu, C., Dewalque, J., Toupance, T., Hirsch, L., Henrist, C., Alloin, F. (2018). Ionic-Liquid-like Polysiloxane Electrolytes for Highly Stable Solid-State Dye-Sensitized Solar Cells. ACS Applied Energy Materials, 1(8), 4106–4114.

[85] Grewal, M.S., Tanaka, M., Kawakami, H. (2019). Free-standing polydimethylsiloxane-based cross-linked network solid polymer electrolytes for future lithium ion battery applications. Electrochimica Acta, 307, 148–156.

[86] Boaretto, N., Horn, T., Popall, M., Sextl, G. (2017). Optimization of the transport and mechanical properties of polysiloxane/polyether hybrid polymer electrolytes. Electrochimica Acta, 241, 477–486.

[87] Kumar, A., Bankoti, S. (2009). Synergistic study on electrochemically deposited thin film with a spectrum from micro to nano range structures, National Institute of Technology, 2009.

[88] Fang, R., Zhao, S., Sun, Z., Wang, D.-W., Cheng, H.-M., Li, F. (2017). More Reliable Lithium-Sulfur Batteries: Status, Solutions and Prospects. Advanced Materials, 29(48), 1606823.

[89] Arof, A.K., Amirudin, S., Yusof, S.Z., Noor, I.M. (2014). A method based on impedance spectroscopy to determine transport properties of polymer electrolytes. Phys. Chem. Chem. Phys., 16(5), 1856–1867.

[90] Doan, T.N.L., Ghaznavi, M., Zhao, Y., Zhang, Y., Konarov, A., Sadhu, M., Tangirala, R., Chen, P. (2013). Binding mechanism of sulfur and dehydrogenated polyacrylonitrile in sulfur/polymer composite cathode. Journal of Power Sources, 241, 61–69.

[91] Ye, J., He, F., Nie, J., Cao, Y., Yang, H., Ai, X. (2015). Sulfur/carbon nanocomposite-filled polyacrylonitrile nanofibers as a long life and high capacity cathode for lithium-sulfur batteries. Journal of Materials Chemistry A, 3(14), 7406–7412.

[92] Lee, S.Y., Kim, J.H., Lee, Y.H., Cho, S.J., Gwon, J.G., Cho, H.J., Jang, M., Lee, S.Y. (2019). Nanomat Li-S batteries based on all-fibrous cathode/separator assemblies and reinforced Li metal anodes: Towards ultrahigh energy density and flexibility. Energy and Environmental Science, 12(1), 177–186.

[93] Fu, K., Li, Y., Dirican, M., Chen, C., Lu, Y., Zhu, J., Li, Y., Cao, L., Bradford, P.D., Zhang, X. (2014). Sulfur gradient-distributed CNF composite: A self-inhibiting cathode for binder-free lithium-sulfur batteries. Chemical Communications, 50(71), 10277–10280.

[94] Bajaj, P., Sreekumar, T. V, Sen, K. (2002). Structure development during dry-jet-wet spinning of acrylonitrile/vinyl acids and acrylonitrile/methyl acrylate copolymers. Journal of Applied Polymer Science, 86(3), 773–787.

[95] Dzenis, Y. (2004). Fibers for Nanotechnology. Science, 304(June), 1917–1920.

[96] Hara, T., Konarov, A., Mentbayeva, A., Kurmanbayeva, I., Bakenov, Z. (2015). High Mass-Loading of Sulfur-Based Cathode Composites and Polysulfides Stabilization for Rechargeable Lithium/Sulfur Batteries. Frontiers in Energy Research, 3, 22.

[97] Schoener, C.A., Weyand, C.B., Murthy, R., Grunlan, M.A. (2010). Shape memory polymers with silicon-containing segments., 1787–1793.

[98] Mentbayeva, A., Belgibayeva, A., Umirov, N., Zhang, Y., Taniguchi, I., Kurmanbayeva, I., Bakenov, Z. (2016). High performance freestanding composite cathode for lithium-sulfur batteries. Electrochimica Acta, 217, 242–248.

[99] Konarov, A., Bakenov, Z., Yashiro, H., Sun, Y.K., Myung, S.T. (2017). Effect of carbon-sulphur bond in a sulphur/dehydrogenated polyacrylonitrile/reduced graphene oxide composite cathode for lithium-sulphur batteries. Journal of Power Sources, 355, 140–146.

[100] Yin, F., Liu, X., Zhang, Y., Zhao, Y., Menbayeva, A., Bakenov, Z., Wang, X. (2017). Well-dispersed sulfur anchored on interconnected polypyrrole nanofiber network as high performance cathode for lithium-sulfur batteries. Solid State Sciences, 66, 44–49.

[101] Donnet JB, Wang TK, Peng JC, R.S. (1998). Jean-Baptiste Donnet - Carbon fibers-Marcel Dekker (1998). 3rd ed. CRC Press, New York.

[102] Zhou, Z., Lai, C., Zhang, L., Qian, Y., Hou, H., Reneker, D.H., Fong, H. (2009). Development of carbon nanofibers from aligned electrospun polyacrylonitrile nanofiber bundles and characterization of their microstructural, electrical, and mechanical properties. Polymer, 50(13), 2999–3006.

[103] Zussman, E., Chen, X., Ding, W., Calabri, L., Dikin, D.A., Quintana, J.P., Ruoff, R.S. (2005). Mechanical and structural characterization of electrospun PAN-derived carbon nanofibers. Carbon, 43(10), 2175–2185.

[104] Shin, H.K., Jeun, J.P., Kang, P.H. (2012). The characterization of polyacrylonitrile fibers stabilized by electron beam irradiation. Fibers and Polymers, 13(6), 724–728.

[105] Wu, M., Wang, Q., Li, K., Wu, Y., Liu, H. (2012). Optimization of stabilization conditions for electrospun polyacrylonitrile nanofibers. Polymer Degradation and Stability, 97(8), 1511–1519.

[106] Moon, S., Farris, R.J. (2009). Strong electrospun nanometer-diameter polyacrylonitrile carbon fiber yarns. Carbon, 47(12), 2829–2839.

[107] Hou, H., Ge, J.J., Zeng, J., Li, Q., Reneker, D.H., Greiner, A., Cheng, S.Z.D. (2005). Electrospun Polyacrylonitrile Nanofibers Containing a High Concentration of Well-Aligned Multiwall Carbon Nanotubes. Chemistry of Materials, 17(5), 967–973.

[108] Song, C., Wang, T., Qiu, Y., Qiu, J., Cheng, H. (2009). Effect of carbonization atmosphere on the structure changes of PAN carbon membranes. Journal of Porous Materials, 16(2), 197–203.

[109] Wang, S.X., Yang, L., Stubbs, L.P., Li, X., He, C. (2013). Lignin-derived fused electrospun carbon fibrous mats as high performance anode materials for lithium ion batteries. ACS Applied Materials and Interfaces, 5(23), 12275–12282.

[110] Zhang, Y., Tajaddod, N., Song, K., Minus, M.L. (2015). Low temperature graphitization of interphase polyacrylonitrile (PAN). Carbon, 91, 479–493.

[111] Gupta, A., Dhakate, S.R. (2017). Development of structurally stable electrospun carbon nanofibers from polyvinyl alcohol. Materials Research Express, 4(4), 045021.

[112] Jawhari, T., Roid, A., Casado, J. (1995). Raman spectroscopic characterization of some commercially available carbon black materials. Carbon, 33(11), 1561–1565.

[113] Kim, C., Park, S.H., Cho, J.I., Lee, D.Y., Park, T.J., Lee, W.J., Yang, K.S. (2004). Raman spectroscopic evaluation of polyacrylonitrile-based carbon nanofibers prepared by electrospinning. Journal of Raman Spectroscopy, 35(11), 928–933.

[114] Wang, Y., Alsmeyer, D.C., McCreery, R.L. (1990). Raman spectroscopy of carbon materials: structural basis of observed spectra. Chemistry of Materials, 2(5), 557–563.

[115] Kalybekkyzy, S., Mentbayeva, A., Kahraman, M.V., Zhang, Y., Bakenov, Z. (2019). Flexible S/DPAN/KB Nanofiber Composite as Binder-Free Cathodes for Li-S

Batteries. Journal of The Electrochemical Society, 166(3), A5396–A5402.

[116] Nair, J.R., Gerbaldi, C., Destro, M., Bongiovanni, R., Penazzi, N. (2011). Methacrylic-based solid polymer electrolyte membranes for lithium-based batteries by a rapid UV-curing process. Reactive and Functional Polymers, 71(4), 409–416.

APPENDIX

Figure AP1 Differential scanning calorimetry (DSC) curves of the PPE10 SPE with $[EO]/[Li^{+}] = 6$.

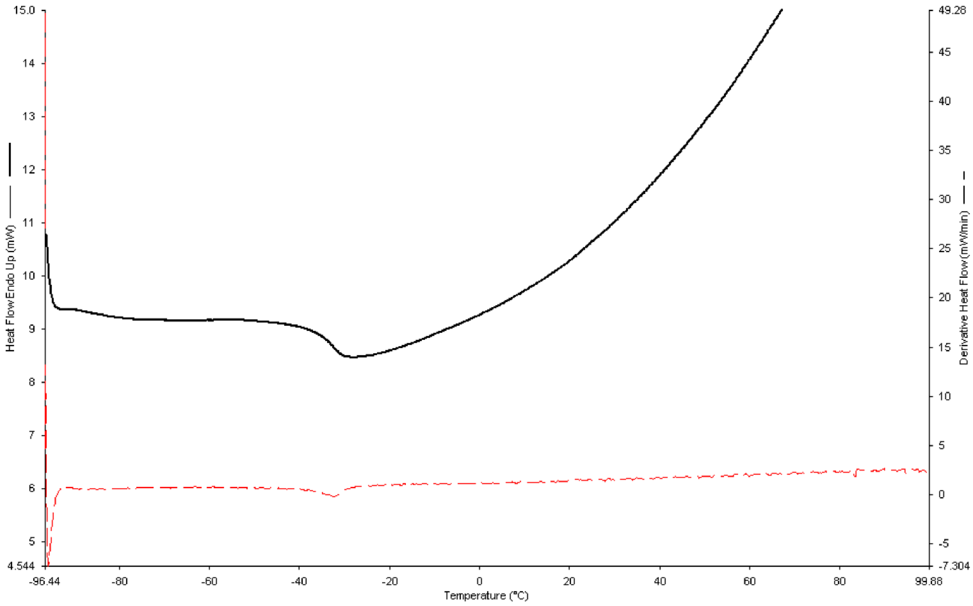

Figure AP2 Differential scanning calorimetry (DSC) curves of the PPE15 SPE with $[EO]/[Li^{+}] = 6$.

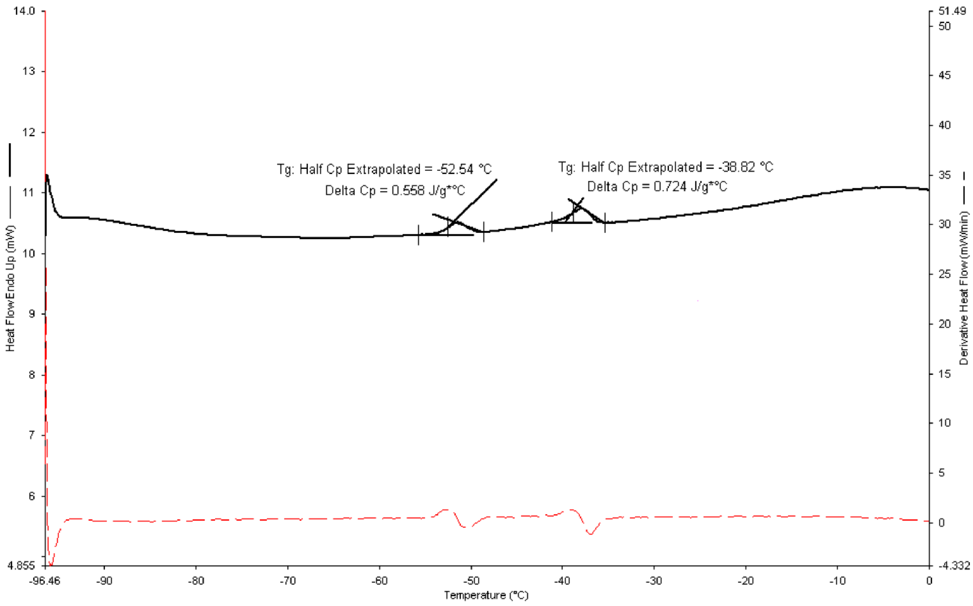

RESUME

Sandugash KALYBEKKYZY

Address: 53 Kabanbay batyr ave., Nur-Sultan 010000

Tel: +77753031494 Email: skalybekkyzy@marun.edu.tr

EDUCATION

2015 - 2020 **PhD in Organic Chemistry**, Marmara University

Dissertation Title: *"Development of Polymer Materials for Flexible Lithium-ion Batteries"*

Supervisor: Prof. Memet Vezir KAHRAMAN

Co-advisor: Prof. Zhumabay Bakenov

Orientations: Nanomaterials, Flexible components for Li-ion batteries, Polymer chemistry.

2013 - 2015 **MS in Chemistry**, Al-Farabi Kazakh National University

Dissertation Title: *"Soft mechanochemical synthesis of a series of phosphate"*

Thesis Supervisor: Prof. Galina Kuanysheva

Orientations: Synthesis of Polyphosphates, Mechanochemistry

2008 - 2013 **BA in Chemistry Education**, Marmara University

Orientations: Developed a large scientific interest and teaching experience

RESEARCH INTERESTS

Polymer materials, Nanomaterials, Electrospinning technique, Li/S batteries

HONORS & AWARDS

Ali Kuşçu Science and Technology Scholarship for PhD (2015 – 2020)

Mevlana Exchange Programme Scholarship (2014 – 2015)

Graduate Program Stipend of Ministry of Education of Kazakhstan (2013 – 2015)

Turkey Scholarship for Undergraduate Studies (2008 – 2013)

PROFESSIONAL ACTIVITIES

Supervised thesis projects of undergraduate students' during MS and PhD.

Successfully completed certificate program "Education on Animal Use for Researchers" Marmara University, 2017.

WORK EXPIRIENCE

2018 - present Junior Researcher, National Laboratory Astana, Nazarbayev University, Kazakhstan

2014-2015 Visiting Research Assistant, Gazi University, Turkey

2013-2014 Research Assistant, Al-Farabi Kazakh National University, Kazakhstan

RESEARCH PROJECTS

- Innovative Materials and Systems for Energy Conversion and Storage, State Targeted Program, Funded by MES RK, 2018-2020, Researcher.
- Development of safe and high performance flexible Li-ion batteries, Research Grant from Nazarbayev University, 2019-2022, Researcher.

PUBLICATIONS

1. S. Kalybekkyzy, A. Mentbayeva, M.V. Kahraman, Y. Zhang, Z. Bakenov, Flexible S/DPAN/KB Nanofiber Composite as Binder-Free Cathodes for Li-S Batteries // Journal of The Electrochemical Society (2019), 166 (3) P. A5396-A5402, [DOI: 10.1149/2.0571903jes] (IF=3.120)
2. S. Kalybekkyzy, A. Mentbayeva, Y. Yerkinbekova, N. Baikalov, M.V. Kahraman, Z. Bakenov, Lightweight 3D Structured Nanofiber Current Collector for High Capacity Sulfur Cathode // Electrochimica Acta. (IF=5.383), (submitted).

CONFERENCES

1. Mentbayeva A., Kalybekkyzy S., Bakenov Z. S/PAN/C Flexible composite cathode made of nanofibers formed by electrospinning // The 19th International Meeting on Lithium Batteries (IMLB 2018), June 17-22, 2018, Kyoto, Japan. Poster Presentation.
2. Kalybekkyzy S., Mentbayeva A., Bakenov Z. Flexible Composite of S/PAN/C Nanofibers by Electrospinning as Binder–Free Cathodes for Li-S Batteries // The 6th International Conference on Nanomaterials and Advanced Energy Storage Systems (INESS-2018), August 8-10, Astana, Kazakhstan. Oral Presentation.
3. Kalybekkyzy S., Mentbayeva A., Zhang Y., Bakenov Z., Freestanding S/PAN/C composite cathode obtained by electrospun nanofibers // The 59th Battery Symposium in Japan, November 27-29, 2018, Osaka, Japan. Oral Presentation.
4. Mentbayeva A., Kopzhassar A.-F., Kalybekkyzy S., Kahraman M. V., Bakenov Z., UV cured gel polymer electrolyte for flexible lithium-ion batteries // The 2019 Spring Meeting of the European Materials Research Society (E-MRS 2019), May 25-29, 2019, Nice, France. Oral Presentation.
5. Kalybekkyzy S., Mentbayeva A., Kahraman M.V., Zhang Y., Bakenov Z. UV-crosslinked flexible solid polymer electrolyte for lithium-ion batteries // European Polymer Congress EPF 2019, June 9-14, Heraklion, Greece. Oral Presentation.
6. Serik N., Baikalov N., Mentbayeva A., Kalybekkyzy S., Yerkinbekova Y., Bakenov Z. High mass-loading sulfur composite cathode on three-dimensional carbon fiber paper as current collector // 6th NanoToday 2019, June 16-20, Lisbon, Portugal. Oral Presentation.
7. Yerkinbekova Y., Kalybekkyzy S., Zhanadilov O., Bakenov Z., Mentbayeva A. Sulfur-containing composite cathode materials for Li-Ion batteries obtained by vacuum infiltration method // The 7th International Conference on Nanomaterials and Advanced Energy Storage Systems (INESS-2019), August 7-9, Almaty, Kazakhstan. Poster Presentation.
8. Kalybekkyzy S., Kopzhassar A., Mentbayeva A., Kahraman M.V., Zhang Y., Bakenov Z. UV-crosslinked flexible solid polymer electrolyte for lithium-ion batteries // The 7th International Conference on Nanomaterials and Advanced Energy

Storage Systems (INESS-2019), August 7-9, Almaty, Kazakhstan. Poster Presentation.

9. Kurmanbayeva I., Kalybekkyzy S., Mentbayeva A., Bakenov Z. SiOx anodes for LIB // The 7th International Conference on Nanomaterials and Advanced Energy Storage Systems (INESS-2019), August 7-9, Almaty, Kazakhstan. Poster Presentation.
10. Baikalov N., Serik N., Kalybekkyzy S., Kurmanbayeva I., Bakenov Z. Mentbayeva A. High Mass-Loading Sulfur-Composite Cathode for High Performance Lithium-Sulfur Batteries // The 7th International Conference on Nanomaterials and Advanced Energy Storage Systems (INESS-2019), August 7-9, Almaty, Kazakhstan. Poster Presentation.
11. Mentbayeva A., Kalybekkyzy S., Kopzhassar A., Kahraman M.V., Bakenov Z. Flexible solid polymer electrolyte for lithium-ion batteries // The 8th International Symposium on Specialty Polymers, August 23-25, 2019, Karaganda, Kazakhstan. Oral Presentation.
12. Kassenova N., Kalybekkyzy S., Kahraman M.V., Bakenov Z., Mentbayeva A. Fabrication and characterization of poly(vinyl alcohol)/maleic anhydride (PVA/MA) based polymer membranes for gel polymer electrolyte by electrospinning for lithium-ion batteries // The 7th International Conference on Nanomaterials and Advanced Energy Storage Systems (INESS-2019), August 7-9, Almaty, Kazakhstan. Oral Presentation.
13. Kalybekkyzy S., Kopzhasar A., Kahraman M.V., Mentbayeva A., Bakenov Z., Investigation on flexible polymer electrolyte for lithium-ion batteries // The 60th Battery Symposium in Japan, November 13-15, 2019, Kyoto, Japan. Oral Presentation.